Models of multi-messenger source of cosmic rays, gamma-rays and neutrinos

Makarim Bouyahiaoui

Université de Paris

Thèse préparée à Université de Paris

École doctorale des Sciences de la Terre et de l'Environnement et Physique de l'Univers - ED n°560

Laboratoire AstroParticules et Cosmologie (APC) - Groupe Théorie

---

Models of multi-messenger source of cosmic rays, gamma-rays and neutrinos

---

Thèse de doctorat de Physique de l'Univers

Makarim Bouyahiaoui

dirigée par Dmitri Semikoz

présentée et soutenue publiquement le 03 décembre 2021
devant le jury composé de :

Stefano Gabici Chargé de recherche (APC, Paris)	Examinateur
Kumiko Kotera Chargée de recherche (IAP, Paris)	Examinatrice
Martin Lemoine Directeur de recherche (IAP, Paris)	Rapporteur
Etienne Parizot Professeur (APC, Paris)	Examinateur
Grigory Rubtsov Professor (INR, Moscow)	Rapporteur
Dmitri Semikoz Directeur de recherche (APC, Paris)	Directeur de thèse

Abstract

Cosmic rays up to knee energy around 4 PeV, at which their spectrum sharply steepens, are believed to be produced in Milky Way Galaxy from supernovae explosions.

Recently it was understood that the large scale magnetic field of the Galaxy plays crucial role in the anisotropic diffusion of cosmic rays and helps them to escape from the Galaxy. Such anisotropic diffusion leads to a much smaller number of sources contributing locally. Furthermore, only a small fraction of supernovae can accelerate to PeV energies. Together with anisotropic diffusion this leads to significant or even dominated contribution of individual sources to local cosmic ray spectrum around the knee.

We model the contribution of the nearest young supernova remnant Vela to the local CRs flux taking into account both the influence of the Local Bubble and the effect of anisotropic diffusion. We found that the magnetic field in the bubble wall prevents low-energy particles penetrate into the bubble, leading to an energy-dependent suppression of CRs from Vela inside the bubble. We recovered the knee observed in the CRs spectrum of energy 3-5 PeV. By the contribution of Vela and an older local source of 2-3 Myr supernova we were able to explain the CRs spectrum from TeV to 100 PeV.

Then, We studied secondary neutrinos and gamma rays produced by interaction of cosmic rays with energies up to PeV in the wall of the Local Bubble.

We show that such a scenario can generate a substantial fraction of the observed astrophysical high-energy neutrino flux below $\sim$ few $\times$ 100 TeV. Finally, we extend our study to all other young supernovae remnants at less than 1 kpc from us. We calculated the CRs density around each source, assuming anisotropic diffusion. We used recent models of dust distribution in the local ISM extracted from extinction studies of Gaia data. Combining the obtained CRs densities with the matter distribution deduced from extinction maps, we found two prominent hot spots: One of them is close to the highest intensity hot spot in IceCube 10 years data.

Key words : Cosmic rays knee, anisotropic diffusion, vela supernova, galactic neutrinos.

Résumé

On pense que les rayons cosmiques jusqu'à l'énergie du "genou" autour de 4 PeV, ou le spectre change d'index, sont produits dans la Voie lactée à partir d'explosions de supernova. Récemment, il a été admis que le champ magnétique galactique régulier à grande échelle joue un rôle crucial dans la diffusion anisotrope des rayons cosmiques et les aide à s'échapper de la galaxie. Une telle diffusion anisotrope conduit à un nombre beaucoup plus petit de sources contribuant à n'importe quel point de la galaxie. Cependant, seule une petite fraction de supernova peut accélérer jusu'aux énergies PeV. Avec la diffusion anisotrope, cela conduit à une contribution significative ou même dominée des sources individuelles au spectre local des rayons cosmiques autour du "genou".

Dans ce travail, nous modélisons la contribution du rémanent de supernova Vela, étant la plus proche de notre système solaire, et nous calculons le flux local de rayons cosmiques reçus en tenant compte à la fois de l'influence de la Bulle Locale et de l'effet d'une diffusion anisotrope. Nous avons constaté que le champ magnétique dans la paroi de la bulle empêche les particules de faibles énergies de pénétrer dans la bulle, entraînant une suppression dépendant de l'énergie des rayons cosmiques de Vela à l'intérieur de la bulle. Nous avons réussi à reconstituer le "genou" observé dans le spectre des rayons cosmiques d'énergie 4-5 PeV. Grâce à la contribution de Vela et d'une source

locale plus ancienne de 2-3 Myr, nous avons pu expliquer le spectre des rayons cosmiques de TeV à 100 PeV. Ensuite, nous avons étudié la production de particules secondaires telles que les neutrinos et les rayons gamma issus de l'interaction des rayons cosmiques avec des énergies allant jusqu'au PeV dans la paroi de la Bulle Locale. Nous montrons qu'un tel scénario peut générer une fraction substantielle du flux astrophysique de neutrinos de haute énergie observés en dessous de quelques centaines de TeV. Enfin, nous étendons notre étude à toutes les autres jeunes supernovas à moins de 1 kpc de nous. Nous avons calculé la densité de rayons cosmiques autour de chaque source, en supposant une diffusion anisotrope. Nous avons utilisé des modèles récents de distribution de poussière dans le milieu interstellaire local extrait d'études d'extinction issues des données de Gaia. En combinant les densités de rayons cosmiques obtenues avec la distribution de matière déduite des cartes d'extinction, nous trouvons deux hotspots importants : l'un des deux est proche du point le plus significatif de la recherche de sources ponctuelles de IceCube.

Mots clés : Rayons cosmiques "genou", diffusion anisotrope , supernova Vela, neutrinos galactiques.

Description du projet et résumé de la thèse

Nous recevons continuellement sur terre une pluie de particules très énergétiques connues sous le nom de rayons cosmiques. Cette appellation englobe les protons et les ions mais aussi les photons, les leptons chargés et les neutrinos.

Le spectre d'énergie des rayons cosmiques suit une loi de puissance $\frac{dN}{dE} \propto E^{-\alpha}$ avec un indice spectral de $\alpha = -2.7$, cependant des deviation charactéristiques sont a noté, la plus remarquable est le "genou". Le genou a été initialement observé par Kulikov and Khristiansen en 1958 [152] correspondant à un changement d'indice de 2.7 à 3.1 a $E \simeq 4\,\mathrm{PeV}$. A des energies plus elevées on observe l'effet inverse au genou connu sous le nom de "cheville" qui se produit à $E \simeq 3 - 4\,\mathrm{EeV}$ ou la pente α remonte a 2.6. Et finalement l'effet GZK, obervé à $E > 4 - 5 \times 10^{19}\,\mathrm{eV}$ correspondant à la suppression de particules du à leur interactions avec le CMB.

L'origine et l'accélération des rayons cosmiques restent encore des mystères non entièrement élucidés, néanmoins, plusieurs théories et modèles tentent de l'expliquer.

Il est communément admis que les rayons cosmiques de basses énergies $\sim$ jusqu'au genou proviennent de sources galactiques, c.à.d sont accéléré

dans la Voie Lactée à partir de remnant de supernovae par exemple. Ces dernières représentent les sources idéales car elles rejettent dans la Galaxie suffisamment d'énergie pour justifier l'accélération des rayons cosmiques à travers le mechanism de Fermi du second ordre qui prédit un spectre d'énergie de particules accélérées suivant une loi de puissance $\frac{dN}{dE} \propto E^{-2}$.

Une fois qu'ils quittent leurs sources, les rayons cosmiques suivent une trajectoire dictée par le champ magnétique galactique qui est composé d'une partie régulière plus une autre aléatoire. La diffusion des rayons cosmiques dépend à la fois du champs magnétique et de l'énergie des particules. Il a été montré que autour du genou la diffusion est fortement anisotrope, ceci impose que que le nombre de sources contribuant aux observations doit être restreint. En effet seules les sources connectées au système solaire par des lignes du champs magnétique sont susceptibles d'apporter une contribution considérable au spectre de rayons cosmiques observé sur terre.

Dans cette thèse nous avons étudié la possibilité qu'une source locale unique soit responsable du flux de rayons cosmiques autour du genou.

Erlykin and Wolfendale [94, 93] ont été les premiers a avoir émit cette idée et avaient proposé comme source dominante le remnant de supernova Vela. Le choix de Vela se justifie par sa proximité 270 pc. En effet c'est la plus proche source de notre système solaire et elle y est connecté par des lignes de champs magnétiques. Nous avons modélisé la propagation de protons et d'ions de Vela en tenant en compte l'effet de la Bulle Locale qui entours le système solaire. Nous avons représenté le champ magnétique local en utilisant 2 configuration, d'abord un champ magnétique uniform puis le model de Janson et Farrar auxquels nous avons ajouter l'effet de la Bulle Locale.

La Bulle Locale correspond à une cavité d'un rayon moyen approximatif

de 100 pc entourée par des parois d'épaisseurs variables qui se caractérisant par une forte densité de matière et un puissant champ magnétique qui entoure la bulle. Nous avons observé que la Bulle Locale régule la pénétration des rayons cosmiques et il en résulte un flux de particules reçu de Vela similaire à celui observé sur terre expérimentalement comme montré dans la figure 1.

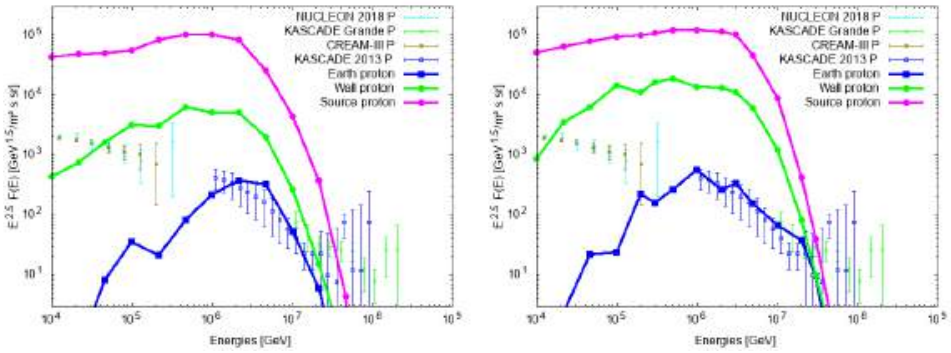

(a) U (b) JF

Figure 1: Contribution de Vela au flux de proton. Flux de proton a la source, dans les parois et près de la terre sont représentés en magenta, vert, et bleu respectivement pour les cas de champs magéntique externe U : uniform et JF: Janson Farrar. Les données expérimentales de NUCLEON [117], CREAM–3 [216] et KASCADE and KASCADE-Grande [47].

Notre modèle dépend fortement de la géométrie et de la distribution du champ magnétique dans la Bulle Locale, dont la description est paramétrique. Nous avons étudier la dépendance des résultats de notre simulation aux différents paramètres du modèle afin d'en calculer les incertitudes systémiques.

Au cours de leurs propagation les rayons cosmiques interagissent avec le milieu interstellaire produisant des neutrinos et des rayons gamma. Le milieu interstellaire se compose de toutes la matière distribué en dehors des étoiles dans la galaxie souvent sous forme de gaz diffus ou de nuages moléculaires. Il est constitué de 90% d'hydrogène, de 9% d'hélium et de 1% d'atomes plus lourds généralement appelés métaux. Il existe différents moyens de sonder la

distribution de la matière dans le milieu interstellaire. Des traceurs tels que les lignes d'absorption ou d'émission de molécules sont souvent utilisés. Il est possible de calculer la densité de colonne en mesurant le taux de lumière absorbé par la poussière interstellaire. Cette méthode basé sur l'extinction de lumière a permit de produire des relevés de plus en plus précis. Des cartographies 3D se basant sur cette technique permettent de produire avec une haute précision les structures telles que des nuages moléculaires: Taurus, Perseus ou la Bulle Locale. Nous avons utilisés la cartographie de Leike et al issues des données Gaia afin de modéliser la distribution de poussière localement. Nous avons mesuré le flux de neutrinos et de rayons gamma produits. Nous nous sommes intéressé dans un premier temps à l'interaction de proton de Vela aux parois de la Bulle Locale. Nous avons obtenues es résultats encourageant compatibles avec les données expérimentales. Les resultats sont représenté dans la figure 2 qui represente le flux de neutrinos et de rayons gamma issus de l'interactions des rayons cosmique provenant de Vela aux parois de la Bulle Locale.

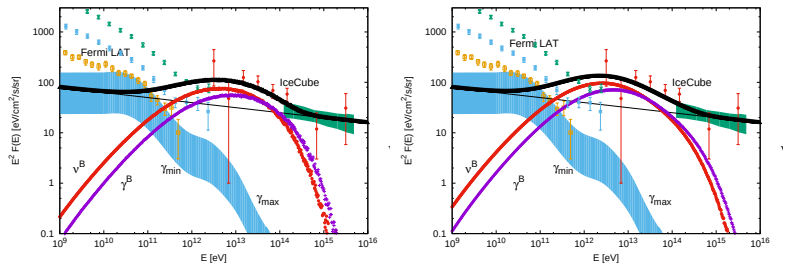

(a) U (b) JF

Figure 2: Contribution multi-messager de rayons cosmiques, neutrinos et rayons gamma de l'interaction dans les parois de la Bulle Locale comparés aux données de IceCube et de Fermi pour les cas de champs magéntique externe U : uniform et JF: Janson Farrar. La contribution extragalatic de neutrinos est modélisé par $1/E^{2.1}$.

Nous avons ensuite étendu notre travail en incluant d'autres sources lo-

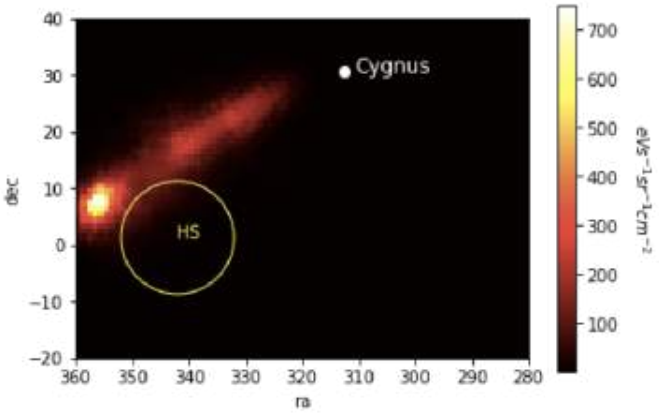

Figure 3: L'intensité du flux de neutrino $E^2 I_\nu(E, \alpha, \delta)$ pour $E = 100\,\mathrm{TeV}$ dans les coordonnées equatorielles; le cercle représente le point le plus significatif de IceCube.

cales. Nous avons calculé la densité de rayons cosmiques autour de chaque source, en supposant une diffusion anisotrope. En combinant les densités de rayons cosmiques obtenues avec la distribution de matière déduite des cartes d'extinction, nous trouvons deux hotspots importants : l'un des deux est proche du point le plus significatif de la recherche de sources ponctuelles de IceCube [10] tel que représenté en figure 3.

Aknowledgment

I first would like to thank Dmitri Semikoz for his supervision during these 3 years of PhD. I learnt a lot from him. He was always supportive and constantly available.
I also would like to thank Michael Kacherliess, with whom I collaborated for all my works. Working with him was enriching and instructive.
I want to like APC and Université de Paris for holding me during my PhD.
I thank my PhD committee members Stefano Gabici and Martin Lemoine for following my work during PhD and for their precious advices.
I sincerely thank my thesis reporters Martin Lemoine and Grigory Rubtsov for reading and reviewing my manuscript.
And I thank Stefano Gabici, Kumiko Kotera, Martin Lemoine, Etienne Parizot and Grigory Rubtsov for accepting to be part of my defense committe.

Je remercie ma mere pour son soutien infaillible et inconditionnel, aucun mot ne pourrait être assez fort pour exprimer ma reconnaissance et ma fierté d'être sa fille.
Je remercie mes soeurs Maya et Kamila pour avoir toujours été là et m'avoir supporté, spécialement vers la fin de ma thèse.
Je remercie très chaleureusement Wassim qui m'a toujours soutenu et encouragé et qui a toujours cru en moi.

Je remercie toute ma famille et ma belle-famille, spécialement tata Lydia pour m'avoir encouragé tout le long.

Je remercie mes amies Nesrine et Amira pour leur aide et leurs encouragements.

Je remercie tous mes amis(es) du laboratoire APC, plus particulièrement du groupe théorie avec qui j'ai partagé de très bons moments.

Je remercie toutes les personnes qui ont croisé mon chemin et qui participaient de près ou de loin à celle que je suis aujourd'hui.

Contents

General Introduction

Cosmic rays are the most energetic particles in the universe, travelling almost at the speed of light. The appellation *"cosmic rays"* can include photons, charged leptons and neutrinos, but we chose in this thesis a more conservative definition that consists only of protons and heavier nuclei.

The existence of cosmic rays was first established by Hess who has suggested that the increase of the atmospheric ionization rate with altitude has a cosmic origin [123]. The term *"cosmic rays"* was given by Millikan to describe the charged particles coming from space and ionizing the atmosphere. The first observation of secondary particles from extensive air shower was made by Kohlorster, Auger and their collaborators in 1930's [53, 148]. After the second world war, large detector arrays were installed permitting measurement of cosmic rays energy spectrum that was found to follow a power law $dN/dE \propto E^{-\alpha}$ with a spectral index $\alpha \simeq 2.7$. Multiplying cosmic rays measurement arises features in their energy spectrum. First one was the *knee* observed by Kulikov and Khristiansen [152] in 1958, it corresponds to a softening of the spectrum index from 2.7 to 3.1. Other features appear at higher energies as the *ankle* at $3 - 4\,\mathrm{EeV}$ where the slope goes again to 2.6 and the *GZK cutoff* at $4 - 5 \times 10^{19}\,\mathrm{eV}$ where cosmic rays are suppressed because of their interactions with CMB photons.

Up to *hundreds* TeV energies, cosmic rays are measured by satellite or bal-

loon experiments such as AMS-02 [23, 25], CREAM [216], NUCLEON [117, 52] and Dampe [40] among others. The direct measurements allows to reconstruct precisely their composition, which is found to be similar to sun abundances except for few unstable elements that are produced by spallation of heavier cosmic rays nuclei.

Higher energy cosmic rays are measured through the extensive air shower they produce. $10^6 - 10^9$ GeV events are measured by experiments such as KASCADE and KASCADE Grande, Tibet, TALE, Yakutsk array and Ice-Top among others. Above 10^9 GeV Ultra High Energy Cosmic Rays are measured by Auger and TA telescopes.

Cosmic rays sources fall into two categories : galactic (supernovae, novae, Super-bubbles) and extragalactic (AGN, straburst galaxies, GRB). The transition between the two categories depends on models, but it is believed to happen between few PeV and few EeV energies. The favoured galactic sources of cosmic rays are supernova remnants, since they release enough energy to justify the cosmic rays energy budget. In supernova remnant, cosmic rays are accelerated through diffuse shock acceleration mechanism that produces a spectrum following a power law $I \propto E^{-2}$. Recent works shows that magnetic field amplification produced by cosmic rays in the source affects the maximal attainable energy in supernova remnant and produces a spectrum that deviates from a single power law [60, 59].

After exiting the source, cosmic rays are constantly deflected by the galactic magnetic field before arriving to Earth, and their trajectory depends both on the regular and the turbulent part of the magnetic field. GMF is poorly understood since it can not be directly measured, but it is deduced from electromagnetic signal. The two main observables to probe the galactic magnetic field are Faraday rotation measures that depend on the thermal

electron distribution, and Sychrotron radiations that depend on the relativitic electron density. Various models were built to describe the galactic magnetic field, all of them use a multiple components structure containing a galactic disk and an out-of-plane regular field plus a random field that is usually described by its power spectrum $P(k) \propto k^{-\gamma}$. The diffusion coefficient of cosmic rays parallel and perpendicular to regular magnetic field lines can be computed and is directly linked to the turbulent magnetic field where $D(E) \propto E^{-\delta}$ where $\delta = 2 - \gamma$. The diffusion dependance δ is measured from the Boron-to-Carbon ratio in cosmic rays. Different experiments as AMS-02 [24], CREAM [31] and NUCLEON [119] found $\delta = 1/3$ and hence $\gamma = 5/3$ corresponding to Kolomogorov turbulence.

During propagation cosmic rays produce also γ rays and neutrinos through hadronic interactions in ISM. The interstellar medium (ISM) represents all matter distributed outside the stars in the form of molecular and atomic clouds and cold, warm and hot ionized regions. ISM is composed mainly of hydrogen at $\sim 90\%$ and helium $\sim 9\%$. One way of cumputing the hydrogen column density in ISM is by measuring extinction due to the presence of dust. Several dust maps describe the matter distribution. Nearby ISM $\lesssim 370\,\mathrm{pc}$ ISM was discussed by Leike et al. [157]. Larger region, up to $3\,\mathrm{kpc}$ distance was modeled by Lallement et al. [153].

Neutrinos and γ-rays astronomy together with CRs observations allow to conduct a multi-messenger study of astrophysical sources. Oppositely to CRs, neutrinos and γ-rays are unaffected by GMF, hence they point directly to their sources. Recent experiments, Fermi LAT [18], allowed to reconstruct γ-rays sky map and spectrum, new experiment such as LHAASO [55], aims to complete the γ-rays spectrum at higher energies. Neutrino astronomy is also a young field. Huge telescopes km^3 size as IceCube have been built to

observe neutrinos and permit to construct an energy spectrum of high energy neutrinos and compute their arrival direction in the sky. In a modern point of view the CRs, neutrinos and γ-rays spectra are deeply interdependent and correspond to a common astrophysical signal seen by different particles and at different energies.

In this thesis, we aimed to construct a multi-messenger model of CRs, neutrinos and γ-rays sources. A first part was dedicated to CRs *knee* study. In fact *knee* explications fall in three main categories : due to interaction properties, resulting from propagation, imprinted in source's properties or sources population. We studied the possibility that *knee* results from the dominance of a single source as proposed by Erlykin and Wolfendale [94, 93]. We chose Vela to be the dominant source since it is connected to us with magnetic field lines and we simulated the propagation of CRs taking into account the effect of the Locale Bubble which distort the magnetic field lines. The Local Bubble shape and strength of magnetic field is weakly constrained, thus our model depends on multiple parameters. We studied the dependence of our result on the main parameters.

In a second project we focused on neutrinos and γ rays counterpart of Vela CRs. A big fraction of CRs are trapped in the Local Bubble walls and they interact and produce photons and neutrinos. We computed the secondaries fluxes expected assuming a uniform distribution of matter in a cylindrical geometry all around the Local Bubble.

In the third project we extended our study to all local young potential sources of CRs from which we propagated particles and studied their interaction with matter deduced from Leike et al. [157] extinction maps.

This thesis is organised as follows. Part I will cover cosmic rays part. It contains 3 chapters. Chapter 1 will give a general description of galactic

magnetic field, essential to understand CRs propagation. Chapter 2 will summarize theoretical knowledge on cosmic rays mainly the energy spectrum, the acceleration mechanism and the propagation. The 3^{rd} chapter will present our modelisation of Vela as dominant source of CRs arround the *knee*.

Part II is dedicated to the two other messengers : γ and ν. In chapter 4 we will present ISM which represents the target on which CRs interact to produce secondaries. In chapter 5 we will describe γ-rays and neutrinos production and propagation and we will present their actual measured spectra. In the last chapter we will present our multi-messenger model for CRs, neutrino and γ-rays production from Vela and from other local sources that we will compare to the more recent neutrino sky map.

Finaly, we end the thesis by presenting a general conclusion and an outlook into future developments of the work presented here.

Part I

Cosmic rays

Chapter 1

Galactic Magnetic Field

Understanding galactic magnetic field (GMF) is primordial in many astrophysical topics such as: disk dynamics, turbulent ISM, molecular clouds collapse, star formation, supernova remnant evolution, and cosmic rays propagation [125]. It is critical to have a detailed description of the morphology and the strength of the galactic magnetic field to study cosmic rays propagation. It plays a major role in understanding how and where are this particle accelerated and which process they experience before reaching Earth. Modeling GMF is an active field of research and a consequent number of models were already produced. We mainly built this chapter on Jeffe review [125], where the author discusses galactic magnetic field modeling work that is either quite recent or still being used.

In this chapter we will give an overview of GMF and how it is measured. In section 1.1 we will present the main observables used to probe galactic magnetic field. Since there is no way to detect galactic magnetic field directly in each point of the Galaxy, we have to study it imprint on the electromagnetic signal from Faraday rotation measures and Sychroton emission of relativistic electrons to extracts the GMF properties. Then, we

will in section 1.2, present a general description of the galactic magnetic field components, the regular component that extends on galactic scale, and small scales turbulence that can be random or ordered. Finally, section 1.3 is dedicated to models of Milky Way magnetic field. When the general structure of GMF is poorly known, usually all models agreed in decomposing the magnetic field in the Milky Way on a disk , a halo and an out of plane component. At the end of that section, we will then focus on the Janson-Farrar model that we will introduce in more details since it is the model used in our work to describe GMF.

1.1 Observables to probe GMF

The GMF affects many physical processes that can be probed with differents observables. Even if none of these observables is sufficient to entirely model GME, each one contributes to probe partially its properties. We will in this section, describe the most commonly used GMF tracers.

Table 1.1 summarise well the observables with the GMF properties probed underlying the dependence on other parameters

Polarized starlight : Since dust grain align their long axes perpendicularly to magnetic field lines, they affect the polarization of light coming from stars behind. Dust grains absorb the part polarized perpendicularly and leave polarized starlight parallel to local field as projected onto the sky, hence perpendicular to LOS. Polarization measurements depends obviously on the knowledge of dust distribution. But it presents the advantage of providing 3D information if one uses star distances data. A recent catalog from Heiles [122] contain more the 9k individual stars measurements. Hence observing polarized starlight

Observable	GMF proprety probed	Dependencies	Pros	Cons
Faraday rotation	$B_{\parallel}$ orientation and strength	thermal electron density	3D sampling along the LOS	mostly in galactic plane
Diffuse synchrotron emission (radio)	$B_{\perp}$ orientation and strength (squared)	thermal electron density; cosmic rays electrons density	goes as $\|B\|^2$; full sky coverage ; probes turbulent Faraday effect.	not 3D info along LOS; polarization horizon of a few kpc due to Faraday depolarization effects.
Diffuse synchrotron emission (microwave)	$B_{\perp}$ orientation and strength (squared)	cosmic rays electrons density	goes as $\|B\|^2$; full sky coverage ; full LOS through the Galaxy; no Faraday rotation	no 3D info along LOS ; total intensity contaminated by Bremsstrahlung and AME
Diffuse dust emission	$B_{\perp}$ orientation	dust grain density, properties, environement and alignement	full sky coverage; full LOS through the Galaxy; 3D information with extinction surveys; no Faraday rotation	Probes only close to Galactic plane $\|z\| \lesssim 100$ pc
Starlight polarization	$B_{\perp}$ orientation	dust grain properties and distribution	3D information	sampling limited to few Kpc

Table 1.1: Large scale galactic magnetif field tracers with their dependencies, pros and cons [125].

informs us on $B_{\perp}$

Faraday Rotation Measures (RMs) of point sources : Polarized emission experience Faraday rotation while it propagate in the ISM. The rotation of the orientation of the linear polarization vector is wave-

length dependent. The observed rotated polarization angle is linked to RM as $\theta = \theta_0 + RM\lambda^2$, where θ_0 is the polarization angle of the source. This measurement probes the LOS component of the magnetic field $B_{\parallel}$ from observing polarized sources such as pulsars at different frequencies and fitting the polarization orientation as a function of frequency to get RMs. Since

$$RM \simeq 0.81 \int_0^L (\frac{n_e(l)}{cm^{-3}})(\frac{B_{\parallel}(l)}{\mu G})(\frac{dl}{pc}) \tag{1.1}$$

Where n_e is the thermal electron density on which $B_{\parallel}$ depends strongly. The number of available RM has increased considerably, we count more than 1k RM from galactic pulsars [121], and 42k for extragalactic polarized sources [202, 215]

Diffuse polarized synchrotron emission : The polarized radiation from radio frequencies to microwaves is dominated by galactic synchrotron emission. For a power law distribution of relativistic electrons (n_{cre}) with spectral index s, the synchrotron emissivity is

$$j_\nu \propto n_{cre} B_\perp^{\frac{1+s}{2}} \nu^{\frac{1-s}{2}} \tag{1.2}$$

n_{cre} is itself poorly known and depends on GMF, it is usually based on models as [197]. Polarization of the diffuse synchrotron emission has been measured in the form of Stokes parameters Q and U, where the polarized intensity is $PI = \sqrt{Q^2 + U^2}$, in radio by Reich et al [188] and Testori et al [203], in microwave through space based telescopes as WMAP [63] and Planck [21], which was useful since at microwave frequencies Faraday rotation is assumed to be negligeble. Nevertheless synchrotron emission and relativistic electron distribution are closely

linked and inter-dependant.

Diffuse polarized thermal dust emission : Grain dust produce thermal emission polarized perpendicular to the local magnetic field, since as discussed above, they align their axes in a perpendicular position. This observation is complementary to synchrotron emission, since it arises from a different region in the the sky, the cold density ISM close to galactic plane. The diffuse polarized thermal dust emission was first observed by Archeops [64] and more recently with Planck [21, 19]. Gaia mission provinding 3D dust model [155] will allow to probe B in 3D using dust.

1.2 Components of the Magnetic field

GMF models contain several components that are distinguishable by their properties and their imprint on the astronomical observables described in section 1.1. Figure 1.1 is a cartoon illustration that shows the morphology of each component and its effect on Faraday rotation measures (RMs), total synchrotron Intensity (I) and Polarized synchrotron Intensity (PI) at different point of view of the observer. We will in the following brielfy describe each component.

Coherent component is the part of the field with coherent direction on large scales, it is also called "Regular". It is studied through Faraday RM. Knowing the distribution of the thermal electron population and it's correlation with the field, one can extract the coherent field strength from RMs.

Isotropic random field : It is a field satisfying the condition $< B(x) >= 0$ and where $< B^2(x) >= B^2_{rms} > 0$. It is usually described as an

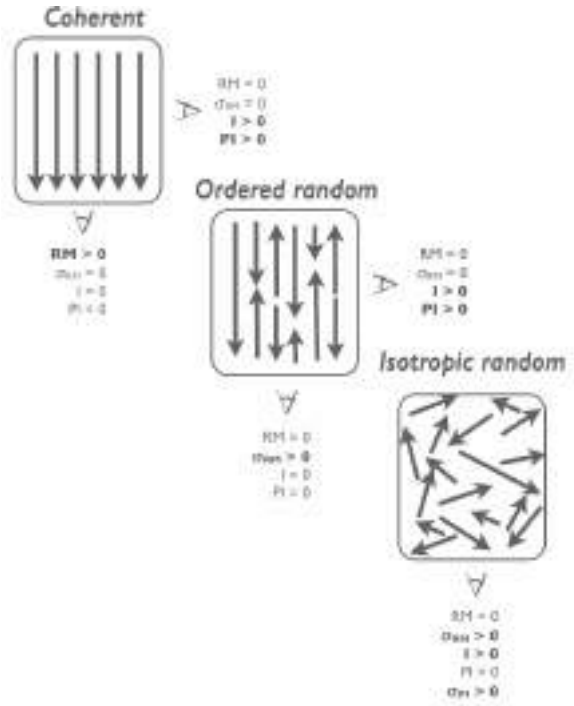

Figure 1.1: Cartoon illustrating several geometrical properties of magnetic fields. It shows the effective magnetic field components defined by their effects on the indicated observable [125].

isotropic Gaussian random field. The strength of the field could be measured using the polarization fraction of synchrotron emission or the variance of the polarization and RM but one has to take into account the particle distribution and its correlation with the fluctuations of the field.

Ordered random field : It is a random field that has a preferred orientation, but not a preferred direction, it is also called "striated" field.

1.3 Milky Way Magnetic Field models

In this section, we will focus on the coherent part of the GMF. The magnetic field on the Milky Way is dominated by the galactic disk contribution.

The mean strength of the field is of 1 μG. Different models were proposed to describe GMF morphology, these models are based either on theoretical computations or on purely observational deductions. All of them use a multiple component structure containing a galactic disk component following spiral arms, and an out of plane part. Many models are available in literature among which : Sun et al [199], Janson Farrar [127], Jaffe et al [126], Kachelriess et al [138], Fauvet et al [97], Pshirkov et al [183], Han [120] . Some of the models cited are shown in Fig 1.2.

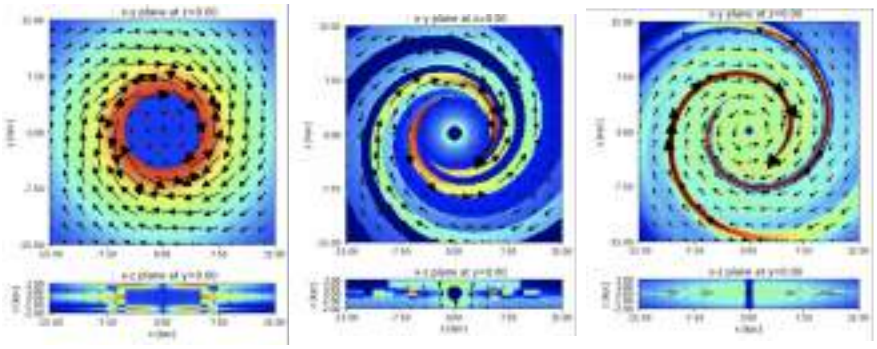

(a) Sun et al [199]

(b) Janson Farrar [127]

(c) Jaffe et al [126]

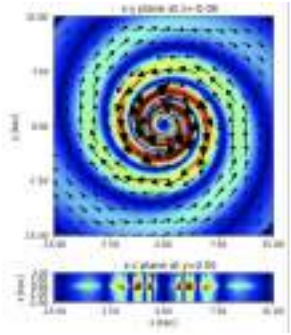

(d) Kachelriess et al [138]

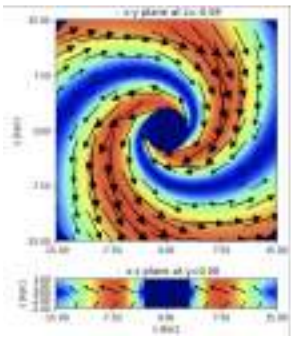

(e) Fauvet et al [97]

Figure 1.2: Example of coherent galactic magnetic field models. The color represents the strength of the magnetic field in arbitrary color scale, the arrows shows the directions of the magnetic field lines, the position of the sun is at (-8.5,0,0) kpc [125].

We will present in more details one of those models, the Janson-Farrar model, that we chose for our work in order to describe the regular GMF.

1.3.1 Janson Farrar model

The Janson-Farrar model is a 22 parameters model of large scale coherent magnetic field. This model is constructed using galactic polarized synchrotron emission maps from WMAP7 and more than 30000 extragalactic Faraday rotation measurements [127]. They constructed a model composed of large scale regular field plus a small scale random field and they include a "striated" part. We will here focus on the regular part. The large scale regular GMF is described with three separate components. In the following we will adopt, as the authors, a right handed Cartesian (x, y, z) and Cylindrical (r, Φ, z) coordinate systems, having the Galactic Center (GC) at the origin, and the sun at $x = -8.5$ kpc. Everywhere $B = 0 \quad \mu$G for $r > 20$ kpc. The large scale regular field of the Janson-Farrar model is composed of :

Disk component : the disk field is limited on galactic plane and has two components : the "molecular ring" extending from 3 kpc to 5 kpc where the magnetic field is purely azimuthal with strength b_{ring}, and "spiral arms" region extending from 5 kpc to 20 kpc where the magnetic field follow spiral arms. The later component count 8 logarithmic spiral regions that are divided as follows : $r = r_{-x} \exp(\phi \tan(90° - i))$, where $r_{-x} = 5.1, 6.3, 7.1, 8.3, 11.4, 12.7, 15.5,$ Kpc and i is the spiral arm. The magnetic field in the spirals follow :

$$\hat{b_i} = \sin(i)\hat{r} + \cos(i)\hat{\phi} \tag{1.3}$$

Where b_i is defined at $r = 5$ Kpc then decrease as $b_i(r) \propto r^{-1}$ until it reaches 0 for $r = 20\,\text{Kpc}$. To assure a smooth transition and a continuity between the different components of the large scale regular part, the authors use a logistic function $L(z, h, w) = (1 + e^{-2(|z|-h)})$

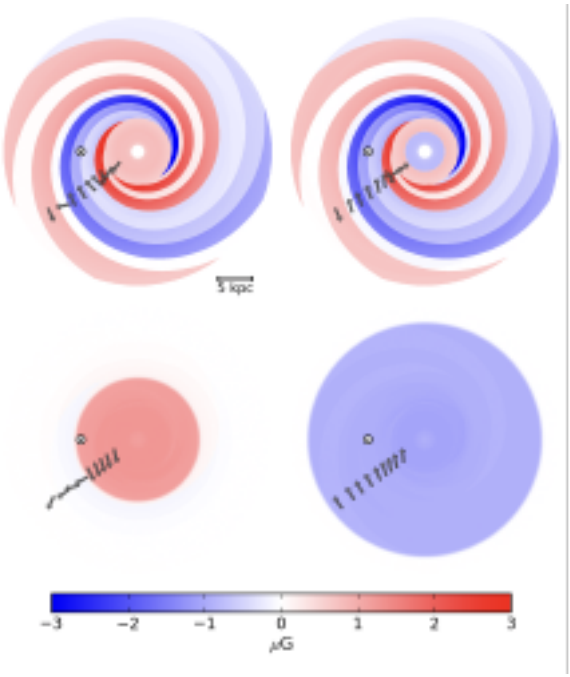

Figure 1.3: Top view of slices in the x-y plane of the GMF model. Top row, from left, slices ar $z = 10\,\mathrm{pc}$ and $z = -10\,\mathrm{pc}$. Bottom row, slices ar $z = 1\,\mathrm{kpc}$ and $z = -1\,\mathrm{kpc}$, respectively. The color scheme shows the magnitude of the total regular field, with negative values if the azimuthal component is oriented clockwise. The location of the Sun is at $x = -8.5\,\mathrm{kpc}$ is marked with a circle. Figure from [127]

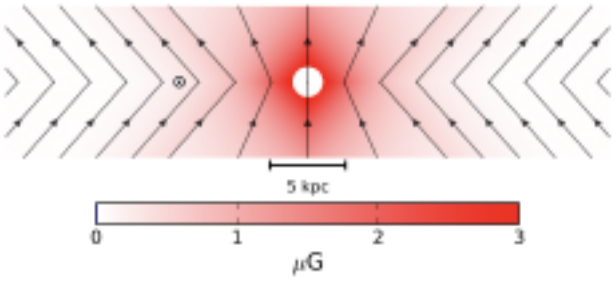

Figure 1.4: An x-z slice of the Galaxy showing only the out-of-plane "X" component. The black lines crossing the mid-plane at $\pm 4.8\,\mathrm{kpc}$ traces the boundary between the outer region with constant elevation angle, and the inner region with varying elevation angle. The black arrows show the direction of the field [127].

where the differents parameters are listed in table 1.2. At the transition the disk component is multiplied by $(1-L(z, h_{disk}, w_{disk}))$ and the halo component is multiplied by $L(z, h_{disk}, w_{disk})$.

Toroidal halo component : The halo component is purely toroidal, and is modeled as follow

$$B_{\phi}^{tor}(r,z) = e^{-|z|/z_0} L(z, h_{disk}, w_{disk}) \times \begin{cases} B_n(1 - L(r, r_n, w_h)) & \text{if z} < 0 \\ B_s(1 - L(r, r_s, w_h)) & \text{if z} > 0 \end{cases} \tag{1.4}$$

The magnetic amplitude in the north and in the south are separate where B_n is the magnetic field strength in the galactic north, B_s is the magnetic field strength in the galactic south. The halo field decreases exponentially with the height.

Out of plane component : The out of plane component is a generalization of the halo magnetic field, it is also named the "X-field" because it is motivated by the X-shape field structure observed in radio data of external galaxies [150, 58]. The X-field is axisymetric and poloidal and is defined as follows

$$b_X(r,z) = b_X(r_p) = B_X e^{-r_p/r_X} \tag{1.5}$$

Where r_p is the radius at which the field line passing through (r,z) cross the mid-plane (z=0). r_X^c represent the galacocentric radius, and we distinguish two regions : inside and outside the galacocentric region.

- Outside the galacocentric region where $r_X > r_X^c$ the field has a constant elevation angle Θ_X^0 with respect to the mid-plane and

the field strength is $b_X(r_p)r_p/r$, where

$$r_p = r - |z|/\tan(\Theta_X^0) \tag{1.6}$$

- Inside the galactocentric region where $r_X < r_X^c$, the elevation angle Θ_X is linear in the radius and becomes vertical for $r = 0$. The field strength is $b_X(r_p)(r_p/r)^2$ where

$$r_p = \frac{r r_X^c}{r_X^c + |z|/\tan(\Theta_X^0} \tag{1.7}$$

and

$$\Theta_X(r, z) = \tan^{-1}(\frac{|z|}{r - r_p}) \tag{1.8}$$

The four out of plane free parameters are specified in the table 1.2

1.3.2 Turbulent magnetic field

Galactic turbulent MF are resulting from the tangling and the compression of the mean field by mass flows. The energy is injected at large scales of magnetic field L_{max} of order 1-100 pc then it cascades to smaller scales until it dissipate at $L_{min} \sim$ u.a [137]. In models, we often use a Gaussian random field following an isotropic power law spectrum $P(k) \propto k^{-\gamma}$, with :

- $\gamma = \frac{5}{3}$ for Kolmogorov turbulence
- $\gamma = \frac{2}{3}$ for Iroshnikov kraichnan turbulence
- $\gamma = 1$ for Bohm turbulence

It appears from observation of the fluctuation in the thermal electron density that the power spectrum follows $P(k) \propto k^{-5/3}$ [48] , it agrees with the one

field	Best fit parameters	description
Disk	$b_1 = 0.1 \pm 1.8\mu$G	field stregth at r=5 Kpc
	$b_2 = 3.0 \pm 0.6\mu$G	
	$b_3 = -0.9 \pm 0.8\mu$G	
	$b_4 = -0.8 \pm 0.3\mu$G	
	$b_5 = -2.0 \pm 0.1\mu$G	
	$b_6 = -4.2 \pm 0.5\mu$G	
	$b_7 = 0.0 \pm 1.8\mu$G	
	$b_8 = 2.7 \pm 1.8\mu$G	
	$b_{ring} = 0.1 \pm 0.1\mu$G	$3\,\text{Kpc} \geq r \leq 5\,\text{Kpc}$
	$h_{disk} = 0.40 \pm 0.03$ Kpc	disk/halo transition
	$w_{disk} = 0.27 \pm 0.08$ Kpc	transition width
Toroidal halo	$B_n = 1.4 \pm 0.1\mu$G	northen halo
	$B_s = -1.1 \pm 0.1\mu$G	southern halo
	$r_n = 9.22 \pm 0.08$ Kpc	transition radius north
	$r_s > 16.7$ Kpc	transition radius south
	$w_h = 0.20 \pm 0.12$ Kpc	transition width
	$z_0 = 5.3 \pm 1.6$ Kpc	vertical scale height
X-field	$B_X = 4.6 \pm 0.3\mu$G	field strength at origin
	$\Theta_X^0 = 49 \pm 1^\circ$	elevation angle at z=0 and $r > r_X^c$
	$r_X^c = 4.8 \pm 0.2$ Kpc	radius where $\Theta_X = \Theta_X^0$
	$r_X = 2.9 \pm 0.1$ Kpc	exponential scale length

Table 1.2: Best fit Janson Farrar coherent galactic magnetic field model parameters [127].

predicted by Kolmogorov [149]. Results from the magnetometer in Voyager 1 confirms the slope of $\alpha = \frac{5}{3}$ and measured a strength of $B_{rms} \simeq 0.6$ μG [72].

1.3.3 Local Bubble

The solar system resides inside a bubble called the "Local Bubble" of hot and tenuous plasma. Superbubbles are believed to be created around OB associations from the merging of the wind-blown bubbles of the individual stars, forming a single superbubble [208, 151]. The shock waves induced by the explosion of those O and B stars, will expand quickly in ISM until they

reach the bubble wall where they are typically stopped [209] and instead of forming visible supernova remnants (SNR), they power the expansion of the superbubble in the ISM.

The Local Bubble extends roughly 200 pc in the Galactic plane, and 600 pc perpendicular to it, with an inclination of about 20° [154]. The Local Bubble abuts with the Loop 1 superbubble, and with another bubble towards the direction of the Galactic center [214], as shown in the figure 1.5 illustrating the structure of the Local Bubble and its local neighborhood.

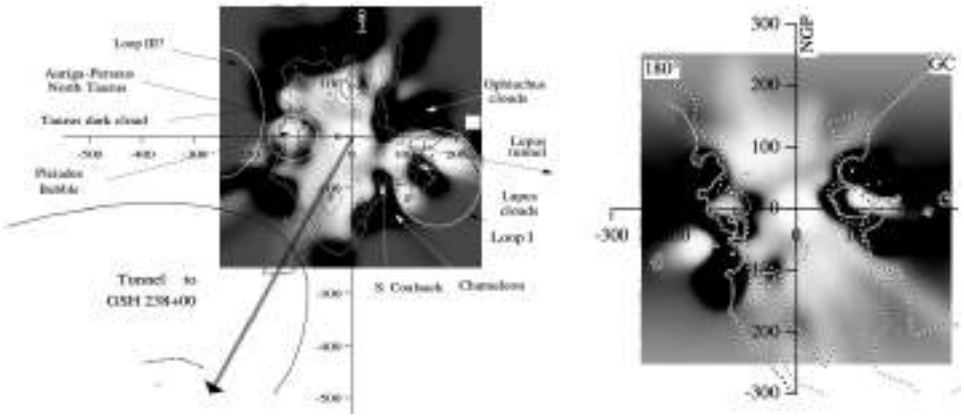

(a) (b)

Figure 1.5: Distribution of dense gas on a plane *(a)* vertical to the galactic plane and *(a)* parallel to the galactic plane. Figures from Ref. [154].

Because of the shock compressing in the Local Bubble walls the strength of the magnetic field is enhanced. It was estimated by Ref. [44] to 8^{+5}_{-3} μGusing Chandrasekhar-Fermi method. Ref. [163] measured Faraday RMs towards the Galactic South and North Pole and modelling the Local Bubble as a cylindrical shell with radius 85 pc and a wall thickness of 4 pc, they derived $B \simeq 9\,\mu$G inside the bubble wall.

Summary : Knowing GMF is crucial for understanding plenty of astrophysical subjects, among which cosmic rays. The structure of GMF dictates the trajectories of particles and thus is a clue information for cosmic rays origin and propagation. The galactic magnetic field has a regular large scale component and a small scale turbulent component, both affect the astronomical electromagnetic signal. The Faraday rotation measures and the polarized synchrotron emission have imprints of the GMF and allow to probe its properties. The regular component of the magnetic field is itself usually considered as a superposition of 3 components : a disk component concentrated in the galactic plane and following the spiral arms, a halo component describing the surrounding neighborhood of the galactic plane, and thrid component which is a generalisation of the halo component the out of place component inspired from the X-shape radio data. A lot of models describe in details each component, we chose to use for the rest of our work the Janson-Farrar model to which we will refer as JF decribing the regular magnetic field from now on.

Chapter 2

High Energy Cosmic rays

Introduction : High energy cosmic rays is one of the most puzzling astrophysical question of the last decades. These charged, energetics particles were discovered in the beginning of the 20^{th} century, and despite all the effort made, the mystery of cosmic field is yet unsolved. Where do they come from ? Which kind of mechanism is involved in their acceleration ? What kind of sources has the sufficient energy and efficiency to accelerate cosmic rays ? How do they propagate in ISM ?
In this chapter, we will try to give a general overview of cosmic rays, we will start with a general presentation of cosmic rays and we will discuss in section 2.2 cosmic rays spectrum and introduce the different features that remain unexplained until today. We will then present the experimental methods used to detect cosmic rays, and we will find out why it is so difficult to obtain precise CR measurements at very high energies in section 2.3.

Section 2.4 is dedicated to cosmic rays composition, that present some discrepancies when compared to our solar system abundances, we will explain the orgin of this differences. We will move to acceleration mechanism starting from Fermi's idea of magnetised clouds, then presenting the diffuse

shock acceleration that may be the leading process in cosmic rays acceleration in section 2.5. This will lead us to sources of cosmic rays in the next section . We ill discuss the Hillas criterion that put constraints on sources of CRs and present the energy budget of few potential sources of CRs. We will present in the section 2.7 the propagation of cosmic rays, will discuss the effect of the different GMF components on cosmic rays propagation. We will end this section by highlighting the actual challenges that face the traditional diffusion model. Finally, in the section 2.8, we will focus on one feature of the cosmic rays spectrum known as the "knee", we will present the characteristics of the knee and we will compare the possible explanations studied in literature.

2.1 What are cosmic rays

Cosmic rays are high energy charged particles that strike the Earth's atmosphere continuously. Most of the primary cosmic rays are protons and nuclei with a subdominant contribution from electrons positrons. CRs were discovered in 1785 by Coulomb with the unexplained discharge of electroscopes [86]. More than a century after, Hess uses observations of the increase ionization of the atmosphere with altitude measured from a balloon experiment to deduce that this effect must originate from outside the atmosphere [123]. By 1930s, it was shown from coincidence measurement of Bothe and Kohlhorster using Geiger-Muller counters[68], that atmosphere ionization is caused by charged particle, called later "cosmic rays" by Millikan. Soon after, Kohlhorster, Auger and their collaborators, established the extensive air shower detection technique [53, 148], and an array detector to measure CR spectrum was built after the second world war.

From 1930 to 1950 cosmic rays were a great tool for particle physics studies.

Before 1950's there was no accelerator , the only way to study relativistic high energy particle was cosmic rays. They allow the discovery of new particles such as the positron predicted by Dirac[88, 89] and observed by Andreson[42], then confirmed by Blackett and Occhialini [67]. In 1936, a charged particle with mass intermediate between proton and electron was discovered by Anderson and Neddermayer [43], they called it "mesotrons" believing it was the particle predicted by Yukawa in 1935 [218]. Pions were discovered more than 10 years later by Lattes et al in 1947 [156], confirming Yukawa's prediction. The "mesotrons" were actually leptons known today as "muons". Kaons were discovered the same year by Rochester and Butler [190]. Then, astroparticle detector started to be sent in balloon and in space, allowing precise detection of particle properties and spectra reconstruction.

2.2 Cosmic rays spectrum

Cosmic rays spectrum was measured from hundred MeV up to 10^{20} eV all over the years. It extends over 12 orders of magnitude in energy and 32 orders of magnitude in intensity. To describe the cosmic rays spectrum, we will use a terminology that we want to introduce once for all here :

$I(E)$ **:** Particle intensity is the number of particles N with energy E crossing a unit area per unit of time and in a unit solid angle. it has a dimension of $[I(E)] = [E]^{-1}[L]^{-2}[T]^{-1}sr^{-1}$. If the intensity is isotropic the flux $F(E)$ through a planar detector would be $F(E) = \pi I(E)$

$n(e)$ **:** The differential number density of cosmic rays with velocity v is $n(E) = \frac{4\pi}{v} I(E)$

$E^{\alpha} I(E)$ **:** it is interesting to multiply the intensity by a power of E in order to flatten the plot and make the features in the spectrum more visible.

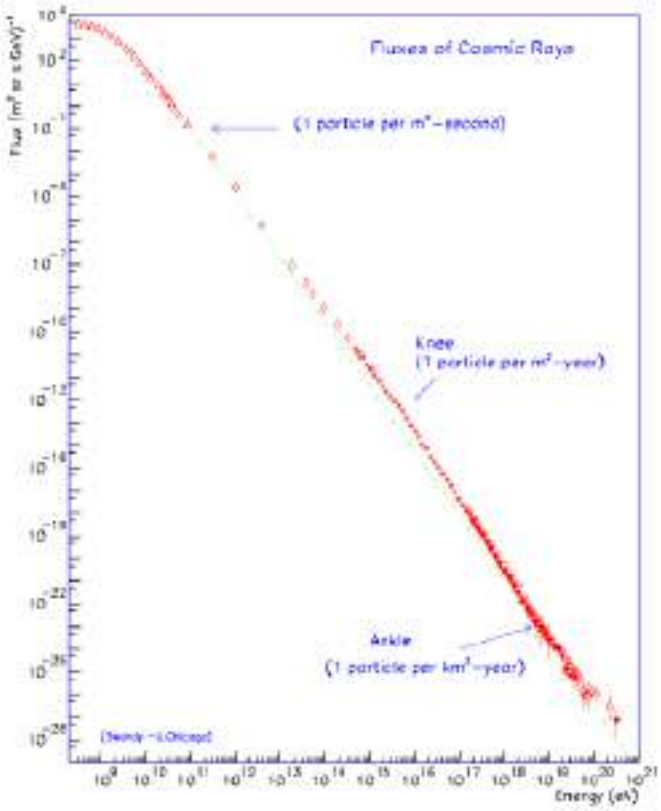

Figure 2.1: The all particle cosmic ray spectrum with reconstructed energy from 10^8 to 10^{21} eV, as measured by various experiments.

R Regidity $R = E/Ze$ and for ultra-relativistic particle $R \simeq pc/Ze$. It is expressed in Volts. The rigidity is an interesting quantity to describe CR because two particles with same rigidity will behave the same way in a given magnetic field.

Figure 2.1 represents cosmic rays energy spectrum, it appears that the cosmic rays spectrum follows a power law with high regularity with a slope of $2.5 - 2.7$. If we multiply the intensity by E^3 as shown in figure 2.2, we can distinguish some remarkable features :

Knee : The spectrum breaks at $E = 3 - 4$ PeV where the slope goes from 2.7 to 3.1, this steepening (softening) is called "knee". A second knee

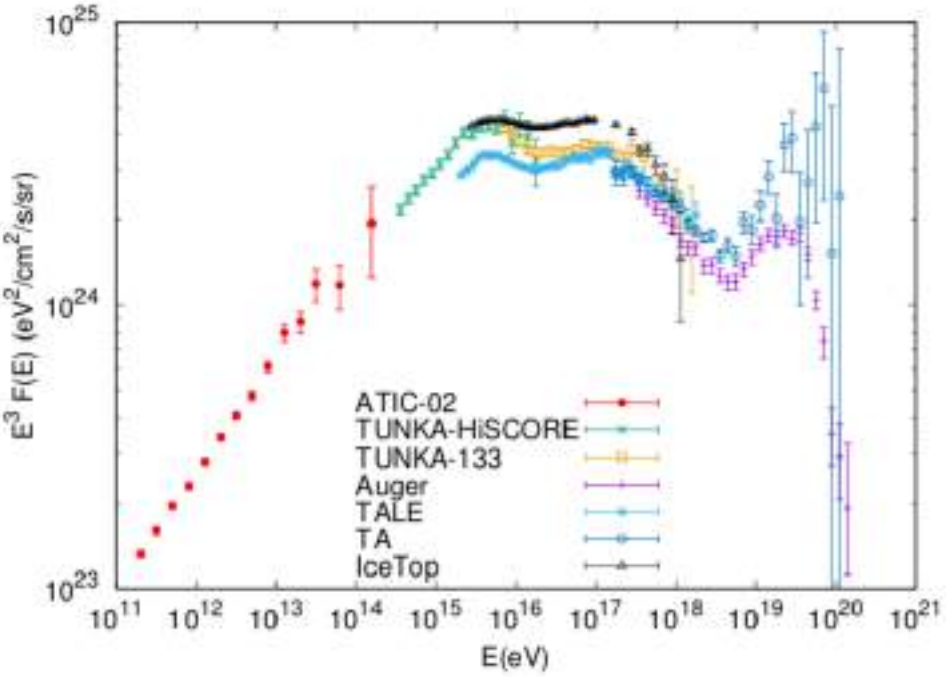

Figure 2.2: The all-particle CR spectrum multiplied with E^3 as function of energy together with experimental data TUNKA [182] , TUNKA-HiSCORE [206], IceTop [185] , TALE [12] the PAO [207], and the TA [9], plot was taken from [137].

was observed at $E = 5 \times 10^{17}$ eV, as shown in figure 2.2. Other knee-like features happens at lower energies, as the one shown in figure 2.8 which was first observed by NUCLEON at $\mathcal{R} \simeq 10$ TV [118, 52] and confirmed by DAMPE[40] .

Ankle : The opposite of the knee happened at $E = 3 - 4$ EeV, where the slope goes again to 2.6, this flattening (hardening) in called "Ankle", see figure 2.2.. This feature is usually described as being either the transition between galactic and extragalactic CR sources, or as an existing feature in CR extragalactic spectrum.

GZK cutoff : Greisen-Zatsepine-Kouzmine cut-off is the limit energy of observable extragalactic CR happening at $\sim 4 - 5 \times 10^{19}$ eV. This

suppression is due the their interaction with CMB photons. This effect was predicted one year after the discovery of CMB in 1966. This means that at the highest energies, only local sources within $\sim 100\,\mathrm{Mpc}$ can contribute to the observed UHECR [137].

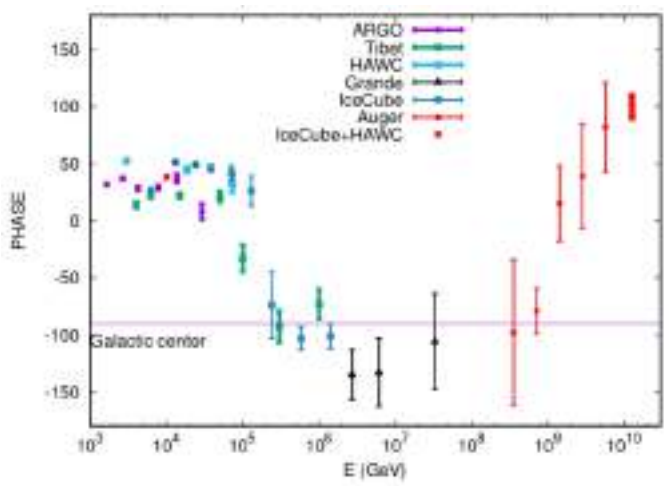

(a)

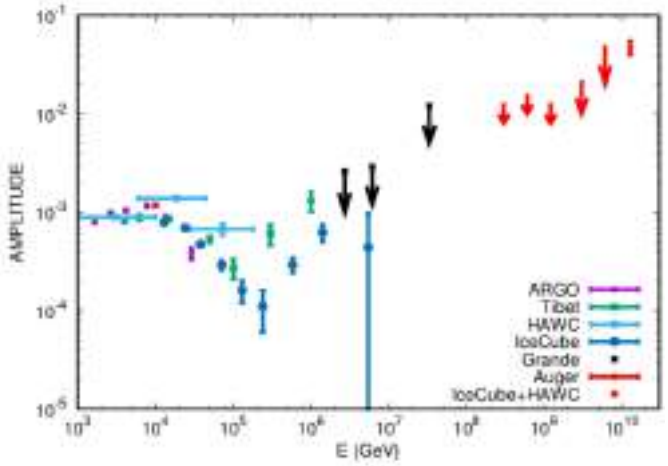

(b)

Figure 2.3: The phase and the amplitude of the dipole component of the CR anisotropy as a function of energy as measured by ARGO [57], Tibet [35, 37] , HAWC [14] , IceCube [6], combining HAWC and IceCube [82], KASCADE-Grande [78] and the PAO [1], the figure was taken from [137]

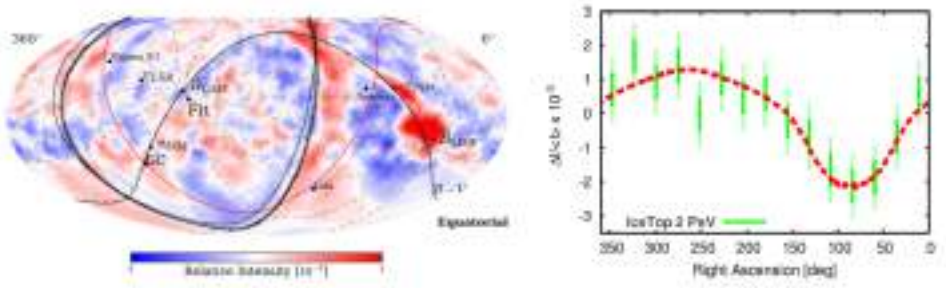

Figure 2.4: Left panel: All-sky map of the CR intensity combining HAWC and IceCube data at 10 TeV median energy after subtracting multipoles with $l \leq 3$. The magnetic equator as the plane containing the magnetic field in the local ISM [221] is shown as a black curve, the Galactic plane as a red curve and the positions of two nearby SNR, Geminga and Vela, are indicated too; adapted from Ref. [13]. Right panel: The relative intensity projected on the equatorial plane as function of right ascension at 2 PeV, adapted from Ref. [114]. Figure from [137]

Then Angular spectrum of cosmic rays shows that the arrival directions of CR are quite isotropic, from figure 2.3 we see that the anisotropy amplitude is very low $\sim 10^{-3}$. The turbulent magnetic field succeeds to isotropises the galactic cosmic rays. Highest energy cosmic rays are believed to be extragalactic, the anisotropy phase plot suggests a transition around 10^8 GeV.

Nevertheless, at high energies some features appear, as in figure 2.4 where we can see from the sky map on the left panel, the existence of higher multipoles in addition to the expected dipole anisotropy. In the right panel of the same figure, it is clear that the shape of anisotropy deviates from the cosine shape expected for a pure dipole.

2.3 Cosmic rays experiments

A huge number of experiments participate to build cosmic rays energy and angular spectrum. The used techniques depend on the probed energy range. We saw from cosmic rays energy spectrum that the expected flux varies on

more than 30 orders of magnitudes. For lower energy particle, we could reach enough statistics with small detector since we expect to observe at *hundred* GeV more than 1 particle/m^2/s, CRs are detected directly at very high altitudes. At higher energies the probability to detect CRs becomes smaller, one needs to build bigger detectors to be able to run an experiment in a reasonable amount of time, hence observations operate from ground based telescopes using air shower produced by CR in the atmosphere to reconstruct the primary particle properties. This is why detection methods are divided into two categories : Direct and Indirect measurements.

2.3.1 Direct measurement

The direct measurement takes place in space craft or balloon experiments, where the particles don't suffer extinction due to atmosphere and still can be observed while they travel through the detector. Putting detectors at high altitudes put constraints on its possible size and weight, thus on the CR energy probed. Direct measurement observes particles up to 10^{14} eV and permits to measure the energy, mass, charge and the incidence direction of the particle with high precision. Here is a non exhaustive list of direct measurement detectors.

AMS-02 Alpha Magnetic Spectrometer-02 is a space experiment deployed on 2011 on the international space station. It is the first experiment to provide high precision energy spectrum of CR protons and nuclei up to $R \sim$ TeV. In the following we will describe the AMS-02 detector as an example for direct measurements. Figure 2.5 shows the composition of the AMS-02 detector, we can distinguish different elements. At the top there is the Transition Radiation Detector (TRD) that allows to discriminate electron and positrons from protons and antiprotons

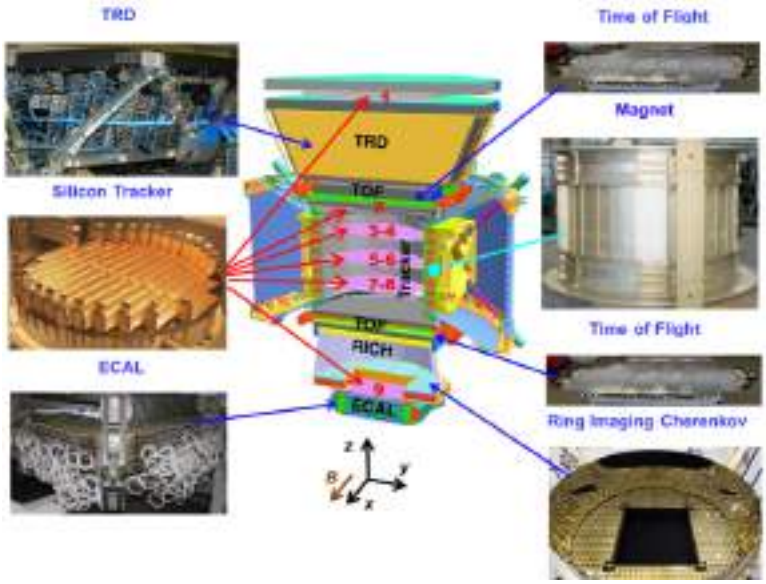

Figure 2.5: The AMS detector showing the main elements and their positions in the space craft.[79]

through the emission or not of radiation while crossing the detector medium. Then particles trajectories are traced by the Silicon Tracker. The rigidity of the particle is measured from its curvature under the effect of the magnet, since $r_L = p/ZeB$. The tracker is put between two planes, measuring the Time Of Flight (TOF) , allowing to measure the particle velocity by computing the time it took to travel from one plane to the other, and to deduce the charge of the particle from Z = 1 to Z = 30 via ioniziation energy loss detection $\frac{dE}{dx} = \text{fct}(\beta, Z)$, see figure 2.6, it also allows to discriminate between upward and downward going particles. AMS-02 also includes an imaging Cherenkov detector that measures the particle velocity from the Cherenkov angle with $\cos(\theta_c) = 1/\eta\beta$, and its charge since Z^2 is proportional to the radiation intensity. And finally, and electromagnetic calorimeter that computes the energy of electrons and positrons with high precision. An anti-coincidence counter is also added in order to eilminate unwanted particles that do

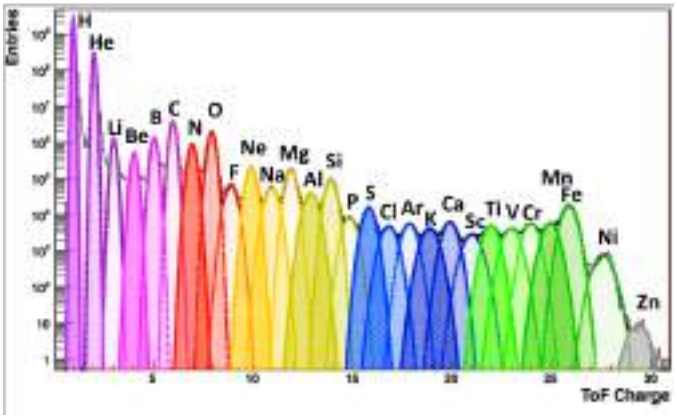

Figure 2.6: The charge distribution as measured by time of flight detector in AMS-02. Z goes from proton (Z=1) to Zinc (Z=30)[79].

not cross the detector in the optimal direction [79].

CREAM Cosmic Ray Energetics And Mass uses ultra long balloon flights to measure CR spectra. It uses detection techniques equivalent to AMS but designed to reach higher energies. It has had 7 successful flights, from 2004 to 2016, allowing it to be the first direct experiment to extend CR spectra up to $R \sim 10^{13} - 10^{14}$ V. CREAM was also the first experiment to detect helium excess at multi-TeV [32].

NUCLEON is a space experiment that was designed to study the chemical composition and energy spectra of galactic cosmic ray nuclei from protons to zinc at energies of $10^{11} - 10^{15}$ eV per particle. The detector was installed on the "Ressource P" satellite and start collecting data on 2015. The main particularity of NUCLEON detector is the implementation of two different particle energy measurements, the first uses an ionization calorimeter, and the second is the KLEM (Kinematic Light weight Energy Meter). The latter method has been used for the first time in NUCLEON experiment. KLEM consist of measuring the multiplicity of secondary particles after the first nuclear interaction of

the primary CR, this allows a cross check of energy measurements.[50] This technique allows NUCLEON to gain in precision at higher energies and thus to detect for the first time the knee-like feature at R = 10 TV with 4σ [51].

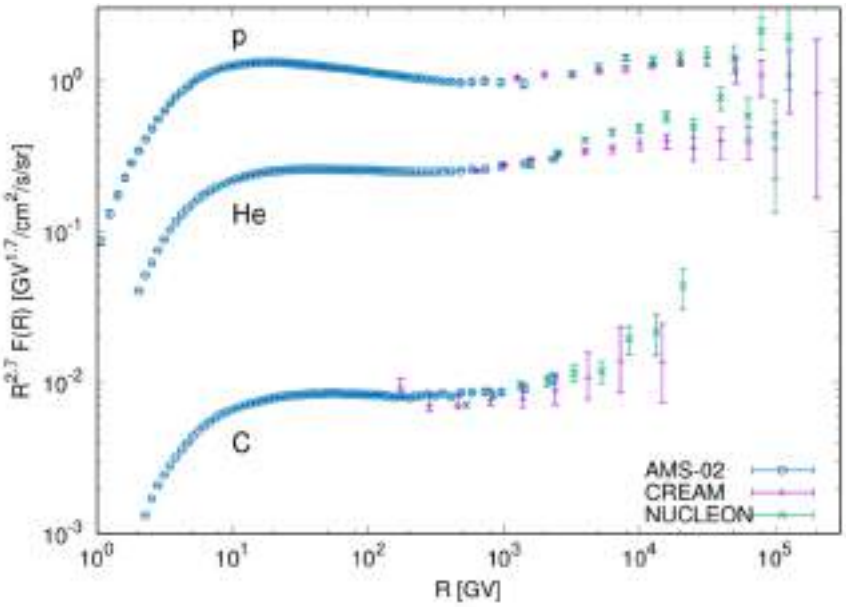

Figure 2.7: The spectrum of proton, helium and carbon as a function of rigidity, measured by the AMS-02 [23, 25], CREAM [216] and NUCLEON experiments [117, 52].Figure token from [137].

DAMPE DArk Matter Particle Explore is also a satellite mission, launched in 2015. In addition to plastic scintillator, silicon tracker and a calorimeter, it has a neutron detector in order to improve the electron/proton separation. It improved considerably the spectrum resolution from TV to hundred TV rigidities, confirming the knee-like feature observed by NUCLEON [40], as seen in figure 2.8.

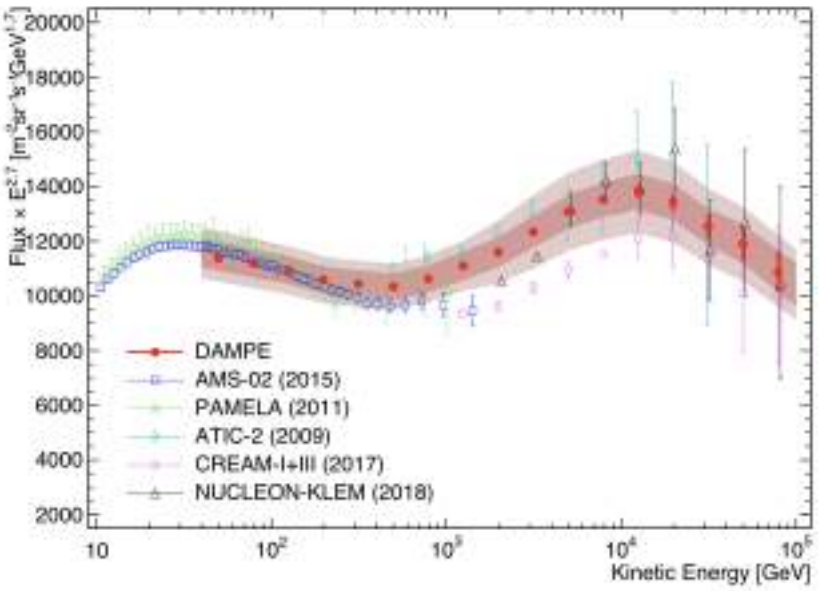

Figure 2.8: Proton spectrum from 40 GeV to 100 TeV measured with DAMPE [40]. together with other direct measurements by PAMELA [20], AMS-02[23] , ATIC-2 [179] , CREAM I + III [216], and NUCLEON-KLEM [51] .

2.3.2 Indirect measurement

Above $\sim 10^{14}$ eV, it gets hard to conduct experiments outside the terrestrial atmosphere because of the size of the detector. At high energies the cosmic-rays flux is reduced, requiring large detectors to reach a reasonable rate of events. All experiments have to be ground based, the observed particles don't reach the detector, they interact in the atmosphere producing cascades. The idea of indirect measurement is to use the atmosphere as a calorimeter and to deduce CR properties through their interaction cascade, called "Extensive Air Shower (EAS)". This detection method presents the inconvenient to be dependant on hadronic models and therefore it lacks precision in measuring mass, energy, direction and particle identification. Before presenting

experiments using EAS, we will briefly present the detection technique.

Developpement of electromagnetic air shower

In the case of electromagnetic shower, there is two leading processes $\gamma \rightarrow e^- + e^+$ and $e \rightarrow e + \gamma$. If we assume that in each case the energy is divided by 2, so the energy at a depth X : $E(X) = E_0 \exp(-\frac{X}{X_0})$, where X_0 is the distance travelled in the atmosphere before the first interaction, and E_0 is the initial energy of the incident particle. The electromagnetic shower stops when ionization dominates bremsstrahlung i.e $E(X) \leq E_c \approx 85\,\text{MeV}$. We can then deduce the depth at which the maximum of the shower development occurs as a function of the initial energy

$$X_{max}(E_0) = X_0 \ln(\frac{E_0}{Ec}) \tag{2.1}$$

By inverting this expression, we can see that with this simple hypothesis, we can compute the energy of the incident particle from the depth of the electromagnetic shower in the atmosphere.

Developpement of hadronic air shower

A hadronic shower is driven by pions $pp \rightarrow \sum \pi^+, \pi^-, \pi^0$ and each pion can either interact or decay.

$$\pi^{\pm} p \rightarrow \sum \pi^+, \pi^-, \pi^0 \qquad \text{if } E \geq E_{dec} \tag{2.2}$$

$$\pi^{\pm} \rightarrow \mu^{\pm}, (\bar{\nu_\mu}) \qquad \text{if } E < E_{dec} \tag{2.3}$$

$$\pi^0 p \rightarrow \sum \pi^+, \pi^-, \pi^0 \qquad \text{if } E \geq E_{dec} \tag{2.4}$$

$$\pi^0 \rightarrow \gamma\gamma \rightarrow \text{electromagnetic shower} \qquad \text{if } E < E_{dec} \tag{2.5}$$

Where E_{dec} is the energy where charged pions start to decay before interacting.

We can see that at the end of the shower there is 3 important obeservables : the depth at which the shower reaches its maximum X_{max}, the number of electrons N_e (from π^0) and the number of muons N_μ (from $\pi^\pm$). If we define n_{tot} the multiplicity at each step of the shower we have

$$N_\mu \simeq (\frac{E_0}{E_{dec}})^\alpha \tag{2.6}$$

where $\alpha = \frac{\ln(2/3\ n_{tot})}{\ln(n_{tot})}$, and

$$X_{max}(E_0) = X_{had}(E_0) + X^{em}_{max}(\frac{E_0}{n_{tot}}) \tag{2.7}$$

Where $X_{had}(E_0)$ is the depth of the first interaction and X^{em}_{max} is the value of X_{max} for electromagnetic showers.

Nuclei induced shower

One way to view a nucleus of mass number A and energy E_0 is as a superposition of A protons with energies E_0/A we then directly have under this approximation :

$$N^A_\mu(E_0) = A^{1-\alpha}(\frac{E_0}{E_{dec}})^\alpha \tag{2.8}$$

$$X^A_{max}(E_0) = X^{proton}_{max}(\frac{E_0}{A}) \tag{2.9}$$

An important difference induced by this superposition of showers is the spread of X_{max} distribution. Indeed, for A showers we expect

$$\sigma^{A}_{X_{max}} \simeq \frac{\sigma^{proton}_{X_{max}}}{\sqrt{A}} \tag{2.10}$$

The heavier is the particle the narrower is the spread of X_{max} and this plays a role in particle identification.

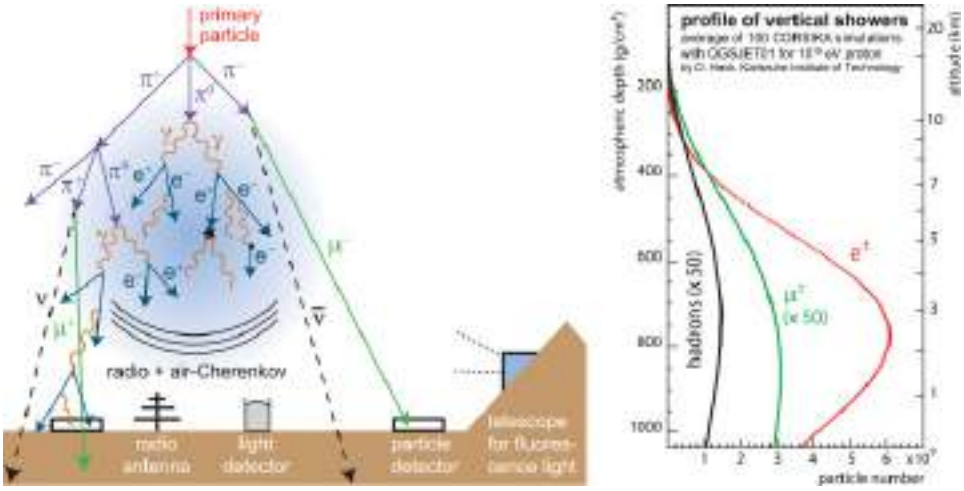

Figure 2.9: Left panel : schematic figure showing the development of a hadronic air shower at different steps together with the different EAS telescopes component, Right panel : shows the development of the number of particles as a function of depth [191].

Exemple of experiment

We will present a few of the most known experiment using indirect measurement of very high energy and ultra high energy cosmic rays (VHECR and UHECR)

KASCADE and KASCADE GRANDE KASCADE is a large area detector conceived to study CR around the knee. The experiment is situated on Karlsruhe Institute of Technology. It started measuring

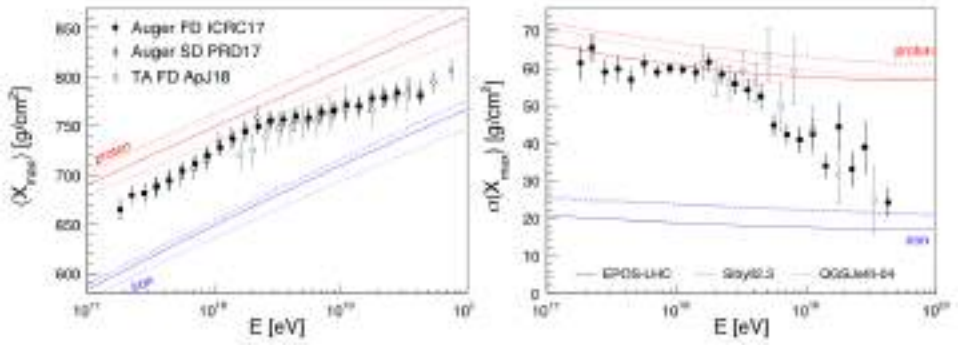

Figure 2.10: Measurements [12, 61] of the mean (left) and standard deviation (right panel) of the distribution of shower maximum as a function of energy. The energy evolution of the mean and standard deviation of Xmax obtained from simulations [66] of proton- and iron-initiated air showers are shown as red and blue lines, respectively; from Ref. [181]. Figure from Ref. [137].

CR in 1996, then from 1987 to 2000, it was extended and became KASCADE Grande. It measured simultaneously the electromagnetic, muonic and hadronic components of extensive air showers of cosmic rays. It was the first experiment that presented energy spectra for individual groups of elements [46].

TAIGA (Ex Tunka) The TAIGA experiment(Tunka Advanced Instrument for cosmic ray physics and Gamma Astronomy) in situated in Siberia in the Tunka valley close to lake Baikal. Tunka started in 1990, with a small array of photomultipliers. It was first updated by the construction of 133 detectors in 2009, then a second extension where the gain a factor 4 in size happened in 2011, which allows it to reach CR energies close to 0.1 EeV. In 2012 Tunka-Rex and Tunka-HiSCORE were installed. Tunka Grande was built in 2014 and it now includes gamma rays and becomes TAIGA.

Tibet AS γ is an air shower array which consists of 697 scintillation counters at Yangbajing (4300m above sea level) in Tibet. It is dedicated

to measurement of the energy spectrum and chemical composition of very high-energy primary cosmic rays. Tibet contributes considerably in measuring CR spectrum and composition in the intermediate energy region between direct and indirect measurements, starting from $R = 10\,\mathrm{TV}$. This improvement was made possible in part thanks to the high altitude of the detector. CR chemical composition measurement from Tibet AS γ suggest an earlier suppression of proton flux at around 500 TeV [39].

IceTop Is an air shower detector at the South Pole. It consists of 162 tanks of ice, each instrumented with two standard IceCube sensors, to detect showers of secondary particles generated by interactions of high-energy cosmic rays in the atmosphere. It can detect CR from 100 TeV to 1 EeV. It is well designed for studying the CR second knee and CR anisotropy [185]. The deployment starts on 2000 and it was fully deployed in 2011.

Pierre Auger observatory (PAO) It is an extensive air shower detector array of 1660 surface detector stations extending over 3000 km^2, each detector is a tank filled with purified water and photomultipliers to detect Cherenkov light. It also contains 27 fluorescence telescopes that detect light produced in the atmosphere during the shower production. It was first conceived by Jim Cronin, Alan Watson and other scientists in 1991. It was the largest telescope to probe ultra high energy CR and thus the first to observe CRs ankle and the GZK cutt off with high precision. It also observed for the first time a steepening at about $10^{19}\,\mathrm{eV}$ in the energy spectrum, see figure 2.11.

Updates of the detector are planned in order to extend detections to low energies up tp $\sim 10^{17}\,\mathrm{eV}$ by installing muons counters underground.

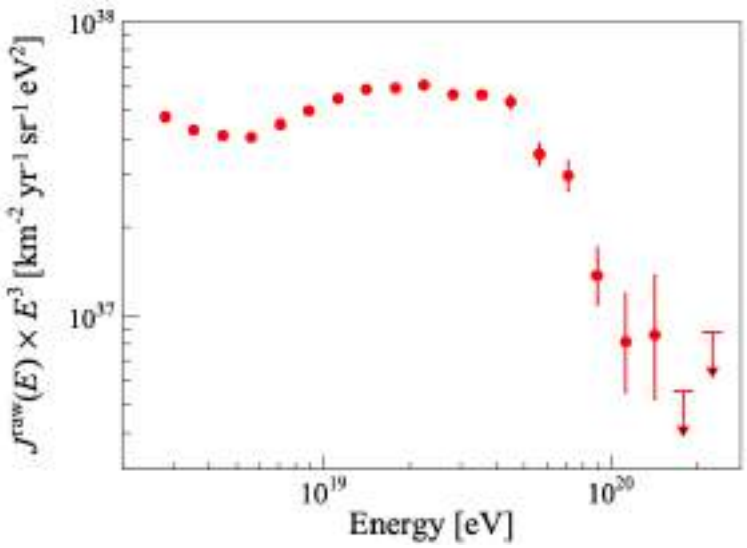

Figure 2.11: Spectrum of ultra high energy cosmic rays measured by Auger [2].

The detector will also be updated by adding a Radio Detector that extends the vertical shower techniques developed in earlier radio arrays, to horizontal showers, with a precision that is expected to be similar to existing ground array techniques. It will provide a novel measurement for inclined showers, complementary to the other techniques.

Telescope Array is designed to observe air showers induced by cosmic rays with extremely high energy, greater than 10^{18} eV. Using a combination of ground array and air-fluorescence techniques. It consists of more than 500 scintillator detectors distributed over 300 square miles of desert in Utah.[81] TA has been collecting data since 2007, and is now extended with "TALE" to probe lower energies CR. TALE The Telescope Array Low Energy Extension (TALE) aim to extend the sensitivity in energy of the Telescope Array (TA) by adding 10 new high elevation angle telescopes, viewing up to 72°, to one of the telescope stations and adding a graded infill array of scintillator surface

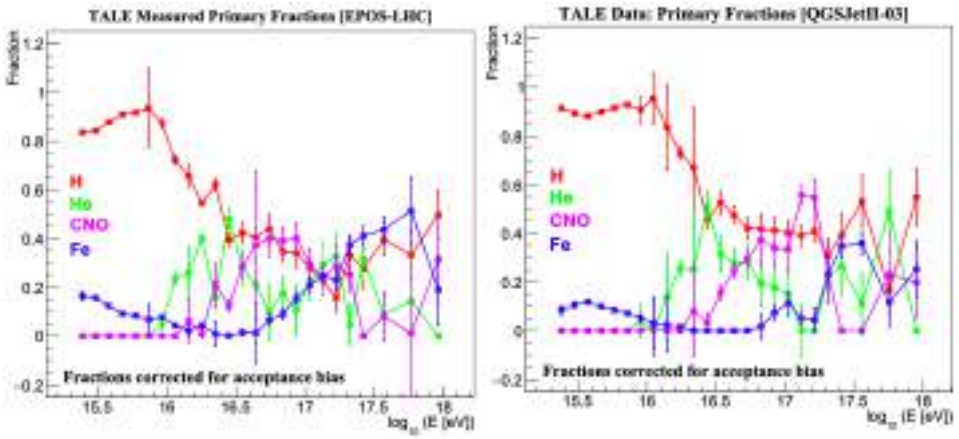

(a) (b)

Figure 2.12: Fit results to the data Xmax distributions (per energy bin) to a four component MC distribution. Primary fractions using the EPOS-LHC based simulations are shown in *(a)*, Those using QGSJetII-03, in *(b)*. Figure from Ref. [11]

detectors. It will detect particle from $E = 10^{16.5}$ eV. The aim of the experiment is to study the second knee, the ankle, and the galactic/extragalactic transition spectra and composition [204]. Figure 2.12 shows that TALE observe a proton rich knee and a mixed composition up to the ankle.

2.4 Composition of cosmic rays

The study of precise chemical composition of cosmic ray was allowed by the presence of direct detector able to perform with high precision the particle identification. Cosmic rays composition is very rich, it is dominated by protons but contains also heavy ions and antimatter. It is interesting to compare chemical composition of cosmic rays with sun abundance, which looks for the majority of elements similar as seen in figure 2.13. This gives a hint of cosmic ray's origin, and suggests that the stars may be cosmic rays

fuel. However, we can notice exceptions in this similarity. For instance a considerable amount of boron can be found in cosmic rays composition, but not in the sun abundances. In fact, nuclear process in stars don't favour boron production, it is instantly transformed into heavier and more stable elements. The common explanation for boron excess in cosmic rays composition is that it is produced by spallation of heavier cosmic rays such as oxygen and carbon. At this point we can separate cosmic rays population into two categories, primaries, made of galactic matter and accelerated through astrophysical process and injected in ISM with high energy; and secondaries, result of primary cosmic rays interaction.

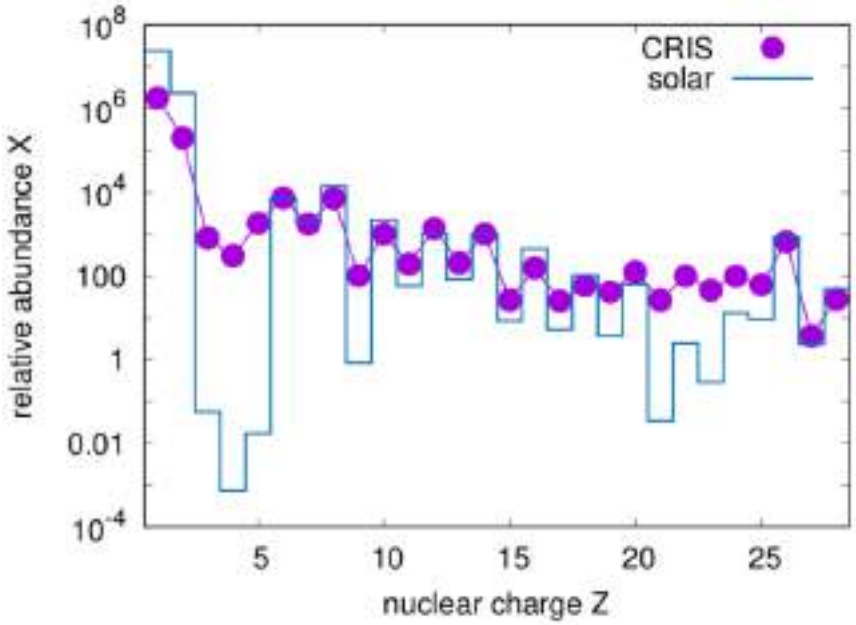

Figure 2.13: Relative abundances X normalised to X(Si) = 1000 from Ref. [158] versus the abundances in CRs measured by BESS [212] and CRIS [87, 107].

2.5 Acceleration of cosmic rays

We previously described cosmic rays spectrum and saw that cosmic rays can reach energies as high as 10^{20} eV, these extraordinary energies could not be explained by thermal phenomena. An efficient acceleration mechanism should be responsible for cosmic rays acceleration. Cosmic rays being charged particles, they could be accelerated by an electric field $\vec{E}$, however the mean electric field in the Galaxy is 0. In many astrophysical objects one can expect the presence of electric field induced from a local variation of magnetic field, as in solar flares or in the vicinity of a neutron star. Another way to see this generated $\vec{E}$ from moving $\vec{B}$ is to apply a change in reference frame from a frame with $\vec{B} \neq 0$ and $\vec{E} = 0$ to a moving frame where $\vec{E} \neq 0$. Fermi has the idea of studying how a moving magnetised cloud could affect a high energy particle. Let's assume a charged particle with a velocity v in the galactic rest frame and a magnetised cloud moving at V in the same rest frame. The cloud is magnetised and had no electric field in his own rest frame. In the configuration of uniformly distributed clouds, this mechanism is called "second order Fermi mechanism", we can calculate the energy gained by the charged particle under this induced electric field

$$\frac{\Delta E}{E} = -2\frac{\vec{V}\vec{v}}{c^2} \tag{2.11}$$

We can easily see from equation 2.11 that this process accelerate particles only if $\vec{V}\vec{v} < 0$, so an efficient acceleration mechanism would be a mechanism where this condition is always fulfilled [1].

[1] Calculation are taken from Lecture notes [34]

Diffuse shock acceleration (DSA)

Astrophysical shocks can be produced in supernova remnant, active galactic nuclei and gamma ray burst and other catastrophic phenomena in the universe. The shock wave originates from outflows propagate faster than the sound in the medium. When a shock propagates we distinguish two regions "Downstream" which is the region that has already been shocked and that we will refer to in the following as "2", and the "Upstream" that hasn't been shocked yet and that we will refer in the following as "1".

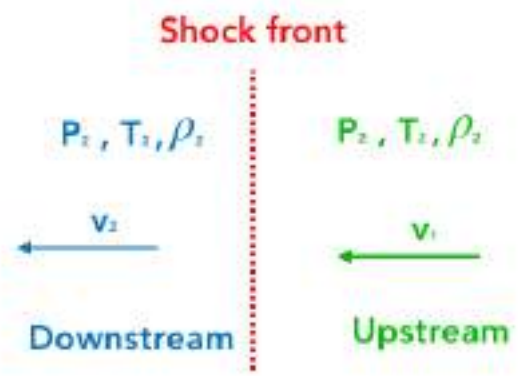

Figure 2.14: Schematic view of a shock wave propagating in a medium, as seen in the shock rest frame. The shock is at rest and the upstream medium is coming toward it with a velocity v_1 while the downstream medium is going away with a velocity v_2. Physical quantities are discontinuous through the (immaterial) surface of the shock

The physical quantities of theses two region are linked with "jump conditions", where ρ describes the density, P the pressure, T the temperature, and v the velocity of the medium in the shock rest frame, see 2.14 .

Mass conservation

$$\rho_2 v_2 = \rho_1 v_1 \tag{2.12}$$

Momentum flux conservation

$$P_2 + \rho_2 v_2 = P1 + \rho_1 v_1 \tag{2.13}$$

Energy conservation

$$\rho_2 v_2 (v_2^2 + \frac{P_2}{\rho_2} + e_2) = \rho_1 v_1 (v_1^2 + \frac{P_1}{\rho_1} + e_1) \tag{2.14}$$

e_i is the energy density given by $e_i = \frac{1}{\gamma_\alpha - 1}\frac{P_i}{\rho_i}$ for a perfect gas and γ_α is the adiabatic index $\gamma_\alpha = 5/3$ for monoatomic gas.

We introduce M_1 the Mach number which is defined as the ratio of the velocity of the upstream to the sound velocity in the upstream region $M_1 = \frac{v_1}{v_{1,sound}}$. When passing through the shock the fluid is compressed, heated, and slowed down. The compression factor r is defined as

$$r = \frac{\rho_2}{\rho_1} = \frac{v_1}{v_2} \tag{2.15}$$

$$\simeq \frac{\gamma_\alpha + 1}{\gamma_\alpha - 1}, \text{ for strong shocks where } M_1 \gg 1 \tag{2.16}$$

$$= 4, \text{ for monoatomic gas where } \gamma_\alpha = \frac{5}{3} \tag{2.17}$$

We then compute the energy gain per cycle.

$$< \frac{\Delta E}{E} >= \frac{4}{3}\beta_{sh}(\frac{r-1}{r}) \tag{2.18}$$

We can write

$$< \Delta E >= kE \text{ ,where } k = \frac{4}{3}\beta_{sh}(\frac{r-1}{r}) \tag{2.19}$$

So after n cycles we have

$$E_n = (1+k)^n E_0 \Leftrightarrow n = \frac{\ln(E/E_0)}{\ln(1+k)} \tag{2.20}$$

For $\beta_{sh} \ll 1$ and $k \ll 1$ we have the differential number density

$$n(E) = \frac{dN(E \geq E_n)}{dE} \tag{2.21}$$

$$\propto (\frac{E}{E_0})^{-\alpha}, \text{ where } \alpha = \frac{r+2}{r-1} \tag{2.22}$$

For strong shock and perfect monoatomic gas where ($\gamma_\alpha = 5/3$ and $M_1 \gg 1$) where have $r = 4$, hence $\alpha = 2$, otherwise $I(E) \propto E^{-2}$

2.6 Sources of cosmic rays

One of the biggest questions in astrophysics that remains unsolved is the possible sources of cosmic rays. On the theory side, several models have been proposed. We can classify these sources in two categories "top-down" and "bottom-up" . We will discuss briefly the two models then concentrate on the latter.

Top-Down model : These models are based on the hypothetical existence of new usable or meta stable supermassive particles such as super-symmetric particles. Cosmic rays would be in this case the decay or annihilation product of those supermassive particles. Therefore, these models predict large photon fraction, equal matter and anti-matter fluxes and the (almost) absence of nuclei [130].

Bottom Up models : These models assume the existence of astrophysical objects able to accelerate charged particles up to very high energies.

An important constraint to identify possible cosmic rays sources are the maximum energy attainable at the source. The Hillas criteria define the maximum energy in term of size and magnetic field strength of the source

$$E_{max} = (10^{18} Ze\beta)(\frac{R}{kpc})(\frac{B}{\mu G}) \tag{2.23}$$

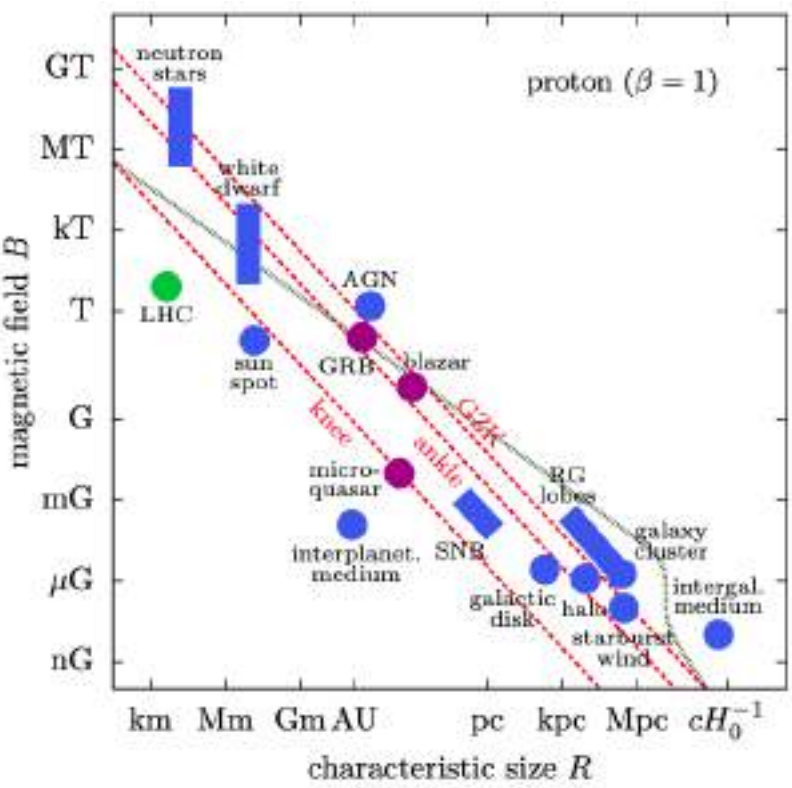

Figure 2.15: An adaptation of the Hillas plot from [4]. It displays upper limits on the reachable CR energy dependent on the size of the acceleration region and magnetic field strength. The red lines indicate the upper limits due to the loss of confinement in the acceleration region for CRs at the knee, ankle, and the Greisen-Zatsepin-Kuzmin (GZK) cutoff. The dotted gray line corresponds to a second upper limit that arises from synchrotron losses in the sources and interactions in the CMB.

Where Z is the charge of the particle, R the length scale of the source, β the acceleration efficiency. This condition stipulates that the parti-

cle should be confined in the source in order to be accelerated. If the cosmic rays Larmor radius is bigger than the source size it will escape the source. Fig 2.15 shows the acceleration capabilities of multiple astrophysical objects. A good accelerator needs either a strong magnetic field or a large length scale.

Another limitation of the maximum attainable energy came from the age of the source, the astrophysical environment is not in steady state, it is scalable and same are the sources. Thus, in case of DSA acceleration the source should give the time to particle to accomplish enough cycles to reach the wanted energy. Finally, we can think of the source as the one capable to provide the energy budget required by CR. The total luminosity of CR is estimated at $L_{CR} \simeq 5 \times 10^{40}$ erg/s. The most favoured CR source is supernovea remnant (SNe), first suggested by Baade and Zwicky [54]. We count in the Galaxy an explosion of more or less one supernova per 30 yr with a luminosity of $L_{SNe} \simeq 10^{51}$ erg/s, we then estimate the average output energy of SNe $L_{avr_{SNe}} \simeq 10^{42}$ erg/s. If less than 10% of the supernovae energy goes to CR acceleration, SNe could cover the CR total energy budget. It was shown in [60, 59], that in the case of efficient magnetic field amplification, SNe can accelerate particles up tp VHE ($\geq$ PeV) with an efficiency of $20\% - 30\%$ of its initial kinetic energy. Other possible sources can be cited such as superbubbles [180], which are bigger structures, where turbulence and multiple shocks could drive efficient particle acceleration. We can discuss also a possibly partial or total contribution to CR production of novae, which has smaller energy than SNe $\sim 10^{40}$ erg/s but much higher frequency of $\sim 100/$ yr; GRB which in he opposite of nova have much bigger energy but are very rare $\sim 10^{-4}/$ yr ; and the

GC supermassive black hole which has an estimated output energy of $1 - 7 \times 10^{42}$ ergs/s.

2.7 Propagation of cosmic rays

The propagation of the cosmic rays in the Galaxy is dictated by GMF, the charged particle is affected by both regular and turbulent parts of the magnetic field. While the regular gives a large scale propagation direction, the turbulent tend to spread CR in all other directions. We know that a relativistic charged particle with velocity $\vec{v}$ put in a magnetic field $\vec{B}$ will follow the equation of mouvment

$$\gamma m_0 \frac{d\vec{v}}{dt} = Ze(\vec{v} \times \vec{B}) \tag{2.24}$$

Where m_0 is the particle mass and γ its Lorentz factor. The particle has a circular motion around magntic field lines with a Larmor radius

$$r_L = 1.1 \quad \text{pc}(\frac{R}{\text{PV}} \times \frac{B}{\mu\text{G}})^{-1} \tag{2.25}$$

Where R is the particle rigidity as described in section 2.2. In the presence of turbulent magnetic field the behaviour of the charged particle follows a random walk. For a large population of cosmic rays, we usually treat them as fluid and we describe then the trajectory by a spacial diffusion tensor as follow

$$D_{ij}(x_0, R) = \lim_{t \to +\infty} \frac{1}{2Nt} \sum_{a=1}^{N} (x_i^a(t) - x_{i,0})(x_j^a(t) - x_{j,0}) \tag{2.26}$$

Where N is the number of propagated CR , $x_{ij,0}$ is the initial position of CR and $x_{ij}^a(t)$ the position at time t of the cosmic ray number a. The diffusion

coefficient parallel to the regular component can be computed analytically from the slope of the turbulent magnetic field power spectrum $P(k) \propto k^{-\gamma} \Rightarrow D_{\parallel} \propto R^{\delta}$ with $\delta = 2 - \gamma$. Ref [198] estimated $D_{\parallel}(R)$ at the numerical value of $D_{\parallel}(R) \simeq 2 \times 10^{27} (\frac{R}{\mathrm{GV}})^{1/3} cm^2 s^{-1}$ for a turbulent magnetic field following Kolmogorov turbulence with $B_{rms} = 5\mu\,\mathrm{G}$ and $L_{max} = 100\,\mathrm{pc}$. If we consider the simplest approximation so called " leaky box approximation" and if we assume that the Galaxy is spherical with radius R_{sphere} we can write the escape time as [2]

$$< \tau_{esc} > (R) \propto \frac{R^2_{sphere}}{D(R)} \tag{2.27}$$

If we ignore energy losses, we can write the following diffusion equation

$$\frac{\partial n(R)}{\partial t} = q(R,t) - \frac{n(R)}{\tau_{esc}(R)} \tag{2.28}$$

Where $q(R,t)$ is the source term and $n(R)$ is the number of cosmic rays of rigidity R in the Galaxy. In a steady state limit, we obtain

$$n(R) = q(R)\tau_{esc}(R) \tag{2.29}$$

So, Since $\tau_{esc} \propto D^{-1} \propto R^{-\delta}$, if $q(R) \propto R^{-\alpha}$ as produced is the DSA acceleration mechanism. We can write that

$$n(R) \propto R^{-(\alpha+\delta)} \tag{2.30}$$

The most common way used to probe diffusion properties of CR is to study secondaries to primaries ratios. Indeed , if we include interaction terms such as spallation for both primaries and secondaries diffusion equation, we

[2] Detailed calculation are available in lecture note [34]

could deduce the diffusion properties [3].

For large rigidities we have

$$\frac{n_s(R)}{n_p(R)} \propto X_{esc}(R) \propto R^{-\delta} \tag{2.31}$$

Where n_s is the number of secondaries, n_p the number of primaries, and X_{esc} is the escape grammage and is defined as the mean grammage crossed by the CR arriving on Earth $X_{esc} = \bar{m} n v \tau_{esc}$ for $\bar{m} \simeq 1.4 m_p$ the mean atomic mass of ISM, n the mean density and v the particle velocity. We often use boron to carbon ratio since by the composition study of cosmic rays, boron was absent in stars as sun, we deduce that all CR boron comes from spallation of carbon ions. Fig 2.16 shows that the most recent measurement agrees with $\delta = 1/3$ and are consistent with Kolmogorov turbulence prediction.

In a pure isotropic random field described by $P(k) \propto k^{-\gamma}$, we can express the diffusion coefficient as

$$D = \frac{cL_0}{3}[(\frac{R_L}{L_0})^{2-\gamma} + (\frac{R_L}{L_0})^2] \tag{2.32}$$

Where $L_0 \simeq \frac{L_c}{2\pi}$. We distinguish two diffusion regimes, a small angle scattering where $D(E) \propto E^2$ and a large angle scattering where $D(E) \propto E^{1/3}$ with a transition at E_{tr} where $r_L(E_{tr}) = L_0$

$$E_{tr} = 2 \times 10^{14} \text{eV} (\frac{L_c}{\text{pc}})(\frac{B}{\mu\text{G}}) \tag{2.33}$$

Fig 2.17 shows the diffusion coefficient calculated in a pure random field following Kolmogorov turbulence with $L_{max} = 25\,\text{pc}$ compared to extrapolation at higher energies of B/C ratio. It appears that the turbulent field with

[3] This is explained in more details in the review [137]

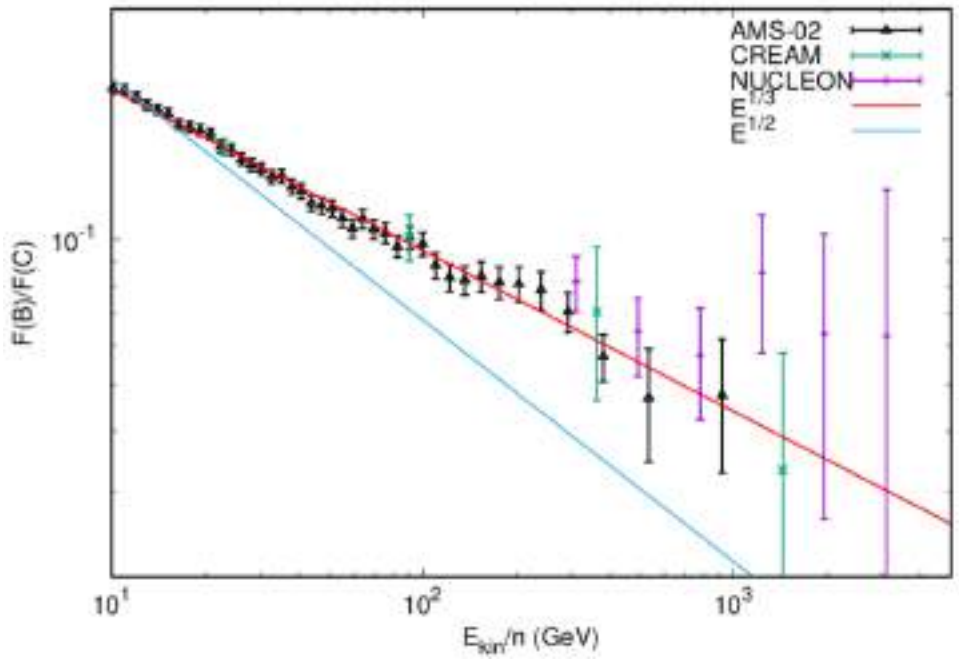

Figure 2.16: Boron-to-Carbon ratio from Ref. [137] as function of ketic energy per nucleon measured by the CREAM [31], AMS-02 [24], and NUCLEON [119] experiments. The power lax predicted by Kolmogorov turbulence ($E^{-1/3}$) and Iroshnikov-Kraichnan ($E^{-1/2}$) turbulence at high energies are also shown.

realistic strength alone is not capable of explaining boron to carbon ratio, CR propagation has to have an anisotropic component helping particle escaping. In fig 2.18, authors of ref [108], added a uniform magnetic field along z direction. They showed that for $B_{tot} = \sqrt{B_0^2 + B_{rms}^2} = 1\,\mu$G, a value of turbulent level $\eta = B_{rms}/B_0 = 0.5$ fits well B/C ratio extrapolation. This description of CR propagating through regular plus turbulent magnetic field in a steady state solution is simplified and neglect multiple effects that may appear in a more realistic picture, such as the coupling of CR with ISM that can drive galactic winds [71, 186], also CR streaming can lead to wave turbulence thus CRs, ISM and GMF form a coupled, non linear system [116, 96]. Another simplification made concerns the space evolution of magnetic field,

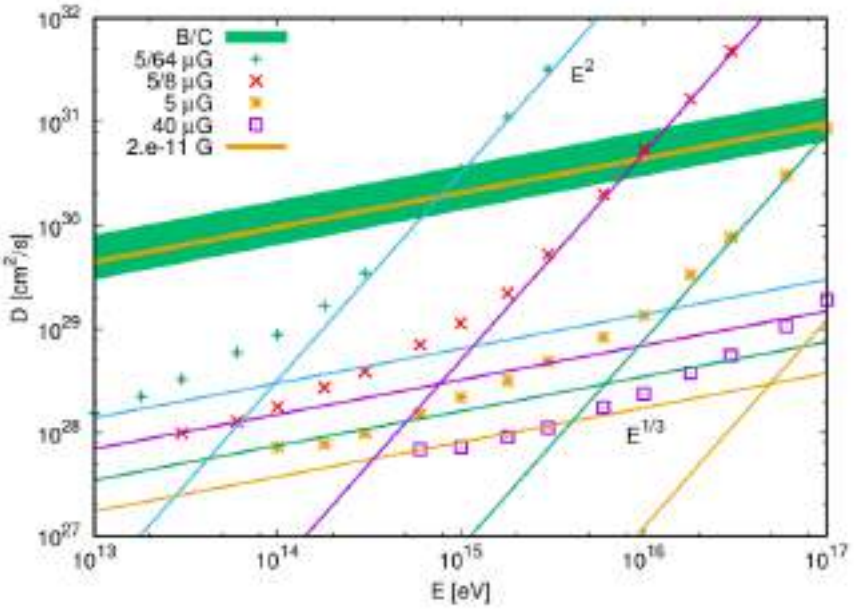

Figure 2.17: The CR diffusion coefficient in pure isotropic Kolmogorov turbulence with $L_{max} = 25\,\mathrm{pc}$ and for four values of The asymptotic behaviours at low and high energies are shown with the solid lines.[108]

in reality they are not static, but they move at alfven speed and thus induce a reacceleration of cosmic rays through second order fermi acceleration [90]. Finally, in addition to diffusion, CR experience advection due to the ISM motion that contributes in particle propagation. This effect was interpreted as responsible for B/C data flattening at GeV [128]. However ref [166, 165] shows that advection is in the case of Kolmogorov turbulence not necessary to reproduce the B/C data.

Ah higher energies other discrepancies emerge, such as the decrease and the flip of anisotropy amplitude between 10-200 TeV which is difficult to reconcile with the diffuse CR propagation through kolmogorov like diffusion [137]. Finally, breaks in the rigidity spectrum and deviation from rigidity dependent power law were observed, especially by CREAM and AMS-02 on proton and helium spectra, where it was found that $\gamma_{p/He} = -0.077 \pm 0.02$[22]

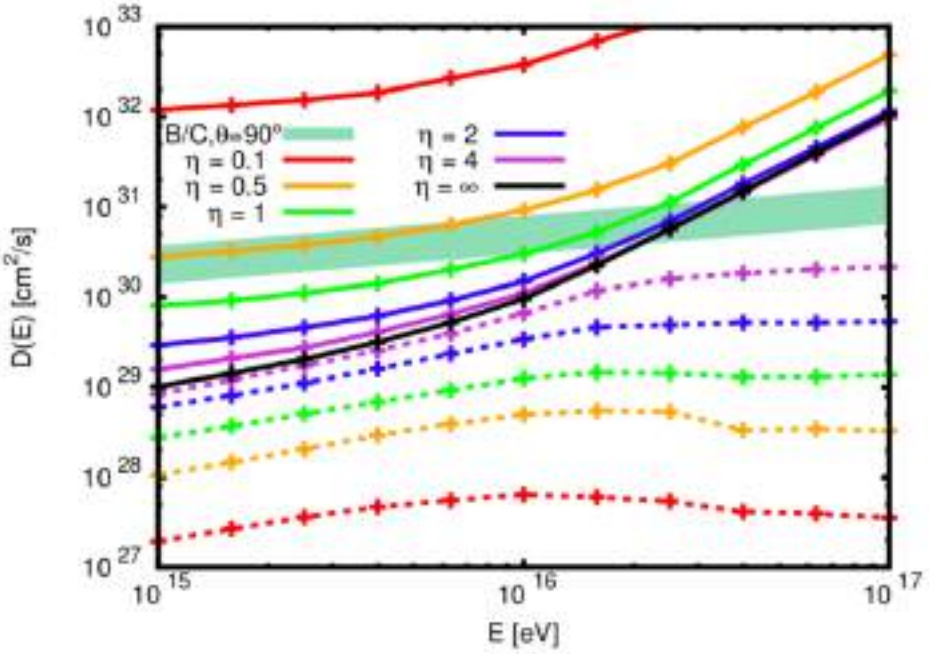

Figure 2.18: Parallel and perpendicular diffusion coefficient for isotropic turbulence with a regular field. [108]

2.8 Cosmic rays knee

As discussed previously, the cosmic rays spectrum present multiple features that are enhanced when plotting the intensity multiplied by a power of energy as $E^3 I(E)$. At $E = 4\,\text{PeV}$ a pronounced break occurs changing the power spectrum from $\beta = 2.7$ to $\beta = 3.1$, shown in figure 2.2. Another remarkable break takes place at $5 \times 10^{17}\,\text{eV}$, where the slope again softens by $\Delta\beta \simeq 0.2$.

CR 4 PeV knee was first discovered in 1958 by Kulikov and Khristiansen [152], and then deeply studied by various experiments. The detection of CR above 10^{14} is indirect, thus the particle identification is more complicated. Nuclei with close masses are summed in groups p, He, CNO (referring to intermediate mass nuclei), FeSi (including all heavier elements), this difficulty

leads to uncertainty in the composition of the first $E = 4 \times 10^{15}$ eV and the second $E = 5 \times 10^{17}$ eV knee.

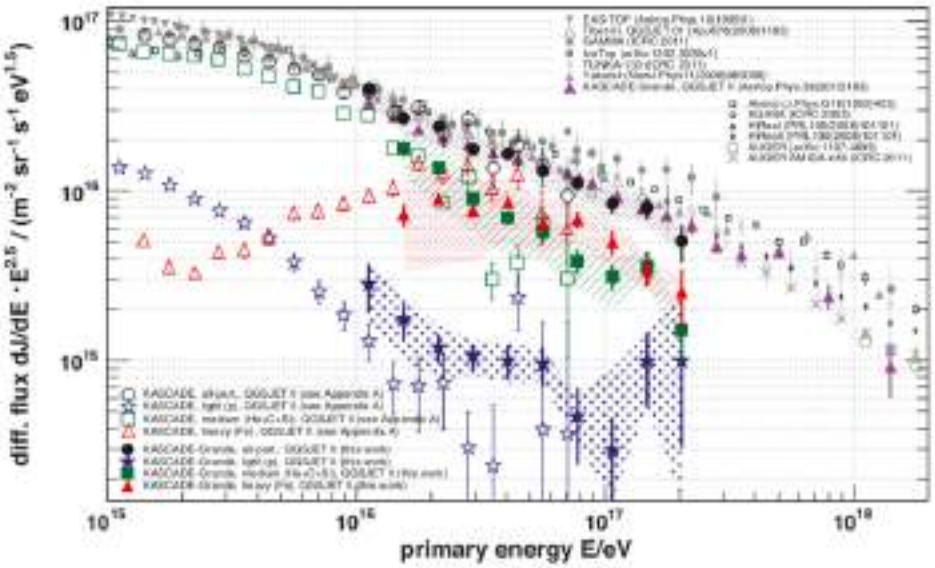

Figure 2.19: The CR spectrum of few elemental groups deduced from KASCADE and KASCADE-Grande date using QGSJET-II, from Ref.[47]

KASCADE and KASCADE GRANDE were the first experiments to present the $E_k = 4\,\text{PeV}$ as the proton knee, heavier elements would be then responsible for rigidity dependent knees with $E_k^Z = ZE_k^p$ as shown in figure 2.19.

More recent results of experiments such as CASA-MIA, BASJE-MAS, and Tibet, tend to suggest proton suppression before the knee at $E = 500\,\text{TeV}$, see figure 2.20.

Determining the knee composition is very important for understanding its origin.

2.8.1 Possible explanations of the knee

Models explaning the knee falls into 3 categories :

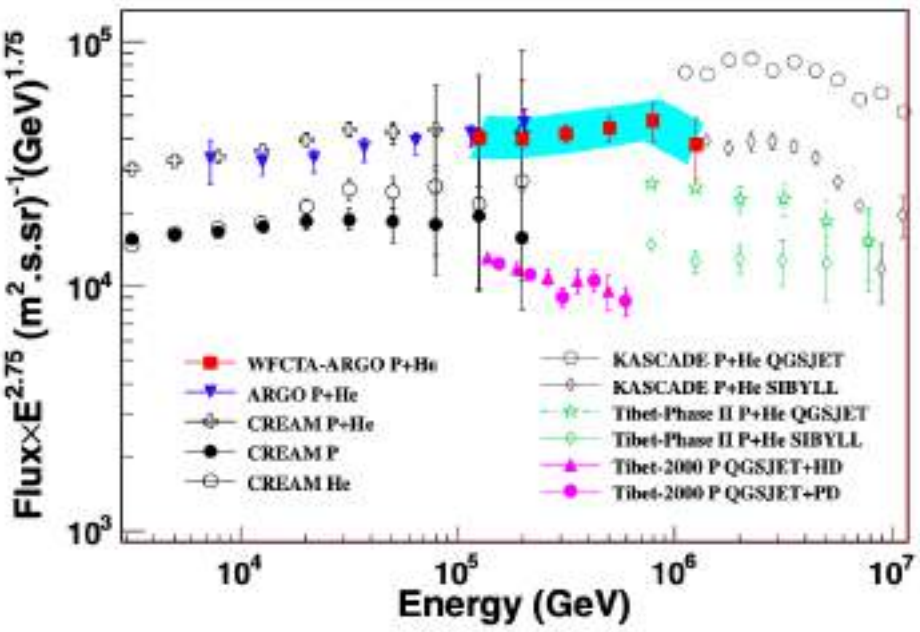

Figure 2.20: Figure from Ref. [220] Spectra of cosmic ray protons and helium nuclei between 3 TeV and 10 PeV from ARGO-YBJ experiment [56], CREAM experiment [32], Tibet AS γ [39, 38] , KASCADE [45].

- Resulting from hadronic interaction changes
- Connected to propagation changes of cosmic rays
- Due to acceleration limits of sources

The first explanation is based on a sudden change in hadronic interactions above knee, corresponding to 2 TeV in the center of mass system, leading to new energy loss channel and hence affecting CR spectrum. These possibilities were excluded by LHC, which have not revealed any strong deviation in hadronic interaction.

The second class of possibilities was suggested by Syrovatsky in 1971[201], where the knee is explained as caused by an increased leakage of CR. We saw from equation 2.32 that the diffusion of cosmic rays has two regimes: small scales angle scattering ($D(E) \propto e^2$), and the large angle scattering

($D(E) \propto E^{1/3}$); the transition happens at the energy E_{tr}

$$E_{tr} = 2 \times 10^{14}\text{eV}(\frac{L_c}{\text{pc}})(\frac{B}{\mu\text{G}}) \tag{2.34}$$

For $B \simeq$ few μG and $L_c \simeq 100\,\text{pc}$ the transition energy E_{tr} $\simeq$few $10^{16}\,\text{eV}$. Ref [184, 73] studied the transition between the dominance of pitch angle scattering to drift along regular field as being a possible explanation of the knee. Ref [111, 112] proposed a different approach to escape model. They connected the knee with a change in the propagation of galactic CR but with the difference of not calculating diffusion of all CR but by calculating trajectories of individual CR and they found a knee like structure at E/Z =few PeV for $L_c = 2 - 5\,\text{pc}$.

The third and last hypothesis emitted to explain the knee connects it with acceleration or source properties. The first possibility is that the knee correponds to the maximal attainable energy by a source population. We can cite two models explaining the knee as a transition region between two source populations, one by Hillas [124] and another by Zatspin et al [219]. A variation of Hillas model assumes 4 populations of sources, one accelerating up to 120 TeV, the second up to the knee, and two extragalactic sources dominating the flux at higher energies [106]. Ref [205] explains the flux above the knee by the reacceleration of CR at the termination shock at galactic wind.

Second variation of this model category is that source accelerates CR above knee following a broken energy spectrum, such as in models [75, 173]. The breaks could be caused by the transition from the free expansion to Sedov-Taylor phase in SNR. Ref [173] included a strong field amplification suggested by Bell and Lucek [60, 59] into a toy acceleration model and obtain a steep-

ening of the injection spectrum at $R_{br} = 2$ PV by $\Delta\beta = 0.9$.

Last possibility was first suggested by Erlykin and Wolfendale [94, 93] where they proposed that the knee region is dominated by a single young nearby source, arguing that the sharpness of the knee requires the dominance of a single source. They suggested Vela, a SNR with age of 11 kyr and distance of 270 pc to this possible source. We will in the following sections present our work in modelling and studying the latter possibility.

Summary : In this chapter, we summarise the theoretical models explaining CRs journey from acceleration to detection, in a general point of view. We tried to highlight some deviations from the original paradigm.

Cosmic rays are charged energetic particles, discovered in 1785 by Coulomb. However, it had to wait more than a century to be considered as a radiation coming from outside the atmosphere. Development of detection technique, as the use of the extensive air shower and space mission, makes spectrum reconstruction possible.

The all-particles energy spectrum obtained from the combination of multiple experiments' data extends over 12 orders of magnitude in energy and 32 orders of magnitude in intensity. It follows a power law spectrum with spectral index ~ -2.7. Though, it contains number of features, such as, the "knees" where the spectrum steepens, the most remarkable appears at $E_k \sim 4-5\,\mathrm{PeV}$; the "ankle" where the spectrum flatten; and the high energy cut off, named the "GZK" cut off, due to CRs interaction with CMB.

Galactic CRs are believed to be accelerated in supernova remnants, since this source population released an energy amount compatible with the energy budget needed to accelerate CRs. However, other sources are currently studied such as Superbubles, novae, GRB, and the galactic center black hole. For a huge majority of possible sources, the acceleration mechanism taking place is the diffuse shock acceleration mechanism. This mechanism predict an accelerated particle intensity following a power law $I(E) \propto E^{-\alpha}$, where in the simplest approximation $\alpha = 2$. More realistic models predict softer slopes, and some predict other features in the accelerated spectrum such as breaks.

Before reaching our detectors, CRs propagate in the ISM, where the GMF

plays a major role. While the regular part describes the large scale trajectory of CRs, the turbulent part force CRs to follow a random walk, that can be described by an energy dependent diffusion coefficient. During their propagation, CRs, called "primaries", interact with ISM through nuclear interactions as "spallation" producing secondary particles, called "secondaries". The secondaries-to-primaries ratios are directly linked to the CRs diffusion coefficient. Experimental data of Boron-to-Carbon ratio gives a $D(R) \propto R^{-\delta}$ where $\delta = 1/3$ consistent with a Kolmogorov turbulence. The received CRs primaries is thus expected to be a combination of acceleration and propagation effect $I(E) \propto E^{-(\alpha+\delta)}$. More complex propagation models studies include non linear effects to explain the discrepancies observed between the perfect power law prediction and experimental data. It was also shown that, while the turbulent magnetic field succeed in isotropising CRs, an important regular part is needed to explain CR escape from the Galaxy. Thus, at high energies, CRs propagation is expected to be anisotropic.

Finally, we concentrate on the knee feature of the CRs spectrum. Possible origins of the knee falls into 3 categories : the first linked it with particle interaction effects, but was excluded by LHC; the second is due to a change in diffusion regime; and the third linked the knee with acceleration effect or source particularities. One of the models proposed in the latter category is the dominance of a single source at PeV energies producing the knee in the all-particles spectrum.

Chapter 3

Vela : Dominent source around cosmic rays knee

In this chapter we present our model of the contribution of the nearest young supernova remnant Vela to the local cosmic ray flux taking into account both the influence of the Local Bubble and the effect of anisotropic diffusion. The magnetic field at the bubble's wall prevents low-energy particles to penetrate into the bubble, leading to an energy-dependent suppression of CRs from Vela inside the bubble. The resulting CR flux at Earth in the energy region around the cosmic ray knee can naturally explain the observed fluxes of individual groups of nuclei and their total flux. Adding the CR flux from a 2–3 Myr old local CR source suggested earlier, the CR spectra in the whole energy range between 200 GeV and the transition to extragalactic CRs are described well by the combined fluxes from these two local Galactic sources.

In section 3.1 we studied all local sources and their distance to magnetic field line crossing the sun, in order to select to most probable dominant source in the nearby ISM. Then we described magnetic field structure close to solar system taking into account the effect of the local super bubble in

section 3.2. In section 3.3 we present our model for source injection spectrum and flux calculation. And we finally present our results in section 3.4, where we show the CRs fluxes inside the Local Bubble, corresponding to Earth received flux, at the end of this section we studied the dependence of our result on the different parameter of our model.

3.1 Motivation for the choice of the source

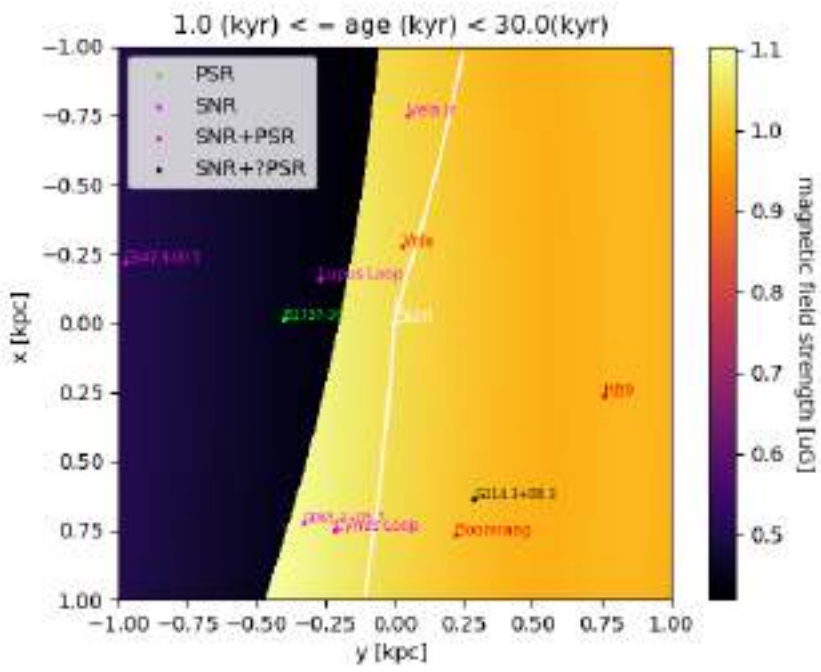

Figure 3.1: Location of potential CR sources with age between 1–30 kyr. The Galactic center is at $(x, y) = (0, -8.5\,\mathrm{kpc})$. The yellow line shows the magnetic field line passing through the Sun projected on the Galactic plane.

Cosmic rays propagate preferentially along the regular magnetic field lines. Therefore, the number of CR sources contributing to the locally observed CR flux is reduced relative to the case of isotropic diffusion [108]. In

particular, the contribution of a source to the local flux depends strongly on its perpendicular distance to the magnetic field line through the Sun. In Fig. 3.1, we show the position of potential CR sources which are younger than 30 kyr. As potential sources we distinguish pulsars (light green points), SNRs (magenta points), SNRs associated with pulsar (red points), and SNRs possibly associated with pulsars (black points). Additionally, we show the magnetic field line passing through the Sun in the JF model as a yellow line. We note that the kink of the field line near the position of the Sun is a projection effect, caused by the z component of the field. Only four sources are close to the magnetic field line through the Sun; these sources are in the position to give a dominating contribution to the local CR flux.

Source	Name	τ/kyr	d/kpc	d_B/kpc	$\Delta_\parallel$/kpc	$\Delta_\perp$/kpc
G065.3+05.7	–	20	0.8	0.27	**0.96**	**0.036**
G074.0-08.5	Cygnus Loop	15	0.78	0.3	**0.83**	**0.032**
G106.3+02.7	Boomrang	10	0.8	0.32	**0.68**	**0.026**
G114.3+00.3	–	7.7	0.7	0.36	**0.6**	**0.023**
G160.9+02.6	HB9	5.5	0.8	0.77	**0.5**	**0.019**
G263.9-03.3	Vela	11	0.29	0.06	**0.71**	**0.027**
G266.2-01.2	Vela Jr	3.8	0.75	0.18	**0.42**	**0.016**
G330.0+15.0	Lupus Loop	23	0.33	0.32	**1.03**	**0.039**
G347.3-00.5	–	1.6	1	0.8	**0.27**	**0.01**
B1737-30	–	20.6	0.4	0.4	**0.98**	**0.037**

Table 3.1: Properties of the sources in Fig. 3.1: d and d_B denote the distance to the Sun and to the magnetic field line passing through the Sun, respectively, while Δ_i is the typical distance CRs with energy $E = 3\,\mathrm{PeV}$ diffuse parallel and perpendicular to the magnetic field line. All distances are in kpc.

Table 3.1 summarises the available information[1] on the CR sources shown in Fig. 3.1. The last column shows the distance $d_i = \sqrt{2D_i\tau}$ beyond which the CR flux from a CR source with age τ is exponentially suppressed. Since

[1]Data on the pulsars are from `https://www.atnf.csiro.au/people/pulsar/psrcat/` and on SNRs from `http://snrcat.physics.umanitoba.ca/SNRtable.php`.

the local magnetic field line is approximately aligned with the x axis, we can set $\Delta_x \simeq \Delta_\parallel \simeq \sqrt{2D_\parallel \tau}$ and $\Delta_{y,z} \simeq \Delta_\perp \simeq \sqrt{2D_\perp \tau}$, with $D_\parallel$ and $D_\perp$ as the parallel and perpendicular diffusion coefficients, respectively. These diffusion coefficient were computed numerically for the position of Vela and the CR energy $E = 3\,\mathrm{PeV}$. The typical distance Δ_i CRs with such an energy diffuse during the time τ should be compared to the perpendicular distance d_B of the source to the magnetic field line passing through the Sun. Depending on the ratio of these two quantities, we can distinguish two cases:

- $\Delta_\perp \ll d_B$: The contribution of this source to the local CR flux is exponentially suppressed.
- $\Delta_\perp \gtrsim d_B$: The source contributes to the local CR flux.

From Table 3.1 it is clear that the contribution from Vela is the dominating one.

Repeating the same analysis for older sources is less conclusive. First, one usually does not observe the shell but only the pulsar for sources which are few Myr old. Since pulsar velocities are typically high, it is difficult to reconstruct the actual position of the supernova explosion. Therefore we assume here motivated by the observations of Fe-60 [145, 62, 100, 211], that only one or two additional CR sources with an age 2–3 Myr contribute to the local CR flux in the energy range from $\sim 10\,\mathrm{TeV}$ up to the knee.

3.1.1 Vela SNR

The Vela SNR is one of the closest supernova remnants to us as already discussed above. Different estimates of the distance to the Vela SNR suffer from a large uncertainty: from $250 \pm 30\,\mathrm{pc}$ [76] to $350\,\mathrm{pc}$[91]. Hubble Space telescope parallax observations of the Vela pulsar give the distance to the

pulsar of $D_{Vela} = 294^{+76}_{-50}$ pc [74], we chose here a mean value of $D_{Vela} \simeq 270$ pc .

The estimate of the Vela SNR age is also uncertain, it ranges from a few thousand years [196] to $t_{SNR} \simeq 2.9 \times 10^4$ yr [49]. The most commonly cited estimate is $t_{SNR} = t_{pulsar} \simeq 1.14 \times 10^4$ yr, where t_{pulsar} is the age of the Vela pulsar [189].

Figure 3.2 shows observation of Vela SNR in X-rays and γ-rays together with VelaJr and Puppis A. The total luminosity is estimated to $L_{Vela} \simeq 1.4 \times 10^{50}$ ergs in Ref.[200].

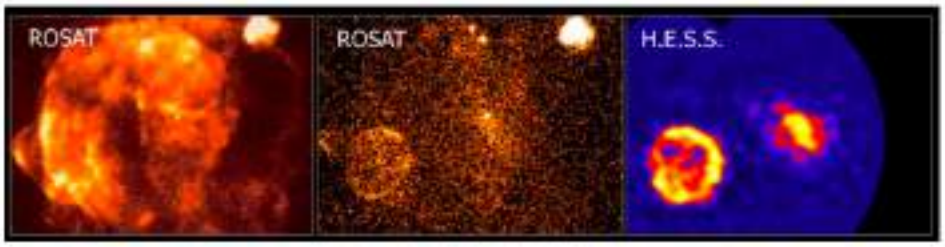

Figure 3.2: X-ray and TeV gamma-ray images of a region of the sky containing Vela (larger bubble, 5 degrees diameter), Vela Junior (smaller bubble on the left) and Puppis A (bubble on the right top) supernova remnants [49, 26, 15]. (image credit: `https://www.mpi-hd.mpg.de/hfm/HESS/pages/home/som/2006/05/`).

In the case of JF magnetic field and an injected luminosity of $L = 10^{50}$ ergs from Vela SNR, the flux received on Earth was calculated for three different dispositions, first face on and directly connected to sun with magnetic field line, secondly shifted by 12 pc from the magnetic field line, and third shifted by 25 pc from the magnetic field line. In all the cases the received flux was more than two orders of magnitude above the experimental data.

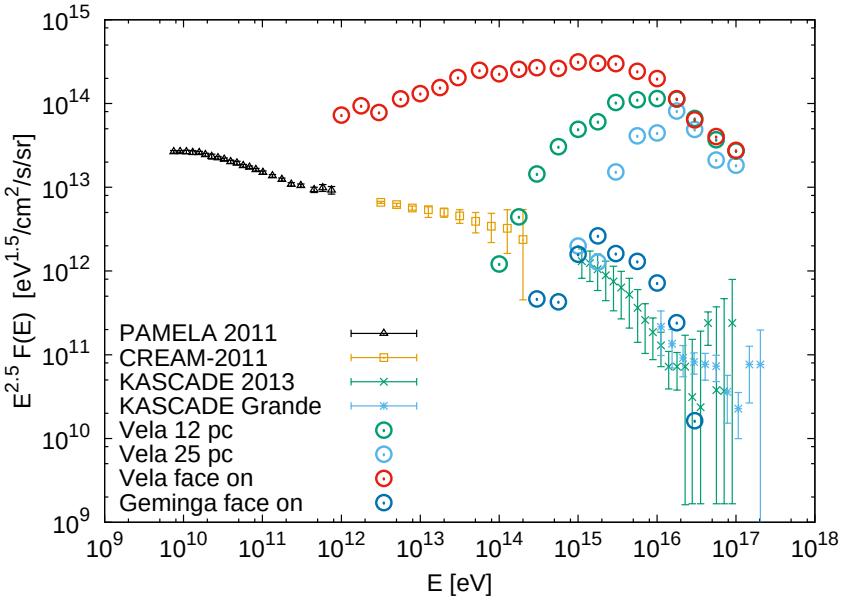

Figure 3.3: Cosmic rays flux from Vela SNR for different positions of the source, face on (red), shifted by 12 pc (green) and shifted by 25 pc (blue) from magnetic field line connected to the sun, together with measurement from PAMELA [20], CREAM [216] as well as from KASCADE and KASCADE-Grande [47].

3.2 Magnetic field model

Our model of magnetic field is based on two components, the magnetic field in the bubble and outside the bubble. Will describe the geometry and the parameters of each part.

3.2.1 Local Bubble

The Sun resides in a low-density region of the interstellar medium (ISM) called the Local Bubble (LB). The LB extends roughly 200 pc in the Galactic plane, and 600 pc perpendicular to it, with an inclination of about 20° [154].

Observations and simulations [70, 192] show that the bubble walls are fragmented and twisted. Moreover, outflows away from the Galactic plane may open up the bubble [70]. In view of this complicated geometry, we idealise the LB in our numerical simulation as follows [41]: We assume for the magnetic field profile $\vec{B}(\vec{x})$ parallel to the Galactic plane (x, y) a cylindrical symmetry, i.e. we imply that the changes as function of the Galactic height z are small compared on the considered length scales. Then $\vec{B}(\vec{x})$ is only a function of $r = \sqrt{x^2 + y^2}$. We use as a base radius R of the bubble $R = 100\,\mathrm{pc}$ and set the wall thickness to $w = 3\,\mathrm{pc}$. We assume inside the bubble and the wall a clockwise oriented magnetic field for $y > 0$ and an anticlockwise one for $y < 0$. The strength of the regular magnetic field depends only on the radius and is set to $B_{\mathrm{in}} = 0.1\mu G$ inside the bubble, $B_{\mathrm{sh}} = 12\mu G$ in the wall.

The transitions between different magnetic field regimes are interpolated by logistic functions $T(r)$. The width of the two transitions is parametrised by w_i with $i = \{1, 2\}$, while w denotes the extension of the wall. We will discuss the dependence of our results on the chosen value of these parameters in Sec. 3.5. As our default parameters, we use $w = 2\,\mathrm{pc}$, $w_1 = 1\,\mathrm{pc}$, and $w_2 = 0.1\,\mathrm{pc}$

$$T_1 = \left[1 + \exp\left(-\frac{r - R + w/2}{w_1}\right)\right]^{-1}, \tag{3.1}$$

$$T_2 = \left[1 + \exp\left(-\frac{r - R - w/2}{w_2}\right)\right]^{-1}, \tag{3.2}$$

where we identify the center of the LB with the origin of our coordinate

system. We set the x,y and z components of the magnetic field for $r < R$ to

$$B_{\rm x} = s\,[B_{\rm in}(1-T_1) + B_{\rm sh}T_1]\sin(\theta)\exp(-z^2/z_{\rm b}^2) + B_{\rm out,x}(1-\exp(-z^2/z_{\rm b}^2)), \tag{3.3}$$

$$B_{\rm y} = -s\,[B_{\rm in}(1-T_1) + B_{\rm sh}T_1]\cos(\theta)\exp(-z^2/z_{\rm b}^2) + B_{\rm out,y}(1-\exp(-z^2/z_{\rm b}^2)), \tag{3.4}$$

$$B_{\rm z} = B_{\rm out,z}. \tag{3.5}$$

Similarly, the field is given for $r > R$ by

$$B_{\rm x} = [sB_{\rm sh}(1-T_2)\sin(\theta) + B_{\rm out,x}T_2]\exp(-z^2/z_{\rm b}^2) + B_{\rm out,x}(1-\exp(-z^2/z_{\rm b}^2)), \tag{3.6}$$

$$B_{\rm y} = [-sB_{\rm sh}(1-T_2)\cos(\theta) + B_{\rm out,y}T_2]\exp(-z^2/z_{\rm b}^2) + B_{\rm out,y}(1-\exp(-z^2/z_{\rm b}^2)), \tag{3.7}$$

$$B_{\rm z} = B_{\rm out,z}, \tag{3.8}$$

With $s = y/|y|$ and $B_{\rm out}$ are the corresponding components of the field outside the bubble. The Sun is assumed to be at the centre of the LB, while Vela is situated at the distance 270 pc from the Sun at $y = 0$.

3.2.2 Magnetic field outside the bubble

We considered two cases for the magentic field outside the bubble, a uniform magentic field and the Janson-Farrar magentic field.

Uniform case : We assumed a uniform magnetic field profile $\vec{B_{\rm out}} = \vec{B_x}$ parallel to the galactic plane (x, y) and we approximated the strength at $B_{\rm out} = 1\mu G$ outside the bubble. Figure 3.4 describe the geometry of the system in the caseU. The strength of the magnetic field for $y = 0$

is plotted in figure 3.5 where the effect the bubble wall of the total amplitude of the magnetic field appears.

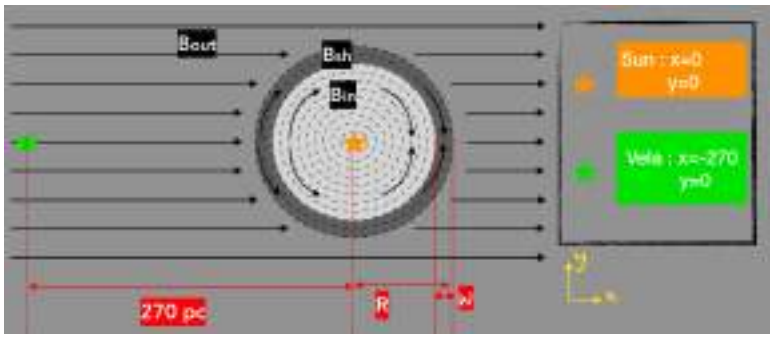

Figure 3.4: Scheme showing the geometry of the magnetic field in caseU. The magnetic field is parrallel to galactic plane $B_{tot} = \sqrt{B_x^2 + B_y^2}$, the sun is at $x = 0, y = 0$ and the GC at $x = 0, y = -8.5$. The colors are choosen arbitrary, the darker has highier magnetic field amplitude.

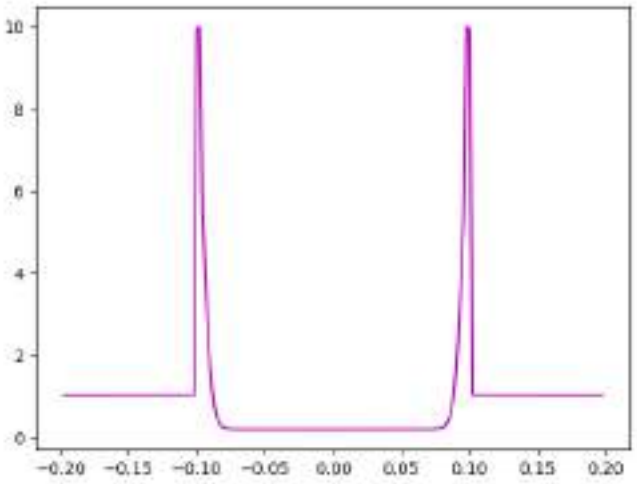

Figure 3.5: The total amplitude of the magnetic field $B_{tot} = \sqrt{B_x^2 + B_y^2}$ plotted as a function of x for $y = 0$ in the presence of the Locale Bubble that extends from $x = -100\,\mathrm{pc}$ to $x = 100\,\mathrm{pc}$ for $y = 0\,\mathrm{pc}$.

Janson-Farrar case : We employed a more realistic description of the magnetic field outside the bubble using the Jansson-Farrar (JF) model

for the Galactic magnetic field [127], everywhere outside the bubble $\vec{B_{\rm out}} = \vec{B_{\rm JF}}$. Figure 3.6 shows projection of the Janson-Farrar model used in our simulation, in the figure we show the general field without the Local Bubble, in the (x, y) plane the geometry would be equivalent to the one shows in the figure 3.4 but with $B_{out,y} \neq 0$ and $B_z \neq 0$.

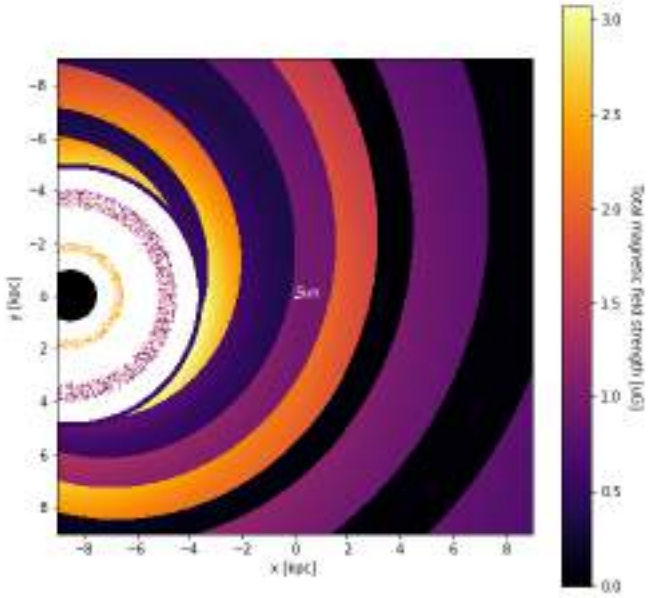

Figure 3.6: Projections B_{out} field in caseJF on galactic plane. The sun is at $(0, 0, 0)$ and the galactic center is at $(0, -8.5, 0)$. The composition of the galactic component appears with spiral arms together with the molecular ring.

3.2.3 Turbulent magnetic field

The turbulent magnetic field modes are distributed between $L_{\rm min} = 1\,{\rm AU}$ and $L_{\rm max} = 25\,{\rm pc}$ according to an isotropic Kolmogorov power spectrum. We construct the turbulent magnetic field using nested grids as described

in Ref. [113]. In the actual simulations, only field modes above $L'_{\rm min} = 0.01\,{\rm pc}$ were included. Inside the wall, we omit all Fourier modes with $L > L_{\rm max}/100$, such that the largest modes still have few oscillations within the thickness of the wall. To maintain the same strength $B_{\rm rms}$ of the turbulent field, we enhance the power in the modes with smaller wave-lengths. The strength of the turbulent field is set for $(R-w/2-3w_1) \leq r \leq (R+w/2+3w_2)$ to $B_{\rm turb} = B_{\rm reg}/2$, and for $r < (R-w/2-3w_1)$ to $B_{\rm turb} = 5B_{\rm in}$. Hence CR propagate outside the bubble anisotropically, but inside nearly isotropically. This choice is motivated by the notion that the supernova explosion which created the LB expelled the regular field into the wall. At the same time, the injected turbulence lead to an increase of the turbulent component of the magnetic field in the bubble.

3.3 Model of injection from the source

3.3.1 Injection of cosmic rays

We use as CR injection spectrum for Vela a broken power law in rigidity $\mathcal{R} = E/(Ze)$ with a break at $\mathcal{R}_{\rm br} = 2 \times 10^{15}\,{\rm V}$ and an exponential cut-off at $\mathcal{R}_{\rm max} = 8 \times 10^{15}\,{\rm V}$ for case U, and $\mathcal{R}_{\rm br} = 3 \times 10^{15}\,{\rm V}$ and $\mathcal{R}_{\rm max} = 8 \times 10^{15}\,{\rm V}$ for case JF, respectively,

$$\frac{dN}{d\mathcal{R}} \propto \begin{cases} \mathcal{R}^{-2.2}, & \text{if} \quad \mathcal{R} < \mathcal{R}_{\rm br} \\ \mathcal{R}^{-3.1}\exp(-\mathcal{R}/\mathcal{R}_{\rm max})), & \text{if} \quad \mathcal{R} \geq \mathcal{R}_{\rm br}. \end{cases} \tag{3.9}$$

The steepening of the injection spectrum by $\Delta\beta = 0.9$ is motivated, e.g., by the analysis of Ref. [173]: Including strong field amplification as suggested by Bell and Lucek [60, 59] into a toy acceleration model, these authors found a break in the energy spectrum of accelerated protons. For typical values of the

SNR parameters, this break is located close to the knee region. The strength $\Delta\beta$ of this steepening depends among others on the injection history, and in a test particle ansatz $\Delta\beta = 0.9$ was found.

The numerical values of the break and the cut-off as well as the relative normalisation of the different groups of nuclear elements were chosen such to reproduce best the measured CR composition.

3.3.2 Cosmic rays flux calculation

In order to compute the flux, we injected 30.000 protons per energy at the position of Vela and propagated them for 12.000 yr. We calculated the CR density $n(E)$ in the three regions of interest averaging the CR densities between 8 to 12 kyr: around the source, in the bubble wall, and inside the bubble. The CR flux $F(E) = c/(4\pi)n(E)$ was then computed from the CR densities in the considered volumes. For energies below 100 TeV we deduced the flux inside the bubble from the flux calculated at earlier times and higher energies using the scaling relation

$$(E_{\text{low}}/E_{\text{high}})^{1/3} \approx t_{\text{early}}/t_{\text{now}}. \tag{3.10}$$

This relation was confirmed in the numerical simulations presented in the supplementary material of Ref. [134].

We defined the flux around the source considering the y-z plan centred on the source with a thickness of $\Delta x = 5$ pc and $\Delta y = 100$ pc, and $\Delta z = 100$ pc form -50 pc to +50 pc on each side. For the flux inside the bubble wall, we considered a ring of 1 pc thickness at the shell, and computed the flux from $z = -50$ pc to $z = 50$ pc. Finally, we computed the flux at the position of the Earth from the CR density inside a cube of 100 pc side length centred at

the Sun.

3.4 Resulting CRs flux from Vela

3.4.1 Spectrum of cosmic rays

In Fig. 3.7, we show the normalised proton flux in the bubble wall, inside the bubble and around the source, for the cases U (top panel) and JF (bottom panel). Our results are compared at low energies to the data of direct cosmic ray measurements, NUCLEON [117] and and CREAM–3 [216], while we show at higher energies indirect measurements from KASCADE and KASCADE-Grande [47]. At high energies, $E \gtrsim 10^{16}\,\mathrm{eV}$, the bubble wall is transparent, since the Larmor radius ($R_L \sim 100\,\mathrm{pc}$) of such protons is large compared to the thickness of the bubble wall. For energies below 1 PeV, particles start to be trapped in the wall and the flux inside the bubble is increasingly suppressed. While the general behaviour in both cases is similar, the proton flux at Earth is higher in the case JF. This difference can be explained by the larger transition width w_1 we use in case JF, $w_1 = 1\,\mathrm{pc}$, compared to $w_1 = 0.1\,\mathrm{pc}$ in case U.

In Fig. 3.8a, we show the proton flux received at Earth from Vela in caseU together with the proton flux from a 2–3 Myr old SN in the model of Refs. [134, 135]. The combined flux of these two sources covers the energy range from 200 GeV up to the extragalactic transition region, fitting well the experimental data. Additionally, we show the extragalactic proton flux which we obtained from a fit to the AUGER data as

$$E^{2.5}F(E) = 5.10^{10}\left(\frac{E}{10^{16}\mathrm{eV}}\right)^{0.3}\exp\left(\frac{-E}{1.5\times10^{18}\mathrm{eV}}\right)\frac{\mathrm{GeV}^{1.5}}{\mathrm{m}^2\,\mathrm{s}\,\mathrm{sr}}.$$

We also compute the flux for other nuclei in caseU : the flux of helium is

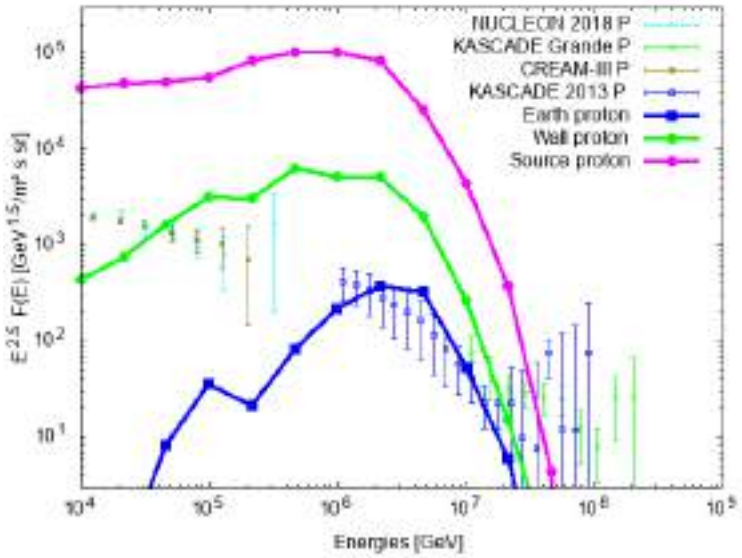

(a) caseU

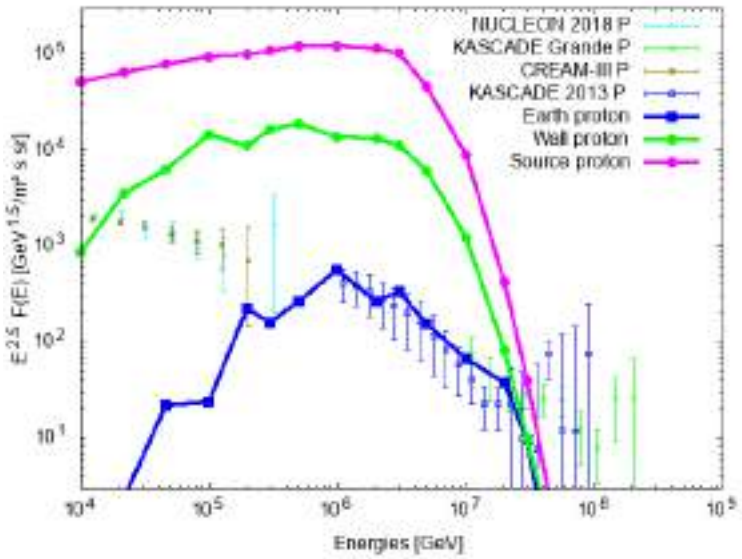

(b) caseJF

Figure 3.7: Contribution of Vela to the proton flux on Earth. The proton fluxes at the source, in the wall of the Local Bubble wall and near the Earth are shown with magenta, green and blue lines, and compared to experimental data from NUCLEON [117], CREAM–3 [216] as well as from KASCADE and KASCADE-Grande [47].

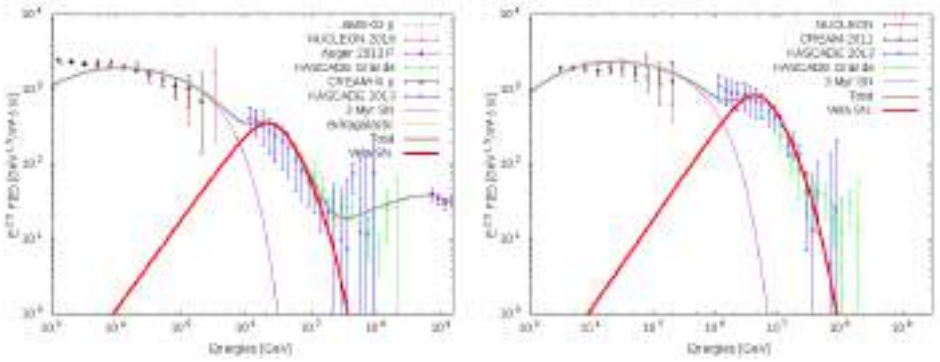

(a) Proton (b) Helium

Figure 3.8: Proton (left) and Helium (right) flux as function of energy from experiments NUCLEON [117], CREAM [217], KASCADE and KASCADE-Grande [47] and AUGER [61]. Vela flux shown with red line, flux from 2–3 Myr SN with violet line, extragalactic proton flux with orange line and total flux with black line.

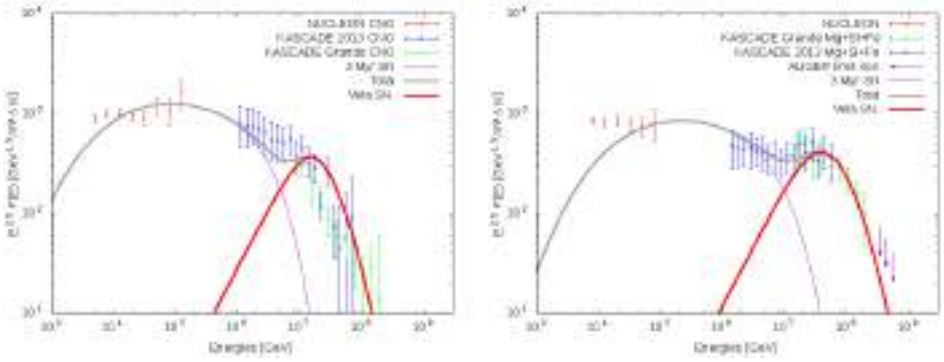

(a) CNO (b) Fe+Si+Mg

Figure 3.9: Flux for the CNO nuclei (left) and the Mg-Si-Fe group (right) from Vela and the 2–3 Myr SN as a function of energy; in the violet the Auger limit on the iron flux. Both with same experimental data as in Fig. 3.8.

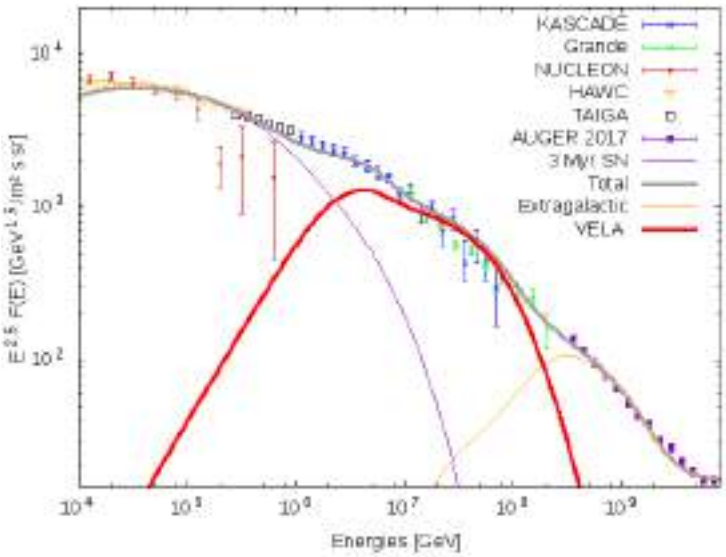

(a) All particles

Figure 3.10: The all-particles flux from Vela and from the 2–3 Myr SN and the extragalactic contribution from Ref. [131] together with experimental data from NUCLEON [117], HAWC [33], TAIGA [65], CREAM [217], KASCADE and KASCADE Grande [47], and AUGER [98].

shown in Fig. 3.8b, of the CNO group in Fig. 3.9a and of the SiMgFe group in Fig. 3.9b, respectively.

From Fig. 3.10, we see that the all-particles flux fits well the experimental data up to 10^{17} eV. In the energy range above 10^{17} eV, the extragalactic contribution becomes important which we model following Ref. [131]. We compute the total energy output of Vela and the relative contribution of the different nuclear groups from the normalisation of the simulated data to the experimental ones. In the case JF, the relative energy fraction in protons found is 0.54, the one of helium 0.42, of CNO 0.03 and of FeSiMg 0.007, respectively. We obtain then as total energy output in CRs 4.2×10^{49} erg. In the case U, the relative energy fraction in protons found is 0.55, the one of helium 0.42, of CNO 0.025 and of FeSiMg 0.004, respectively, and the total energy output in CRs 3.6×10^{49} erg. The total kinetic energy of the Vela supernova calculated in Ref. [200] is 1.4×10^{50} erg. We note also that the CR acceleration efficiency of Vela should be high, as it is expected in the scenario of strong magnetic field amplification of Refs. [60, 59].

3.5 Parameter dependence of the fluxes

The main parameters of our model for the magnetic field in the LB are the magnetic field strength $B_{\rm sh}$ in the wall, the wall extension w and the widths $w_{1/2}$ of the transition regions between the magnetic field in the wall and the outside. By varying these parameters, we study how the flux in the wall and inside the LB changes to study the systematics incertainty of our results.

To do so, we run a set of simulations modifying each time only one parameter. To make these simulations less computing time expansive, we consider a miniature model with a smaller bubble, $R = 50\,\mathrm{pc}$, and a reduced distance to the source, $d = 100\,\mathrm{pc}$. Outside the bubble, we use instead of the

JF model a uniform magnetic field directed along the x axis with strength $B_{\text{out}} = 3\mu\text{G}$. Moreover, we compute the CR flux at an earlier time, $T = 7\,\text{kyr}$. Therefore, the fluxes obtained should not be compared to experimental data, but serve to illustrate how the flux in the wall and inside the bubble depends on the various parameters. If not otherwise specified, we choose the widths as $w = 3\,\text{pc}$, $w_1 = 0.1\,\text{pc}$ and $w_2 = 0.01\,\text{pc}$, while we set the magnetic field strength in the wall to $B_{\text{sh}} = 10\mu\text{G}$.

3.5.1 Wall thickness

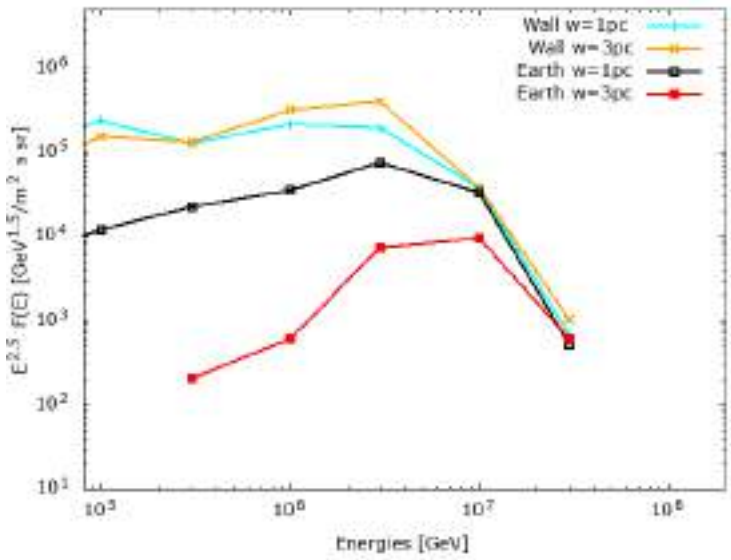

Figure 3.11: The proton flux computed for two different values of the wall thickness: $w = 1\,\text{pc}$, cyan line in the wall, and black line inside the bubble, and $w = 3\,\text{pc}$, orange line in the wall, and red line inside the bubble.

Figure 3.11 shows the flux inside the bubble and in the wall for two different values of the wall thickness, $w = 1\,\text{pc}$ and $w = 3\,\text{pc}$, respectively. While the flux of protons in the wall is practically independent from the wall thickness w, the fraction of protons traversing the wall and thus entering the bubble depends strongly on it. In contrast, the flux in the wall practically

does not change varying w, since only a small fraction of protons quits the wall and enters the bubble.

3.5.2 Wall magnetic field amplitude

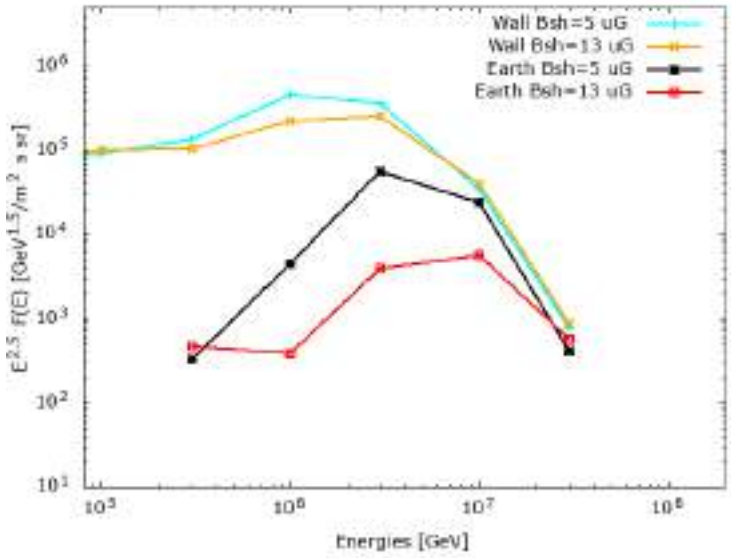

Figure 3.12: The proton flux computed for two different wall magnetic field $B_{\rm sh} = 5\,\mu G$, cyan line in the wall, and black line inside the bubble, and $B_{\rm sh} = 13\,\mu G$, orange line in the wall, and red line inside the bubble.

A similar behavior is found for the dependence of the fluxes on the amplitude of the magnetic field in the wall: A stronger magnetic field in the wall leads to a smaller fraction of protons entering the bubble, as they diffuse slower inside the wall. This behavior is shown in Fig. 3.12, where we plot the fluxes for two field strengths, $B_{\rm sh} = 5\,\mu$G and $B_{\rm sh} = 13\,\mu$G, in the shell. The flux inside the bubble is determined by the fraction of particles exiting the wall. It is a function of the wall thickness, the amplitude of the magnetic field in the wall, and the energy of the particle. For a given strength of the magnetic field one should compare the Larmor radius R_L of the particle and the wall thickness: For $R_L \gg w$, particles cross the wall easily without

scattering, while for $R_L \ll w$ (and short enough propagation times) they are trapped in the wall.

3.5.3 Transition widths

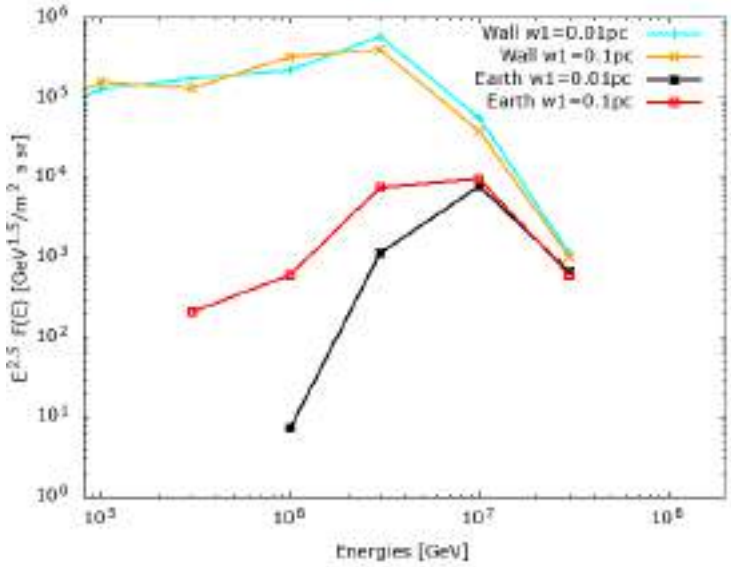

Figure 3.13: The proton flux computed for two different transition widths: $w_1 = 0.01\,\mathrm{pc}$, cyan line in the wall, and black line inside the bubble, and $w_1 = 0.1\,\mathrm{pc}$ orange line in the wall, and red line inside the bubble. Both cases with $w_2 = 0.01\,\mathrm{pc}$.

We have seen that the CR flux in the wall depends neither on the field strength nor the extension of the wall. In contrast, the width w_2 of the transition region between the outside and the wall influences the CR flux in the wall: When the transition is wider, the variation of the magnetic field strength is smaller and less protons are reflected. In the Fig. 3.14, one can see that the flux in the wall increases by a factor three for a transition width w_2 ten times larger. This implies also a higher flux inside the bubble. The same phenomena happen varying the second width w_1 between the bubble wall and the inside, as shown in Fig. 3.13: Increasing w_1 increases the flux

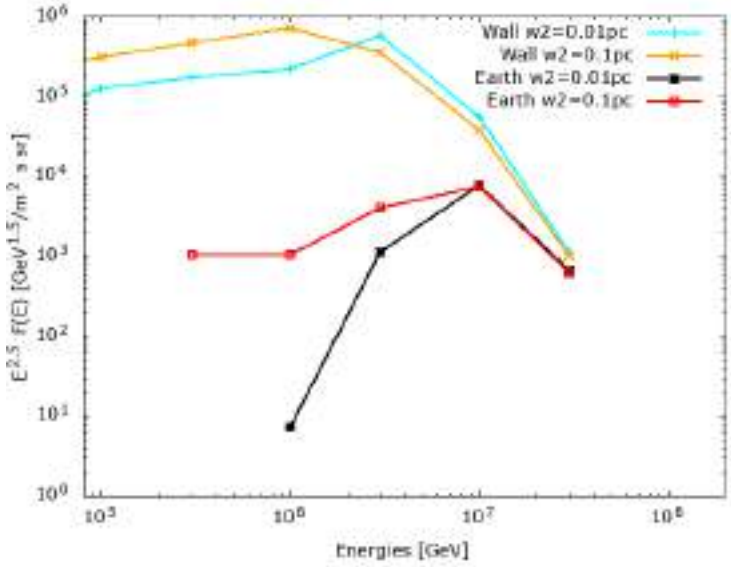

Figure 3.14: The proton flux computed for two different transition width $w_2 = 0.01\,\mathrm{pc}$, cyan line in the wall, and black line inside the bubble, and $w_2 = 0.1\,\mathrm{pc}$ orange line in the wall, and red line inside the bubble. Both cases with $w_1 = 0.01\,\mathrm{pc}$.

inside the bubble, because less particles are reflected.

Summary : In an anisotropic diffusion picture few sources are expected to participate to CRs flux received locally. The dominating sources should be connected to us by magnetic field lines and young enough, otherwise PeV CRs would have already escaped the system.

We studied the Vela supernova remnant contribution to local CRs flux, assuming two different magnetic field models. First a simplified uniform model connecting directly the source to sun, then a more realistic model, described in chapter 1, the Janson-Farrar model. We adjusted this magnetic field locally by adding the effect of the Local Bubble which distort the magnetic field lines, and we obtained a good description of the flux of individual groups on nuclei in the knee region.

To understand the uncertainty connected to the strength and the geometry of the Local Bubble, we vary the different parameters of our model and studied the dependence of the resulting flux on each parameter and we conclude that the amplitude and the shape of the received flux depends strongly on the size and the magnetic field strength on the walls of the bubble.

Part II

Astrophysical Neutrinos and Gamma rays

Chapter 4

Inter-Stellar Medium

ISM, CRs and GMF are 3 main ingredients of our Galaxy, they are coupled and together create an equilibrium. Indeed the three components have comparable pressure and interact with each other through electromagnetic forces. While GMF and CRs affect the dynamics of ISM and offer an efficient support against gravitational force, the weight of ISM confines magnetic field, hence CRs in the Galaxy, and it is also responsible for the random part of GMF due to its turbulent motion [99]. We already discussed the importance of GMF in CRs study, we will in this chapter talk about the interstellar medium.

This chapter will be divided into 3 sections. The first section 4.1 will introduce briefly all the components of the ISM, describing their properties. In section 4.2, we will focus on dust, we will explain how to convert extinction due to the presence of dust into hydrogen column density. The final section 4.3 is dedicated to introducing the dust map that we used in our work.

4.1 Composition of ISM

"The interstellar medium is anything not in the stars" as said Osterbrock [176]. It is the total matter and radiation content existing outside the star systems. Even if it contributes to a small fraction of the total mass of the Galaxy, it plays a major role in the galactic ecosystem. It consists of gas composed of atoms, molecules, ions and electrons; plus dust. Gas and dust manifest through absoption and emmission of electromagnetic continuum or lines, but also through obscuration, reddening and polarization of starlight. The interstellar matter represents $\sim 10-15\%$ of the total mass of the galactic disk. It is principally concentrated near the galactic plane and in the galactic arms. ISM mass is inhomogeneously distributed, approximatively 50% of the ISM mass is concentrated in clouds that occupies $\sim 1-2\%$ of the total ISM volume. The chemical composition of the ISM is close to abundance measurements on the sun, it is composed by 90.8% (70.4% in mass) of hydrogen, 9.1% (28.1% in mass) of helium and 0.12% (1.5% in mass) of heavier elements, usually referrd to as "metals".
This section is mainly based on Ferrière review [99].
The ISM can be divided according to to temperature and density into

Dark clouds : are made of very cold molecular gas with T$\sim 10-20\,$K and densities around $\sim 10^2-10^6\,\mathrm{cm}^{-3}$. Molecular clouds are usually probed from radio emission due to $J=1\rightarrow 0$ rotational transition of CO molecules.

Diffuse clouds : are composed by atomic gas at T$\sim 50-100\,$K and densities of $\sim 20-50\,\mathrm{cm}^{-3}$. They are mainly composed by hydrogen atoms and are usually observed by UV of the L_α lines.

Warm neutral (atomic) medium : is composed by hydrogen atoms de-

noted H_{I} at T$\sim 6000-10000\,$K and densities of $\sim 0.2-0.5\,\text{cm}^{-3}$. It is observed through the 21-cm line emitted in the "spin-flip" transition in the hydrogen atoms.

Warm ionized medium consist on region filled with hydrogen ions called "H_{II} regions" with T$\sim 8000\,$K and densities of $\sim 0.2-0.5\,\text{cm}^{-3}$. Hydrogen atoms are ionized by the strong UV radiation emitted by nearby O and B stars. It is widely observed using H_α lines, the optical hydrogen Balmer lines produced by electronic transition from an excited state n>2 to the first excited state n=2.

Hot ionized medium : correspond to coronal gas where metals are also highly ionized, it has temperature T$\sim 10^6-10^7\,$K and densities $\sim 10^{-4}-10^{-2}\,\text{cm}^{-3}$. It is observed through X-rays emission and absorption of highly ionized atoms such as O_{VI} and N_{V}.

4.2 Dust

Dust represents 1% of ISM mass. It consist on microscopic particles composed of dielectric and refractory material with size of $\sim 0.01-0.5\,\mu$m. It is observed by two basic ways : Interaction with starlight (extinction and reddening, Diffusion and reflection, polarization, absorption lines by silicates); and emissions (thermal from NIR to FIR, IR emission bands of polycyclic aromatic hydrocarbons PAHs, radio continuum emission from rotating grains) [69]. Extinction is a wavelength dependant quantity, but before presenting the extinction curve, we will introduce extinction. A star emitting at wavelength λ with a magnitude m_λ would be observed with a magnitude

$m_{0,\lambda}$ in the absence of dust, see figure 4.1, with

$$m_{0,\lambda} = m_\lambda + 5\log(\frac{d}{10\,\mathrm{pc}}) \tag{4.1}$$

Where d is the distance of the star from the observer. In the case where

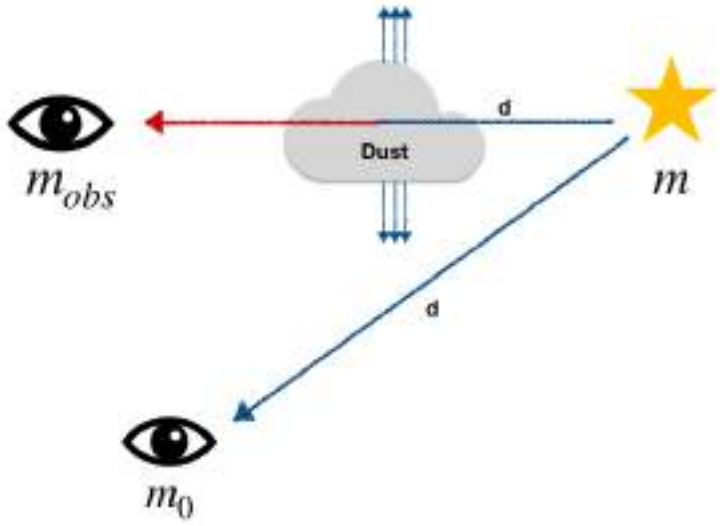

Figure 4.1: Cartoon drawing illustrating the extinction of starlight due to the presence of dust and the corresponding magnitudes.

starlight cross dust the observed magnitude $m_{obs,\lambda}$ becomes

$$m_{obs,\lambda} = m_{0,\lambda} + A_\lambda \tag{4.2}$$

Where A_λ is the extinction du to dust.

We can express A_λ from equation 4.2

$$A_\lambda = m_{obs,\lambda} - m_{0,\lambda} = -2.5\log(\frac{I_{obs,\lambda}}{I_{0,\lambda}}) \tag{4.3}$$

If we introduce the extinction depth due to extinction τ_{ext} such as $I_{obs,\lambda} = I_{0,\lambda} \exp^{-\tau_{ext}(\lambda)}$, then

$$A_\lambda = \tau_{ext}(\lambda) \frac{2.5}{\ln(10)} \tag{4.4}$$

We can define the total-to-selective extinction ratio $R_V = A_V/E(B-V)$, where $E(\lambda_1 - \lambda_2) = A_{\lambda 1} - A_{\lambda 2}$,and B and V are the B band (440 nm) and V band (550nm).

We can show that

$$\frac{A_\lambda}{A_V} = \frac{1}{R_V} \frac{E(\lambda - V)}{E(B-V)} + 1 \tag{4.5}$$

The value of R_V depends on the composition of the dust, for ISM $R_V = 3.1$ and for dense molecular clouds $R_V = 4 - 6$ Figure 4.2 shows extinction curves for different R_V values. We can notice 3 main regions : near UV where the curve is linear to λ^{-1} caused by grain size $< \lambda \sim 0.1\,\mu$m; 2175 Å equivalent to $\lambda^{-1} \sim 4.6\,\mu\text{m}^{-1}$ bump usually attributed to graphite particles; and Far UV $\gtrsim 6\,\mu\text{m}^{-1}$ where the curve grow exponentially and where extinction due to grain size $\ll \lambda \sim 0.01$ are expected to take place [69].

4.3 3D dust maps

Gaia DR2 data release of photometric and parallax measurements [103, 104] combined with 2MASS data allows the emergence of detailed 3D dust maps. As example of dust maps we cite Chen et al. [77] that used Gaia, 2MASS and WISE data to derive extinction profiles along the plane, Lallement et al [153] that used Gaia and 2MASS to propose a 3D map of galactic interstellar dust within 3 kpc and Leike et al. [157] that used Gaia, 2MASS,PANSTARRS, and ALLWISE surveys to build 3D dust map up to 370 pc to model the local ISM.

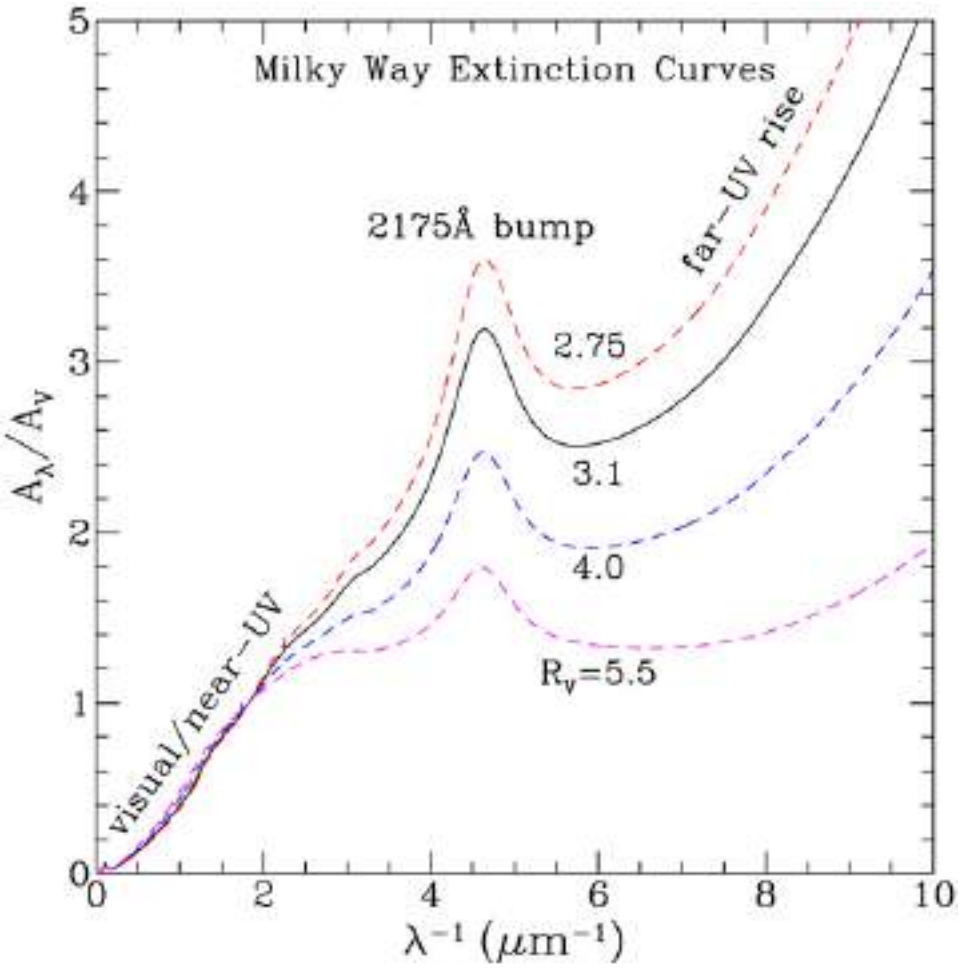

Figure 4.2: Plot of extinction A_λ/A_V as a function of $1/\lambda$, where the V band corresponds to $\lambda_V = 550\,\text{nm}$ for different value of R_V.

We studied both Lallement et al. and Leike et al. maps, and we chose to use the latter since it offers a better resolution of $1\,\text{pc}^3$ against $5^3\,\text{pc}^3$ for Lallement et al. Figure 4.3 shows the differences between the line of sight projection of dust maps up to 370 pc in galactic coordinates for Lallement et al. and Leike et al. We clearly notice the limits of Lallement et al to reconstruct detailed dust distribution features observed in Leike et al. Note that the authors used different reconstruction methods, while Lallement et al. used an iterative hierarchical technique, Leike et al. used a probabilistic

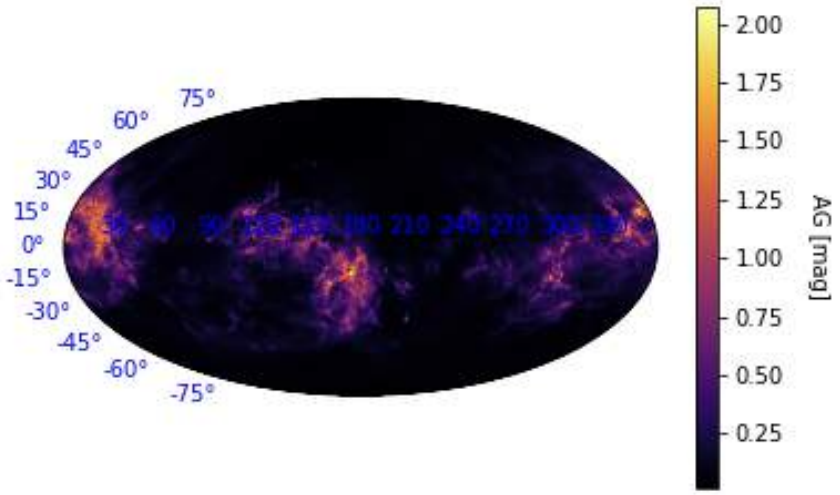

(a) LGE2020

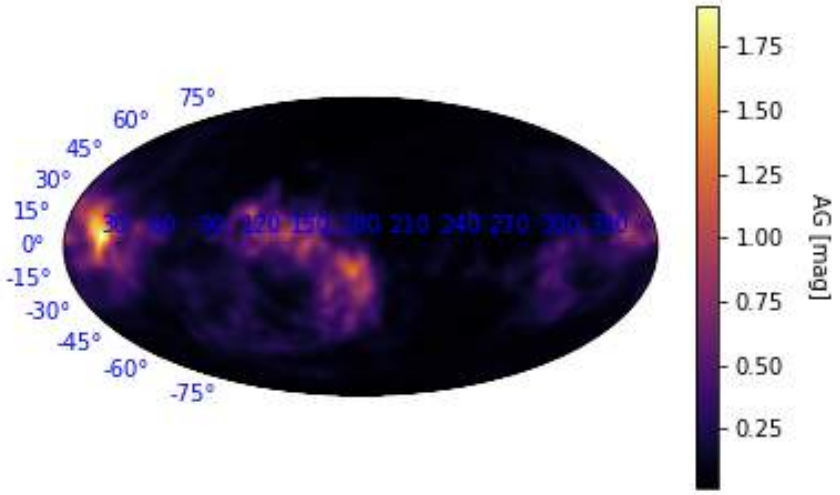

(b) Lal2019

Figure 4.3: *up :* LGE2020 [157] and *down :* Lal2019 [153] dust maps integrated over LOS for $r \in [0, 370]$ pc and projected in galactic coordinates, the GC is to the left.

approach derived from information field theory. In the following we will refer to Leike et al. maps as LGE2020 and to Lallement et al. map as Lal2019.

The LGE2020 dust map consists on a $740^2 \times 540\,\mathrm{pc}^3$ cube with a superior resolution of 1 pc. They deduced the G band extinction of five million stars with known parallaxes. Their results for the 3D distribution of dust are publicly available on `https://wwwmpa.mpa-garching.mpg.de/~ensslin/research/data/dust.html` as a grid containing the e-folds of extinction per cell, which correspond to the extinction depth in the G band $\tau_{ext}(G)$

The extinction due to dust is proportional to the hydrogen column density along the grid cell as [102]

$$N_{\mathrm{H}} = 2.87 \times 10^{21}\,\mathrm{cm}^{-2}\; A_{\mathrm{V}}/\mathrm{mag}. \tag{4.6}$$

Using moreover $A_{\mathrm{G}}/A_{\mathrm{V}} = 0.789$ as the selective extinction in the GAIA G band from Ref. [213], we obtain

$$N_{\mathrm{H}} = 3.63 \times 10^{21}\,\mathrm{cm}^{-2}\; A_{\mathrm{G}}/\mathrm{mag}. \tag{4.7}$$

In addition, we account for helium, which contributes 9.1% to the number density of the ISM. Figure 4.4 shows the projection of the integrated density of the LGE2020 dust grid on the x,y and z coordinates. Where the XY plane corresponds to the galactic plane. Positive x point toward $l = 0°$ and positive y toward $l = 90°$. z axis is perpendicular to the galactic plane with

positive z toward the Galactic North Pole.

$$x = r\cos(b)\cos(l) \tag{4.8}$$

$$y = r\cos(b)\sin(l) \tag{4.9}$$

$$z = r\sin(b) \tag{4.10}$$

In order to check the completeness of this map, we first compare the distribution of the LGE2020 and Lal2019 dust maps. We computed the average density on XY, XZ and YZ planes as a function of z, y and x respectively, multiplying by a factor 1.4 to account for helium and heavier elements,. We plotted the resulting functions for both Lal2019 and LGE2020 in figure 4.5.

We first notice that the two maps seems consistent in term of mass distribution even if we note some discrepancies as for $x \in [-300, -200]$ pc where LGE describes two discrete region while in Lal2019 it appears as a continuous dense region , and in $x \in [200, 300]$ pc and $y \in [150, 250]$ pc dust suppression is present in LGE2020 that doesn't appear in Lal2019.

In general, it is clear that LGE2020 overall amplitude is everywhere $\sim 25 - 30\%$ smaller then Lal2019 amplitude. We calculated the resulting average surface density Σ summing over the z coordinate, we obtain $\Sigma = 10.4\, M_\odot/\mathrm{pc}^2$ for LGE2020 and $\Sigma = 14.6\, M_\odot/\mathrm{pc}^2$ for Lal2019. The comparison with the estimate $\Sigma = 13 M_\odot/\mathrm{pc}^2$ for the local surface density from Ref. [101] indicates that the LGE2020 map includes $\simeq 80\%$ of the total gas.

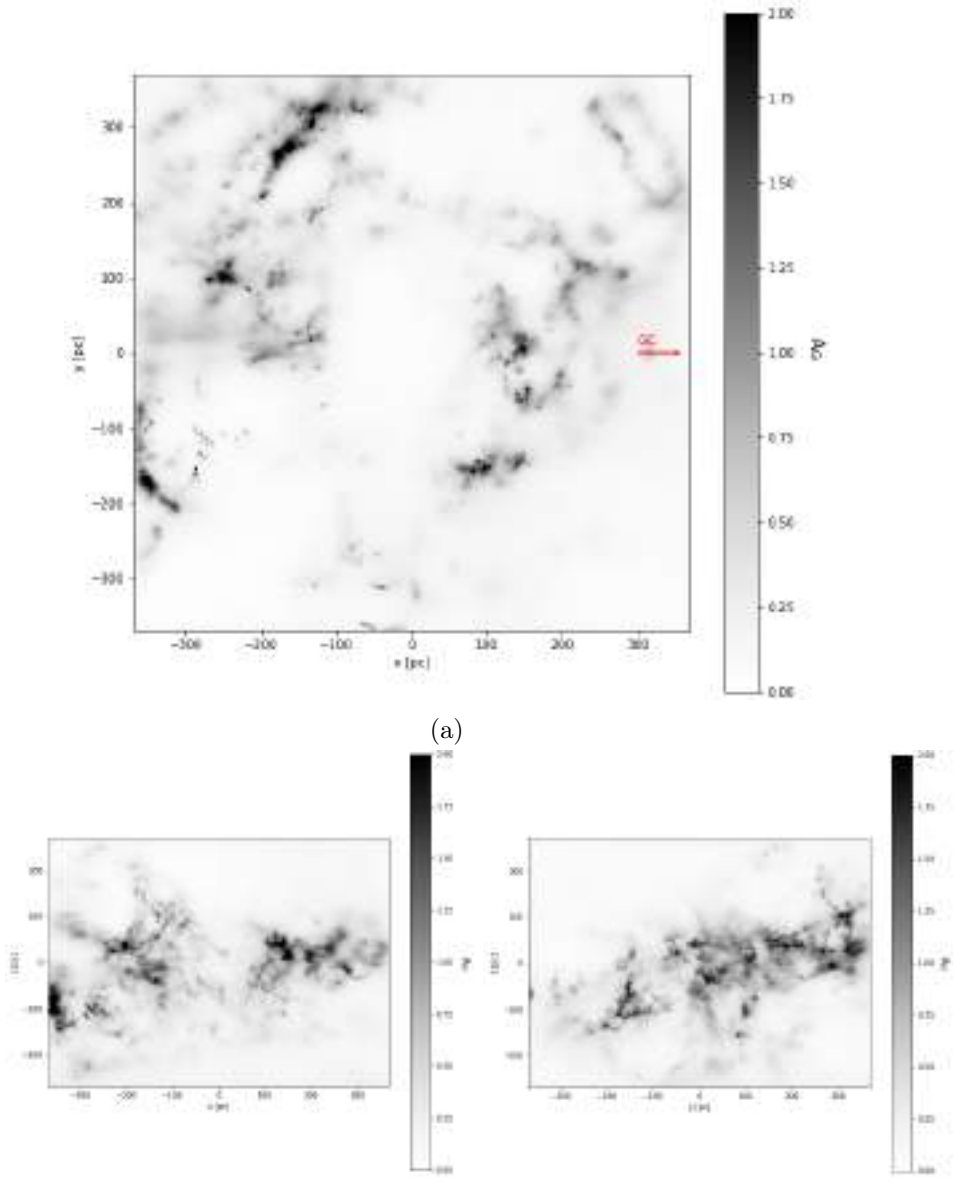

Figure 4.4: LGE2020 [157] dust grid integrated and projected in *(a)* XY plane, *(b)* XZ plane, *(c)* YZ plane. GC center is at y=0 and x=8.5 kpc.

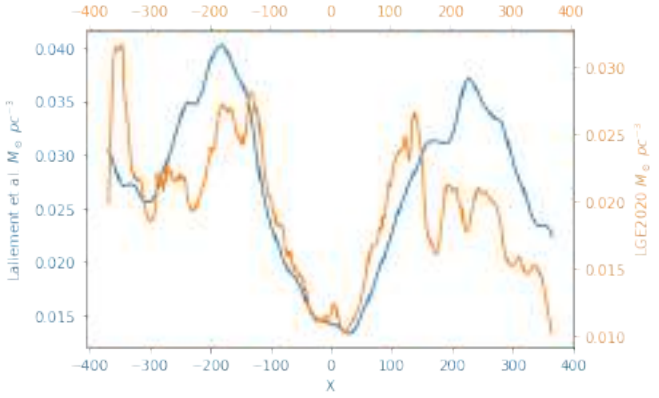

(a)

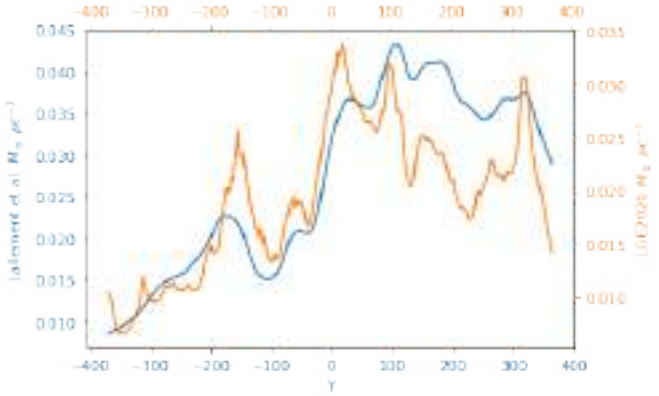

(b)

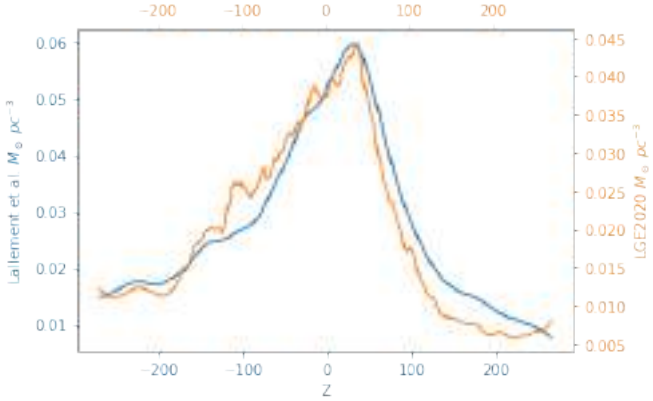

(c)

Figure 4.5: LGE2020 [157] in *(orange)* and Lallement et al. [153] in *(blue)* surface average density distribution, *(a) :* averaged over the YZ plane as a function of x, *(b) :* averaged over the XZ plane as a function of y and *(c) :* averaged over the XY plane as a function of z.

Molecular clouds

Another way to check the distribution of gas in the dust map is to reconstruct the closet knows molecular clouds. We isolated 5 clouds from LGE2020 dust map that we compare two maps produced by Lombardi et al. [162, 159, 160] in K band from 2MASS survey using the NICER method [161]. We plotted galactic projection dust map integrated over $r \in [0; 370]$ pc with a resolution of $dl = db = 0.1°$. We show in figure 4.6 Taurus and Perseus molecular clouds, in figure 4.7 Ophiuchus and Lupus molecular clouds, and in figure 4.8 Pipe nebulae.

From Ref. [213] we expect $A_G/A_K \sim 10$, we see for instance in the figure 4.6 that a priori LGE2020 are underestimating the dust extinction by at least a factor of $\sim 3 - 4$. This could be explained by three effects. First, a systematic diminution of extinction values is due to likelihood calibration, where to correct for positive expectation values in dustless regions, the authors subtracted that value from the all map leading to a general decrease of the extinction values. Second, the authors recommend distrusting scales bellow $\lesssim 2\,\mathrm{pc}$, hence they don't resolve the smallest clumps that might carry high matter density. Finally, the higher is the density the bigger will be the absoption, thus the harder it get to still find a viable source behind it, in the absence of data in those regions they interpolated density from close neighborhood.

As discussed above, LGE2020 map fail to reconstitute the densest clumps, it is thus interesting to compare the mass fraction occupied by the darkest region in both maps, we reconstructed in figure 4.9 the cumulative mass fraction for Pipe nebula, Ophiuchus and Lupus clouds, and we clearly see that the plot quickly drop above $A_G \gtrsim 1.75$ for Ophiuchus in LGE2020

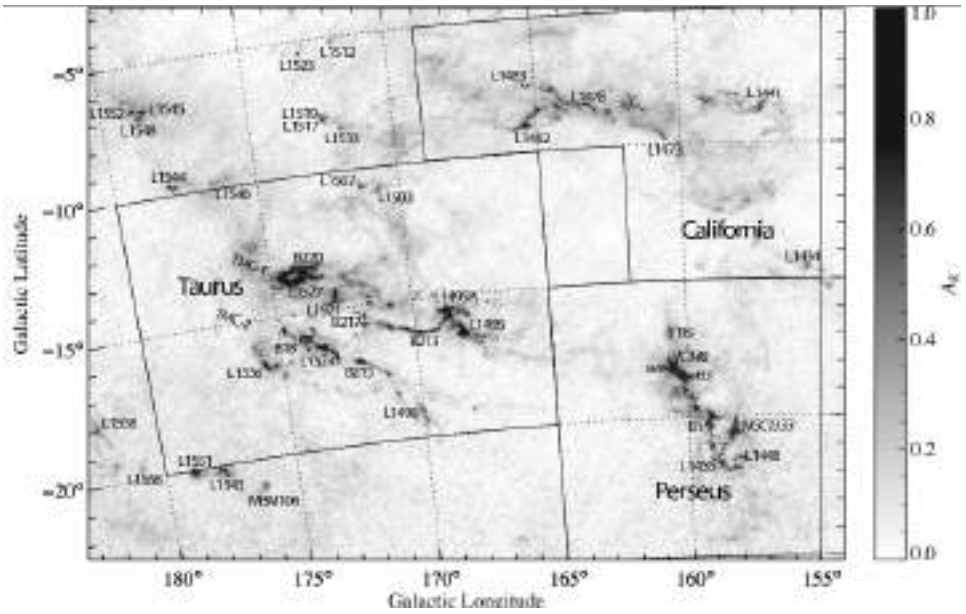

(a) Taurus and Perseus MC from Lombardi et al. [160]

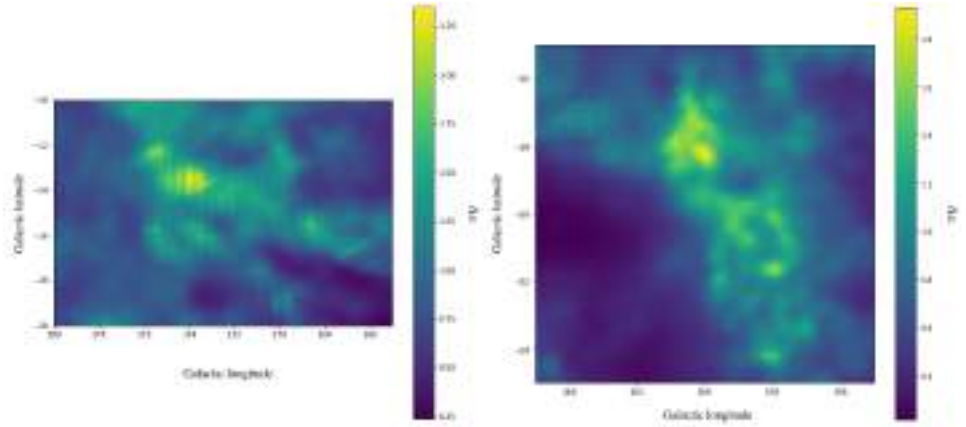

(b) Taurus MC

(c) Perseus MC

Figure 4.6: Projection of *(a)* Taurus and *(b)* Perseus molecular clouds from LGE2020 [157] in G band and *(c)* represent both Taurus and Perseus in K bands from [160].

extinction map while in Lombardi et al. it reaches extinction up to $A_K \simeq 2.5$ when we expect $A_G/A_K \sim 10$.

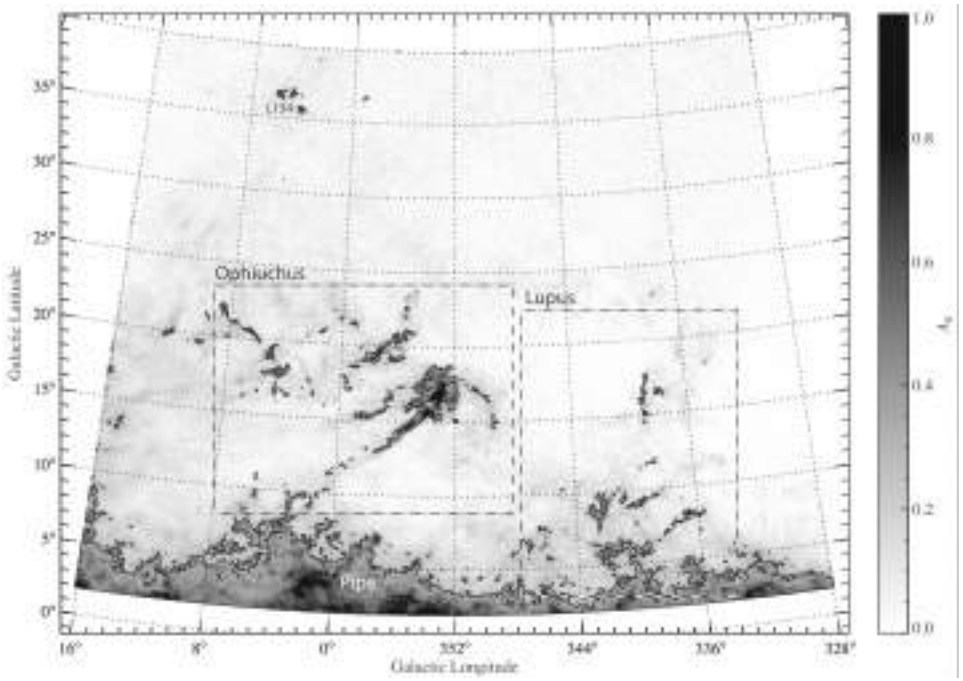

(a) Ophiuchus and Lupus MC from Lombardi et al. [159]

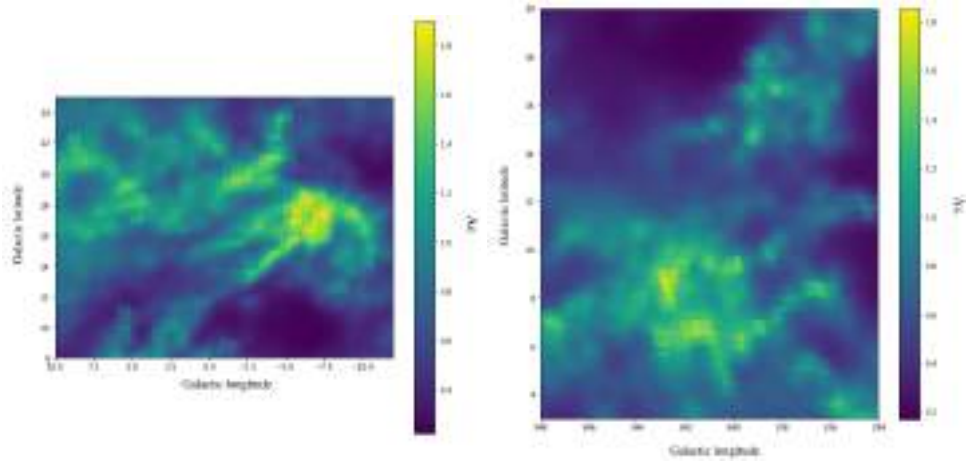

(b) Ophiuchus MC

(c) Lupus MC

Figure 4.7: Projection of *(a)* Ophiuchus and *(b)* Lupus molecular clouds from LGE2020 [157] in G band and *(c)* represent both Ophiuchus and Lupus in K bands from [159].

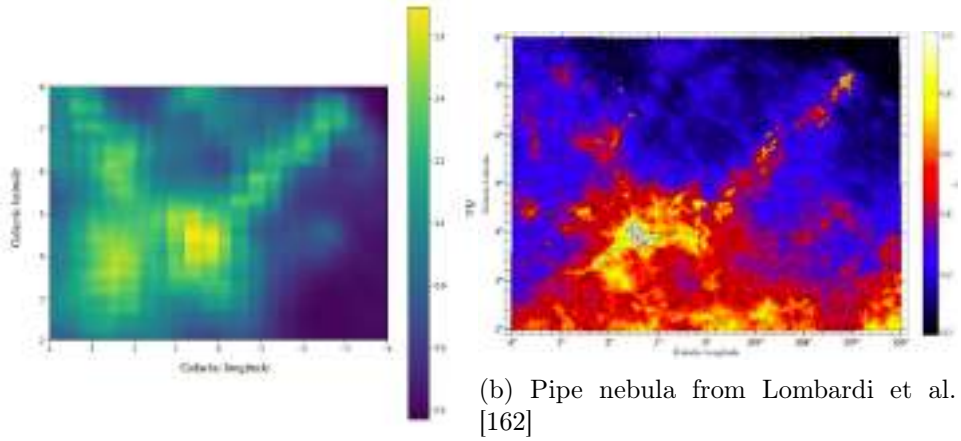

(a) Pipe nebula

(b) Pipe nebula from Lombardi et al. [162]

Figure 4.8: Projection of *(a)* Pipe nebula from LGE2020 [157] in G band and *(b)* represent Pipe nebula in K bands from [162].

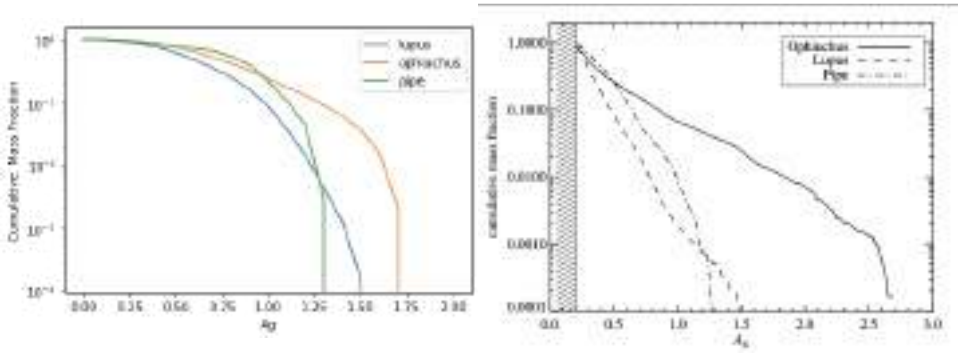

(a)

(b)

Figure 4.9: Cumulative mass fraction for Pipe nebula, Ophiuchus and Lupus clouds as a function of extinction for LGE2020[157] and Lombardi et al. [159]

Summary : The ISM plays an important role in the galactic ecosystem. It is present in the form of molecules, atoms and ions from temperature of 10 K up to 10^7 K in the hottest regions. ISM is composed by $\simeq$ 90.8% of hydrogen, 9.1% of helium and 0.1% of metals. Multiple surveys probe ISM through absorption and emission from gas and dust. We studied dust surveys based on the extinction of starlight due to presence of dust, which is linked to hydrogen column density by $N_{\rm H} = 2.87 \times 10^{21}\,{\rm cm}^{-2}\ A_{\rm V}/{\rm mag}$. We used the dust map produced by Leike et al.[157] (LGE2020), the authors used Gaia data to compute the extinction in the G band where $A_G/A_V = 0.789$. We check the consistency of our reconstructed map by computing the total average density on galactic plane and we found $\Sigma = 10.4\,M_\odot/{\rm pc}^2$ while it was computed $\Sigma = 13 M_\odot/{\rm pc}^2$ for the local surface density from Ref. [101]. We conclude that the LGE2020 dust map includes 80% of the total gas. After verifying the total amount of accounted gas we checked its distribution by looking for nearby molecular clouds at distance $\lesssim 300\,{\rm pc}$ and we compared the result with Lombardi et al. [162, 159, 160] maps. We noticed that LGE2020 maps restore accurately the gas distribution is the nearby environment with an unreached precision of $1\,{\rm pc}^3$, but fails to restore the total mass.

Chapter 5

Cosmic rays interactions in ISM

Cosmic rays interaction with the ISM during their propagation or in their acceleration sites produce secondary high energy photons and neutrinos. It is thus interesting to combine CRs, γ rays, and neutrinos observations to conduct a multi-messenger approach to astrophysical question. Figure 5.1 summarises well the inherent link between the three messengers : CRs, γ rays and neutrinos. While cosmic rays are affected during their propagation by GMF, photons and neutrinos being neutral point directly to their production sites as they are observed from Earth. In addition, neutrinos are stable and weakly interacting particles, thus they don't suffer energy losses, while photons can be strongly attenuated during the propagation.

In this chapter, we will discuss the neutrino and γ rays produced by VHE CRs. In section 5.1, we will present photons and neutrinos production channels, we will focus on hadronic interactions from the interaction of CRs with ISM. Section 5.2 will be dedicated to propagation of secondary photons and neutrinos, we will present some energy losses process, that play a major role

in gamma rays propagation. Then we will introduce briefly gamma rays and neutrinos astronomy and present the experiments currently used to probe them in section 5.3 and 5.4.

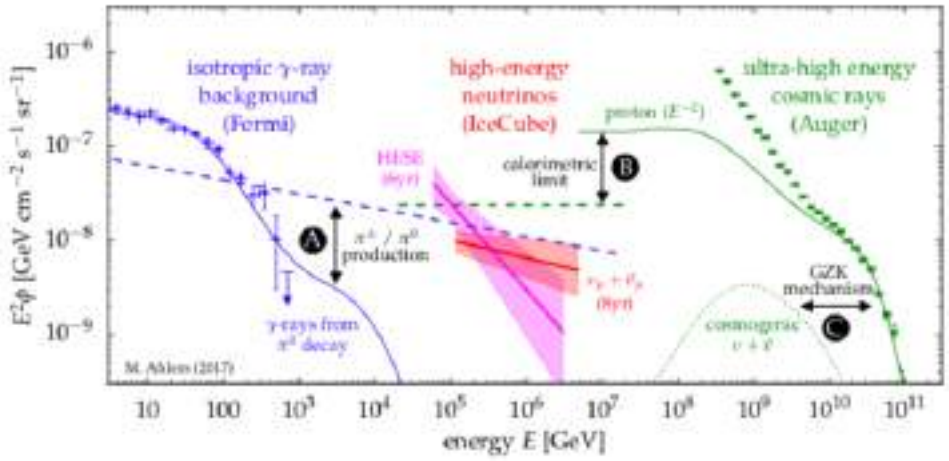

Figure 5.1: Ultra high energy cosmic rays, high energy neutrinos and γ rays plotted together. The spectral flux of neutrinos inferred from the eight-year upgoing track analysis (red fit) and the six-year HESE analysis (magenta fit), the flux of unresolved extragalactic γ-ray sources [17] (blue data) and ultra-high-energy cosmic rays from Ref. [83] (green data). Where is highlighted the various multimessenger interfaces: **A**: The joined production of charged pions ($\pi^{\pm}$) and neutral pions (π^0) in cosmic-ray interactions leads to the emission of neutrinos (dashed blue) and γ-rays (solid blue), respectively. **B**: Cosmic ray emission models (solid green) of the most energetic cosmic rays imply a maximal flux (calorimetric limit) of neutrinos from the same sources (green dashed). **C**: The same cosmic ray model predicts the emission of cosmogenic neutrinos from the collision with cosmic background photons (GZK mechanism). Figure from [29].

5.1 Neutrinos and gamma rays production

High energy CRs proton or nuclei interact with gas (pp) or ambient radiation ($p\gamma$). Hadronuclear pp interaction produces pions that decays producing

subsequently neutrinos

$$pp \rightarrow \begin{cases} \pi^0 \rightarrow \gamma\gamma \\ \pi^+ \rightarrow \mu^+\nu_\mu \rightarrow e^+\nu_e\nu_\mu\bar{\nu_\mu} \\ \pi^- \rightarrow \mu^-\bar{\nu_\mu} \rightarrow e^-\bar{\nu_e}\bar{\nu_\mu}\nu_\mu \end{cases} \tag{5.1}$$

Where finals neutrinos carry $\sim 5\%$ of the primary cosmic ray proton energy, while photons carry $\sim 10\%$.

Phothadronic interactions are resonant collisions via $\Delta^{\pm}$ resonnance.

$$p\gamma \rightarrow \Delta^+ \rightarrow \begin{cases} p\pi^0 \rightarrow p\gamma\gamma \\ n\pi^+ \rightarrow n\mu^+\nu_\mu \rightarrow ne^+\nu_e\nu_\mu\bar{\nu_\mu} \end{cases} \tag{5.2}$$

The cross section for $p\gamma$ is about 100 times smaller than pp channel, nevertheless in astrophysical objects the target photon density is usually higher than matter density.

The energy spestrum I_γ and I_ν follows closely the energy spectrum of the primary cosmic rays, see figure 5.2, where secondary γ and neutrinos fluxes are produced for a proton flux following $I_p \propto E_p^{-2}\exp(-E_p/E_0)$. One can see that noth neutrinos and γ-rays spectra follow $\propto E^{-2}$ power law.

The branching ratio of charged to neutral pions implies

$$E_\gamma^2 I_\gamma(E_\gamma) = 2E_\nu^2 I_\nu(E_\nu) \tag{5.3}$$

Neutrinos are produced at different flavour ratios depending on their production mechanism. However the expected ratio at Earth is $\nu_e : \nu_\mu : \nu_\tau = 1 : 1 : 1$ due to neutrino oscilliations.

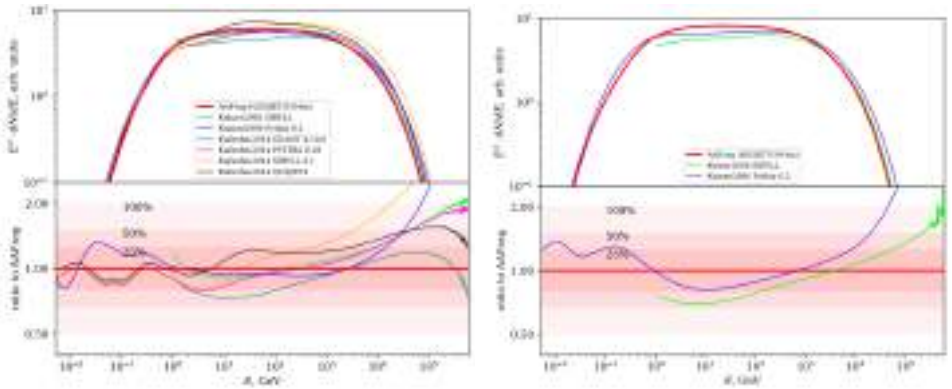

(a) γ-ray energy flux (b) Neutrinos energy flux

Figure 5.2: γ-ray (*left*) and neutrinos (*right*) energy fluxes for a power law primary proton spectrum, with an exponential cut off $\propto p^{-2}\exp((-p/p_0))$ with parameters $p_0 = 100$ TeV. Fluxes calculated with AAfrag using QGSJET-II-04m compared to the ones of Ref. [143] based on SIBYLL, Ref. [142] based on PYTHIA 6.2, and Ref. [139] based on GEANT 4.10.0, PYTHIA 8.18, and QGSJET-I. Figure from Ref. [146]

In addition to hadronic interaction, photons are also produced through leptonic channels via the interaction of relativistic electrons with radiation and matter. The main processes are : synchrotron radiation and inverse compton scattering. We will describe briefly the two processes and the resulting spectra.

Synchrotron radiation is the radiation emitted by a charged particle when it spirals around magnetic field lines. The power emitted for a particle with mass m, charge e and momentum $p_\perp$ perpendicular to magnetic field B in the classical limit is

$$P_{cl} = \frac{2}{3}\alpha m^2 (\frac{p_\perp}{m}\frac{eB}{m^2})^2 \tag{5.4}$$

The energy loss per time $dE/dt = -P \propto m^{-4}$, hence the principal sychrotron emitter in the universe are relativistic electrons.

Inverse compton scattering is when a relativistic electron transfer a large fraction of its energy to a photon producing a high energy gamma ray. For low energy photon, the scattering falls into the Thomson regime; while for high energies, quantum effect became important and the regime is called Klein-Nishina [129].

$$\sigma \simeq \begin{cases} \sigma_{th}(1 - \frac{s}{m^2}) & , \frac{s}{m^2} \ll 1 \\ \frac{3m^2}{4s}\sigma_{th}(\ln(\frac{s}{m^2} + \frac{1}{2}) & , \frac{s}{m^2} \gg 1 \end{cases} \tag{5.5}$$

Where σ_{th} is the thomson cross section $\sigma_{th} = \frac{8\pi\alpha^2}{3m^2e}$.

In leptonic cases the photon flux is modeled as the sum of both contribution from synchrotron and inverse compton, as shown in figure 5.3.

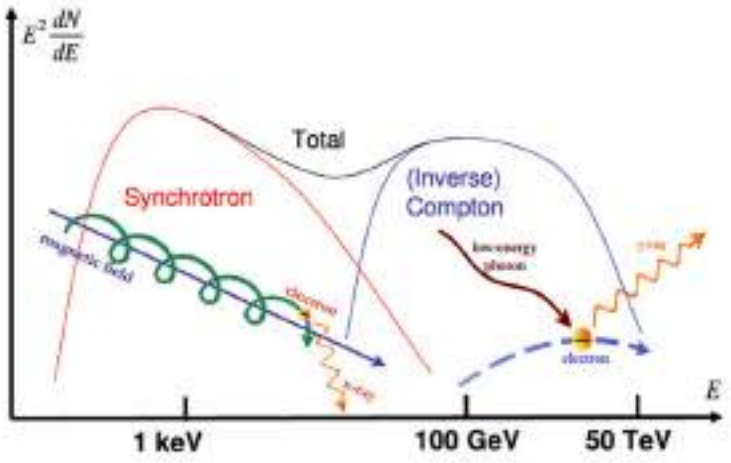

Figure 5.3: Cartoon scheme of characteristic differential energy spectrum of photons produced in synchrotron and in IC proceses. Figure from [85]

5.2 Gamma rays and neutrinos propagation

After their production, neutrinos and photons have to travel through ISM before being detected on Earth. Both particles being uncharged, they propagate in a straight line not deflected by magnetic field lines. But while neutrinos suffer only redshift losses, photons in addition to redshift lose energy through EM interactions. As shown in the figure 5.4, for $E_\gamma \gtrsim$ few MeV the dominant interaction channel is pair production.

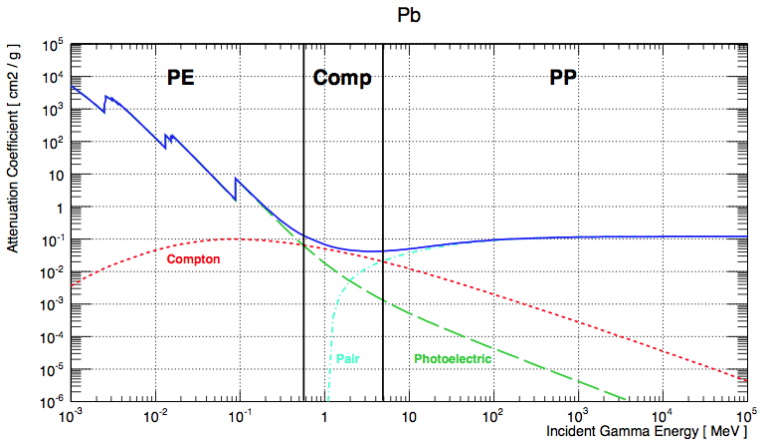

Figure 5.4: Gamma ray cross section in Pb. Figure from [95]

Pair production takes place in the field of the nucleus where the high energy photon interact with a background photon emitting e^+e^- pairs, and develop an electromagnetic cascade that will transform an initial γ-ray flux into a more intense X-ray flux. Figure 5.5 shows the mean free path of γ-ray photons in the extragalacitc medium. It appears that a photon with $E_\gamma \gtrsim 10^2$ TeV emitted by an extragalactic source wouldn't reach us before losing its energy. As a result the measurement of X- and γ-ray fluxes can be used together with high energy neutrino flux to constrains distance to their sources, and thus to CRs sources.

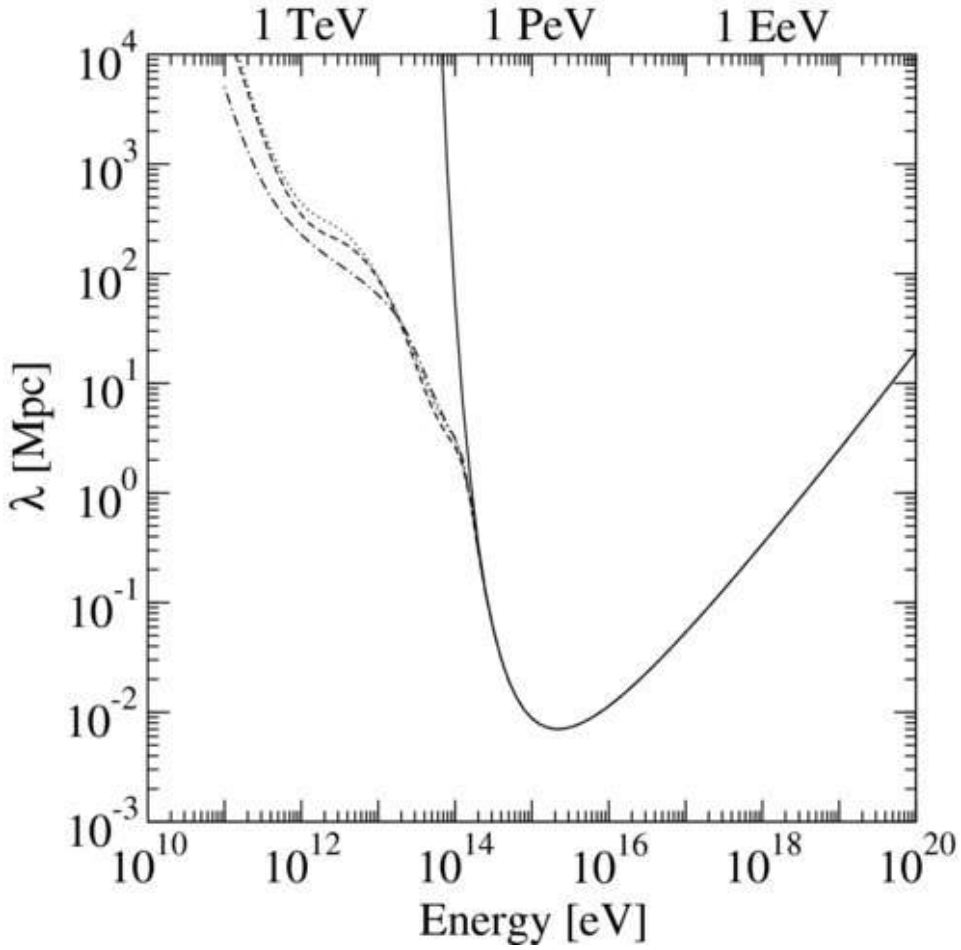

Figure 5.5: Pair production mean free path for VHE photons propagating through the present-day soft photon background as a function of energy for four different models of the background. *Solid*: Soft photon background consisting of only the CMB. *Dotted*: Soft photon background consisting of the CMB and Gilmore et al. model [115] of EBL.*Dot-dashed*: Soft photon background consisting of the CMB and Stecker et al. [194] model of EBL. *Dashed*: For comparison, the soft photon background consisting of the CMB and Kneiske [144] model of EBL. figure from [210]

5.3 Neutrino astronomy

First neutrino was discovered in 1956, opening the possibility of observing the sky with a new messenger, uncharged, essentially massless and weakly interacting. Where gamma rays above TeV are absorbed and cosmic rays

deflected, neutrinos travel freely from their sources to our detectors. The neutrino low interaction rate presents a huge advantage in probing astrophysical sources, but a big challenge in the ability to detect them. We will in this section present the most common detection technique and one of the currently used neutrinos detectors.

High energy neutrinos interact through neutral current (NC) or charged current (CC) with quarks in the target nucleus by exchanging a Z or W weak bosons.

Neutral current : produce at final state an outgoing neutrino that inherits most of the incoming neutrino energy. The target initiates a hadronic shower that presents the only signature of the interaction. This doesn't allow to reconstruct neither the energy nor the direction of the incoming neutrino.

Charged current : In charged current a charged lepton is produced, sharing same flavor as the initial neutrino and approximately 80% of its energy. The nucleus target initiates hadronic shower in the medium. The common method to detect neutrino is from observing the secondary charged particles moving inside the detector and emitting Cherenkov radiation or electromagnetic shower. The signature of the event depends on the flavor of the produced lepton. We can distinguish two possible signal classes :

Tracks : refer to the emission of a long-lived muon. The muon can travel several kilometers before being stopped or decaying thanks to its ultra-relativistic speed. At high energies, the produced muon is expected to be collinear with the incoming neutrino.

Since the trajectory of the muon is well reconstructed, track events offer high angular resolution of the detected muon and thus of the parent neutrino. But when the muon is produced outside the detector it is difficult to guess the energy lost before reaching the detector and thus the energy reconstruction of the initial neutrino is uncertain [28].

Cascade event : concerns shower like event that can be induced by an electronic or a tau neutrino. In the case of ν_e an electron is produced that immediately interact with the medium. The produced e^- initiate an electromagnetic cascade that will be superimposed on the hadronic shower produced by the nucleus target. The ν_τ will produce a τ lepton that, because of its small lifetime, will decay fast producing either a hadronic of an electronic shower. At few TeV, the hadronic cascade produced by the target and the one produced by the τ decay couldn't be distinguished, but at PeV the two signals start to be observed separately giving a remarkable double signature to the event, at much higher energies the τ may exit the detector before decaying and thus produce an muon like signal, i.e a track. Cascade event deposit a big fraction of their energy in the detector, making the energy reconstruction of the initial neutrino easier. In the opposite, angular reconstruction is more complicated, since both the hadronic cascade produced by the struck target and the shower produced by the produced lepton usually superimpose in a mostly spherical pattern [28].

Figure 5.6 summarises the detection signals for each event. We notice that NC events for ultra high energy neutrinos is similar to cascade event of a very high energy neutrino, and tau neutrino can either produce a cascade,

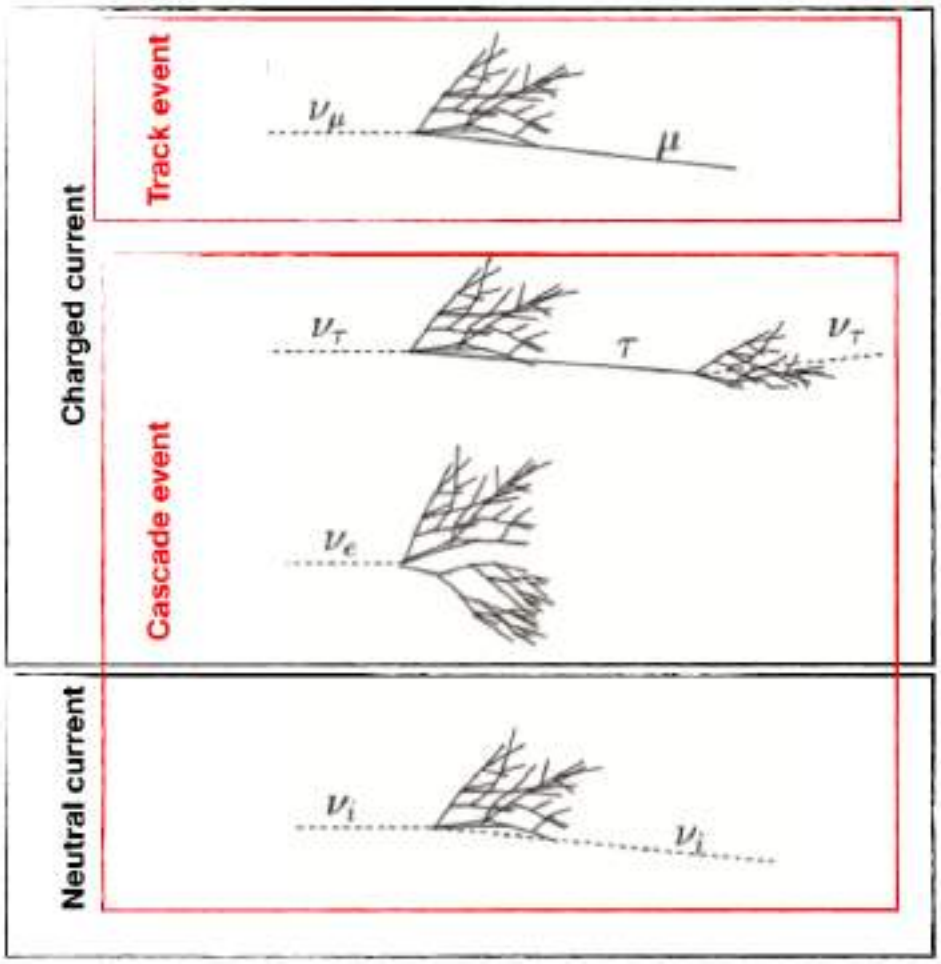

Figure 5.6: Cartoon illustrating several observed signals depending on the flavor of the incident neutrino.

a double cascade or a track event depending on its energy.

Neutrinos and muons are also largely produced in the atmosphere, in the extensive air shower initiated by very high energy CRs. To reduce muon background, the observation of tracks is limited to tracks produced in detector of up going tracks using Earth as a shield against atmospheric muons as shown in figure 5.7.

This condition doesn't prevent against an atmospheric neutrino background that are indistinguishable from astrophysical neutrinos. However,

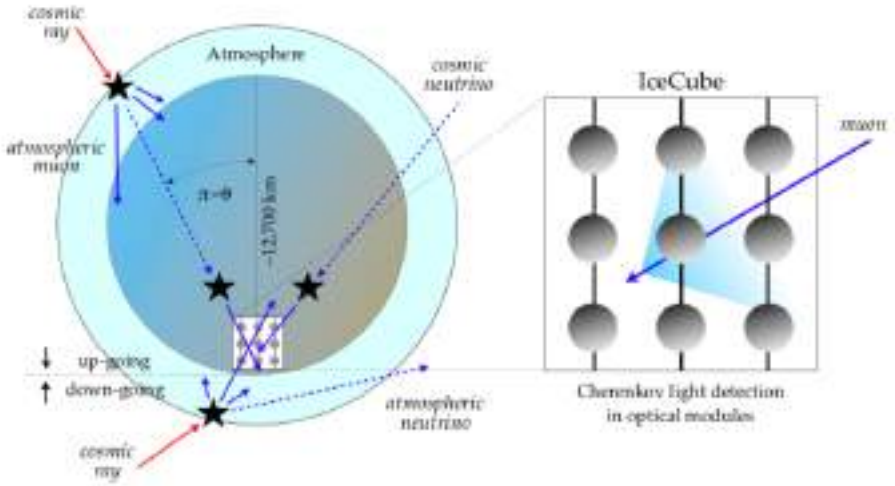

Figure 5.7: The background of high-energy muons (solid blue arrows) produced in the atmosphere can be reduced by placing the detector underground. The surviving fraction of muons is further reduced by looking for upgoing muon tracks that originate from muon neutrinos (dashed blue arrows) interacting close to the detector. Figure from[29].

atmospheric neutrino follows a steep power spectrum $\propto E^{-3.7}$ and this allow to compute a diffuse astrophysical neutrino emission for $E > few\,\mathrm{TeV}$ as seen in figure 5.8.

Tracks upgoing event limit neutrino observations to a single flavor coming from half of the sky. To extend the study to the all sky, an alternative method is to identify high energy neutrino interactions in the detector, so called "High Energy Starting Events" HESE. HESE events include both muon tracks and secondary shower that accompany electron and tau neutrino as well as neutral current [28]..

From all this considerations, it is interesting to compute the expected event rate for a neutrino detection. For a track event, the event rate of

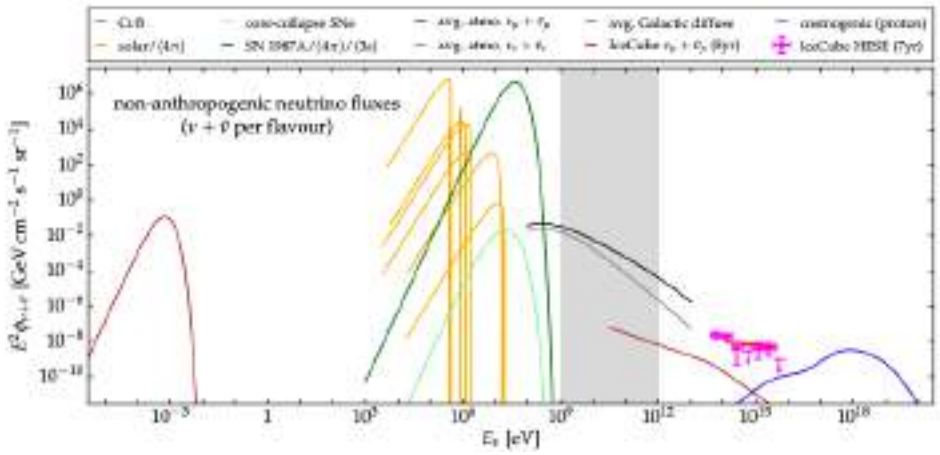

Figure 5.8: Cosmological, astrophysical and atmospheric neutrino spectra (predicted or detected). The GeV–TeV energy region. Grey shaded region represents the region where the astrophysical flux is expected to be dominated by *pp* interactions. Figure from [30].

muons with energy $E > E_{min}$ in a detector of area A is

$$\text{Rate} = A \int dE d\Sigma P_\mu(E, E_\mu^{min}) S(E) I_\nu(E_\nu) \tag{5.6}$$

Where $S(E)$ is the shadow factor and it takes into account the attenuation in Earth. $P_\mu(E, E_\mu^{min})$ is the probability that a muon is created and reaches the detector with $E > E_{min}$. We can approximate $S \sim (E/E_{min})^{-0.2}$ and $P_\mu/sim10^{-3}(E/E_{min})^{0.8}$. Hence, if we assume $E_{min} \sim$PeV we expect $\sim$ 100 events for a km^3 detector [1]. Immense particle detectors are required to collect a statistically significant number of neutrinos. The need for a kilometer scale detector was already understood in 1970's [29]. Markov [164] first suggested to use a large volume of deep natural water as a Cherenkov detector.

An example of neutrino detector is IceCube. It is a neutrino observatory situated in Antartica in the South Pole. It used pure transparent Ice for

[1] For detailed calculation, please see Ref. [129]

Cherenkov detection. The detector consists on a km^3 volume located at 1.5 km depth and instrumented with photomultipliers, figure 5.9 shows the global structure of the detector.

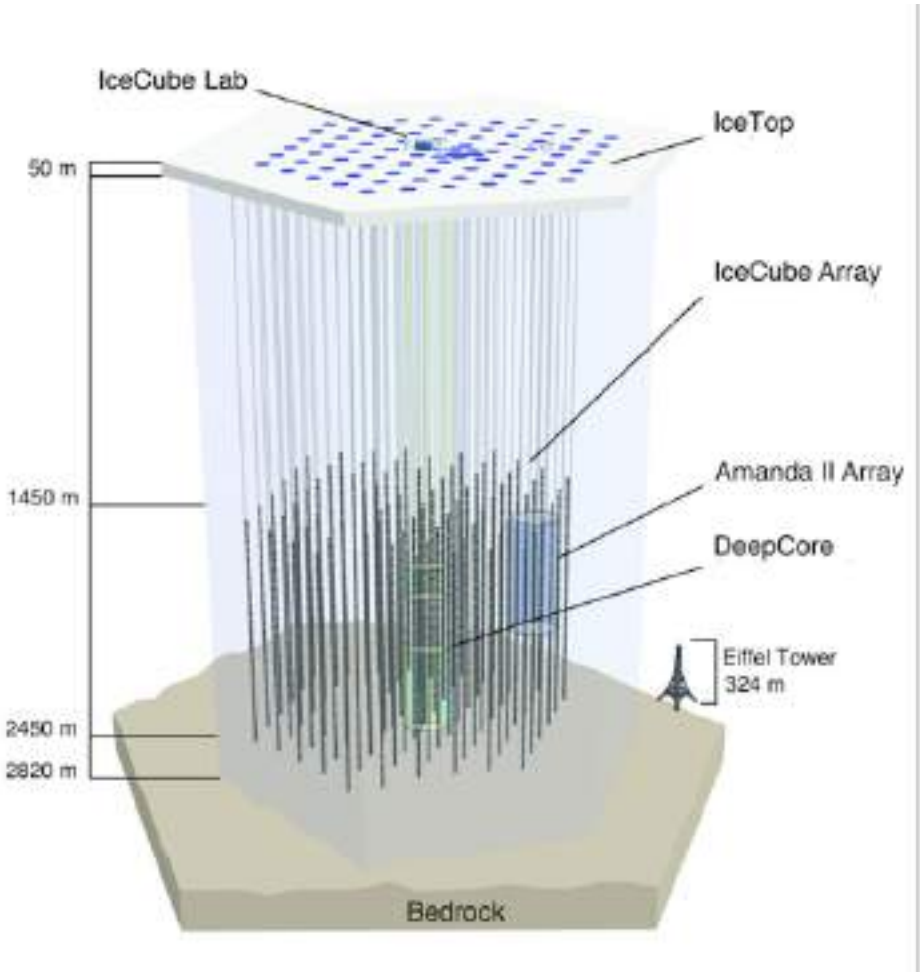

Figure 5.9: A perspective view of a fully instrumented IceCube detector, with the different sub-detectors Deep core (shaded region in the center), AMANDA (blue shaded cylinder) and IceTop in the top of the detector (blue circles). Figure from [29]

IceCube succeeded to a pre-existing detector AMANDA and its deployment were held from 2003 up to 2011.

It also contains a surface array detector "IceTop" that we already presented as a CRs detector, but IceTop has another mission, it is used as a veto against

the atmospheric muon background. A denser detector is installed at the center of IceCube called "Deep Core" characterised by smaller spacing strings in order to reduce the energy threshold of the detector up to $\sim 10\,\mathrm{GeV}$. Using Ice for detection complicates neutrino arrival direction reconstruction since the optical properties of the detector depends on Ice model.

IceCube will be upgraded during next 2 years. For future, a bigger project "IceCube Gen2" is under design. The proposed detector will cover a volume of $8\,\mathrm{km}^3$ and will host radio detector to raise the detectable energy threshold up to $\sim 10\,\mathrm{PeV}$.

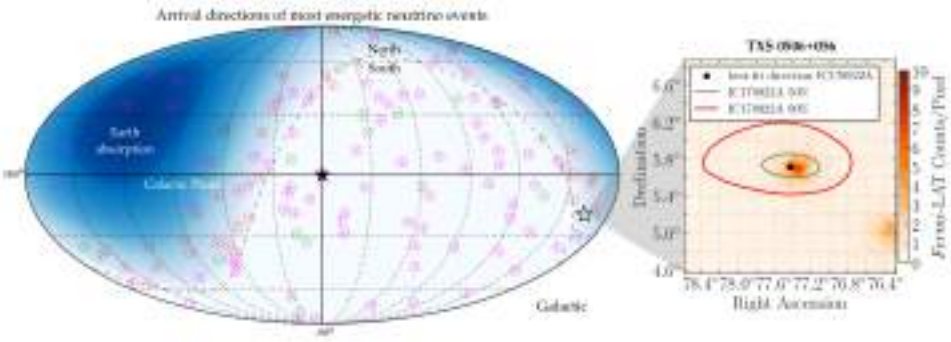

Figure 5.10: Mollweide projection in Galactic coordinates of the arrival direction of neutrino events. The current sky map of highly energetic neutrino events detected by IceCube , upgoing track analysis ($\odot$),high-energy starting event (HESE) (tracks $\otimes$ and cascades $\oplus$). The location of the first compelling neutrino source, blazar TXS 0506+056, is marked with a star. Shown in the inset are the related Fermi LAT measurements of the region centred on TXS 0506+056 from September 2017 [5]. Figure from [8]

Figure 5.10 resume IceCube neutrino events from all channels. It also shows the first compleling neutrino source, blazar TXS0506+056.

From all these events the spectrum was reconstructed as shown in figure 5.11 for HESE events.

Track events are measured above 200 TeV and the spectrum is consistent

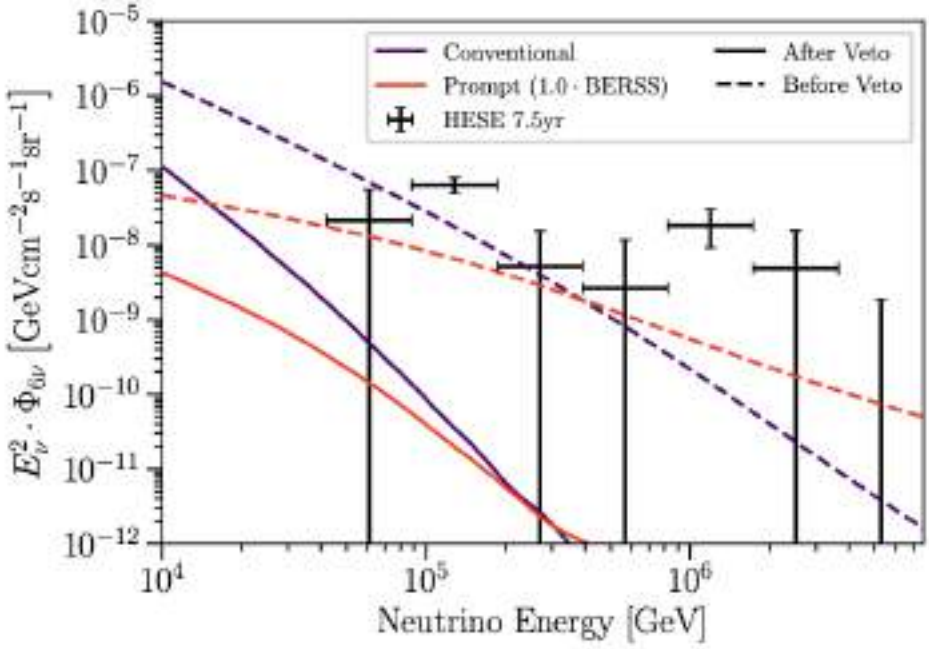

Figure 5.11: All-sky average astrophysical neutrino flux and atmospheric neutrino fluxes before and after the veto. The atmospheric neutrino fluxes considered are shown as dashed lines. The solid lines show the product of the atmospheric flux with the passing fraction averaged over depth at a zenith angle of 0°. This comparison demonstrates the effect of the veto in the down-going region, where it is strongest. The atmospheric flux suppression becomes weaker towards the horizon and is not present in the up-going region. The dashed lines labeled "before-veto" are equivalent to the up-going atmospheric fluxes, with or without the veto, neglecting Earth absorption effects. [10]

with a power law following [3]

$$E^2F(E) = (4.32 \pm 0.9) \times 10^{-8}(\frac{E}{100\,\text{TeV}})^{-0.3\pm0.1}\frac{\text{GeV}}{\text{cm}^2\text{s sr}} \tag{5.7}$$

Cascade events energy spectrum follow also a power law [3]

$$E^2F(E) = (4.92 \pm 1.1) \times 10^{-8}(\frac{E}{100\,\text{TeV}})^{-0.53\pm0.1}\frac{\text{GeV}}{\text{cm}^2\text{s sr}} \tag{5.8}$$

5.4 Gamma rays astronomy

The electromagnetic observation of the sky extends from radio to γ-ray wavelength. Figure 5.12 show the wavelength, frequency and energy dependence. The development of space telescopes allows to observe the universe at wavelengths beyond the optical and thus to study much higher energy sources. Many surveys contributes to produce a multiavelength sky maps, in the following we will focus on γ rays. γ-ray band covers a broad energy range from 10^2 GeV to $few \times 10^2$ TeV. Below $\sim$ 100 GeV, observations are exclusively carried from space. Higher energies are observed from the ground by detecting the Cherenkov light produced by γ-rays in the atmosphere.

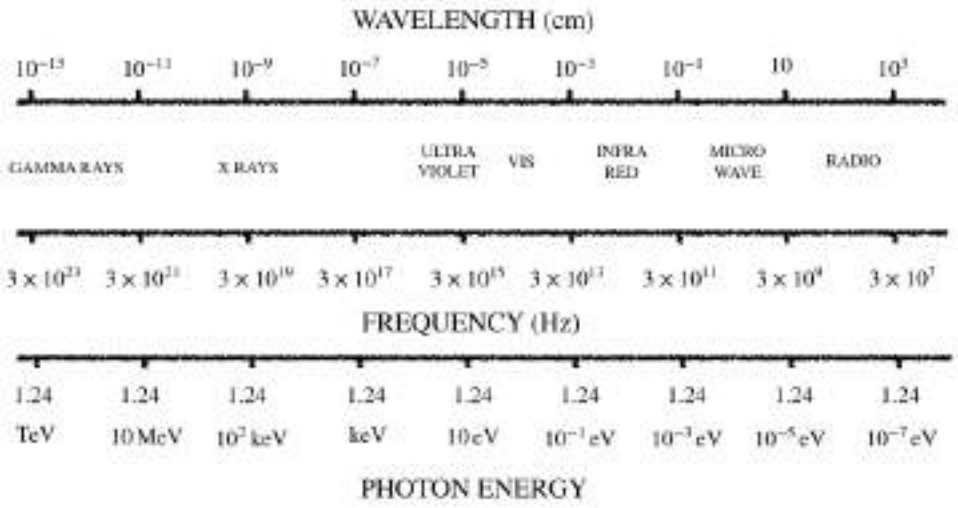

Figure 5.12: Scheme of the different domains of the electromagnetic spectrum in wavelength, frequency and energy.

Fermi is a gamma-ray space telescope that detects photons from 8 keV to 300 GeV. It was launched in 2008 in an orbit of 535 km altitude and since then it circles the Earth each 96 min. Fermi carries two instruments : the Large Area Telescope (LAT) and the Gamma-ray Burst Monitor (GBM).

The LAT instrument has a large field of view equivalent to 1/5 of the sky, and observe gamma-ray sources from 30 MeV to 300 GeV. It is composed by 3 detectors : a tracker measuring paths of the e^+e^- pair produced by the incident photon; a calorimeter to measure the photon energy and an anticoincidence detector to isolate CRs background. This allows Fermi LAT to be the first experiment to produce a diffuse γ-rays sky map at hundred GeV that is shown in figure 5.13. It also permits many discoveries such as Fermi bubbles observed for the fisrt time by Fermi and clearly appearing in the same figure 5.13.

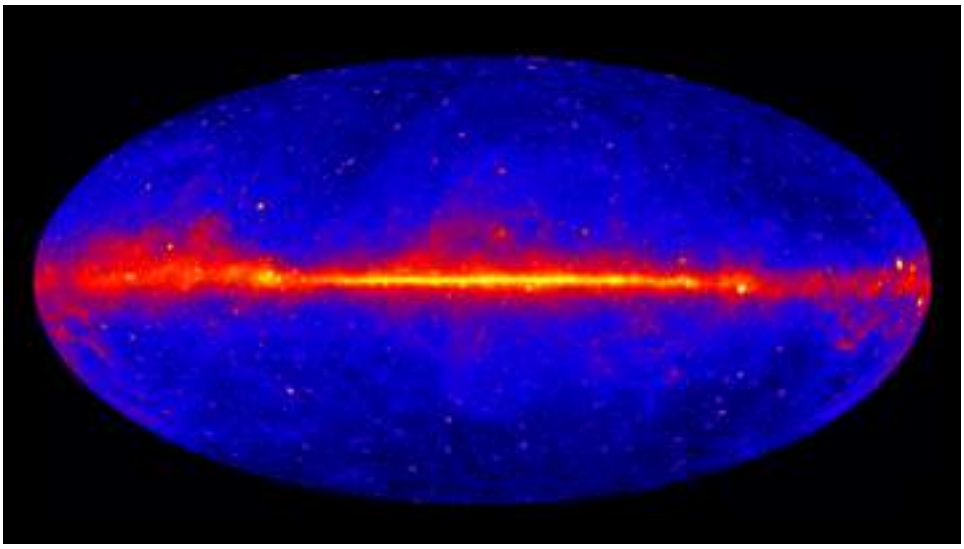

Figure 5.13: The Fermi LAT 60-month image, constructed from front-converting gamma rays with energies greater than 1 GeV. The most prominent feature is the bright band of diffuse glow along the map's center, which marks the central plane of our Milky Way Galaxy. The gamma rays are mostly produced when energetic particles accelerated in the shock waves of supernova remnants collide with gas atoms and even light between the stars. Hammer projection. Image credit: NASA/DOE/Fermi LAT Collaboration.

Fermi was also the first to observe a γ-ray signature of neutral pion decay from SNR, confirming the hypothesis of possible CR acceleration in snupernovae remnant [80].

LHAASO (Large High Altitude Air Shower Observatory) is a ground based gamma-ray detector. LHAASO was built in 2016 to be the most sensitive γ-ray telescope at energies from 10^{11} to 10^{17} eV. It started collecting data from 2019.

It is installed at 4410 m of altitude in the Sichuan province in China. It is composed on multiple detectors : a km^2 array (KM2A) for electromagnetic particle detection(ED), a km^2 array of underground Cherenkov detector tank for muon detection (MD); a closed pool of 78000 m^2 of water Cherenkov (WCDA) and 12 wide field of view air Cherenkov telescopes (WFCTA) [193].

One of the most important characteristics of LHAASO is its high altitude location that puts the observatory near the depth of the EAS maximum allowing thus a better sensitivity. Figure 5.14 show different observatories sensitivities, it appears from the figure that LHAASO is a unique telescope to observe photon of $\gtrsim$ hundreds TeV [193].

Figure 5.15 shows the diffuse γ-ray spectrum produced by Fermi LAT, where most γ-ray signal originate from π^0 decay in the Galaxy. Other discrete sources contribute to the total γ-ray flux such as pulsars, AGN, γ-ray bursts and some others.

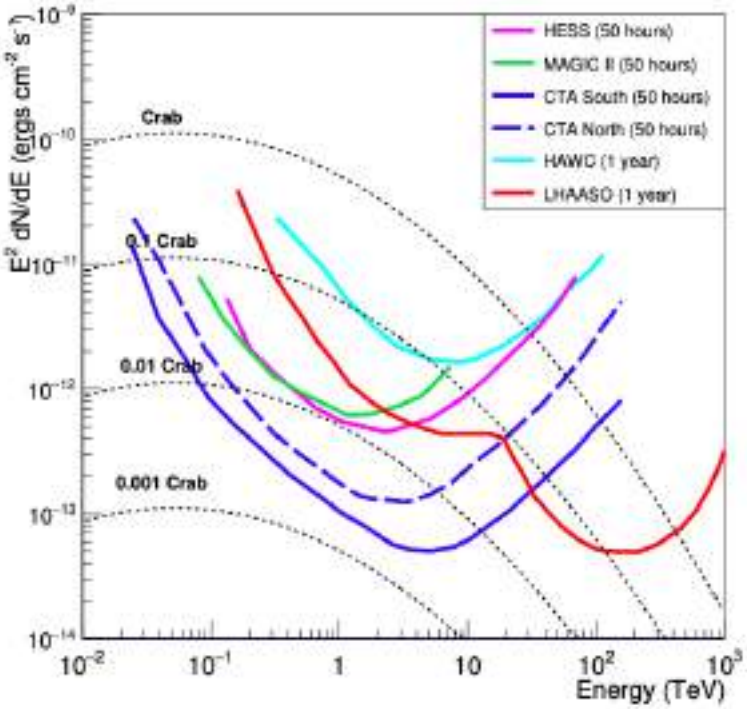

Figure 5.14: Differential sensitivity of LHAASO to a Crab-like point gamma ray sources compared to other experiments (multiplied by E2) from Ref. [193].

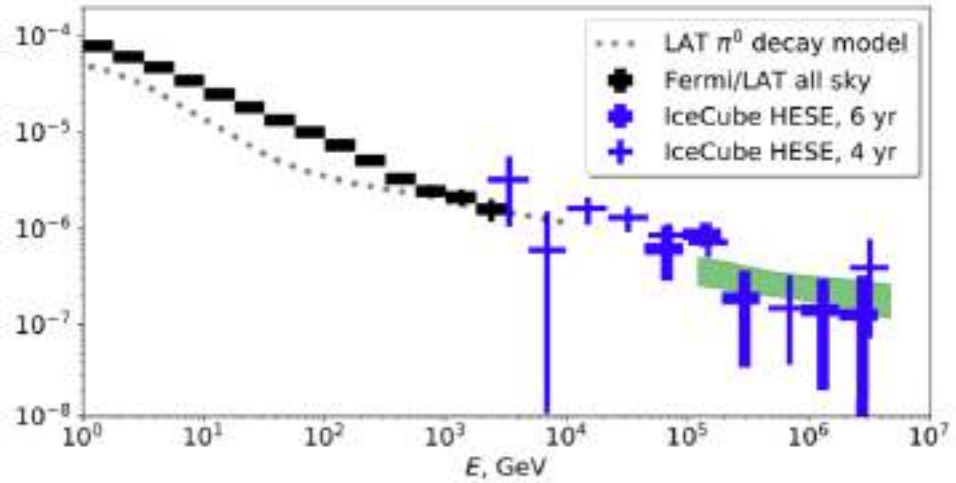

Figure 5.15: The multi-messenger spectrum of the full sky. Fermi LAT spectrum of γ-ray emission is shown by black data points. IceCube data are shown by blue data points and by the green bow-tie (from Ref. [7]). The dash-dotted curve shows the model of Galactic diffuse emission component from π^0 decays [16]. Figure from [167].

Summary : While propagating, CRs cross regions in the sky filled with matter and/or radiation. A fraction of CRs interact through hadronic processes producing pions. While neutral pions decay to 2γ, charged pions produce ν. Neutrinos and photons are produced with comparable statistics and energy in the source, but neutrinos travel freely while photons suffer energy losses via e^+e^- pair production. Comparing high energies, neutrino and γ-ray fluxes inform us on their sources, thus VHE CRs sources.

Neutrino astronomy is complicated because of the weak coupling of neutrino with matter. Large detectors were built in order to allow reasonnable amount of observations of astrophysical signals. IceCube is one of the biggest currently running detectors, it uses km^3 block of ice to detect Cherenkov light emitted by lepton daughter of the initial astrophysical neutrino. It observes neutrinos through two channels, cascade and tracks. Because of the atmospheric background, the astrophysical energy spectrum is constructed by IceCube above $\sim$ hundreds of TeV.

γ-ray astronomy is also recent. It was made possible thanks to space telescopes such as Fermi that observes photons up to 300 GeV. Higher energy photons are observed by ground based telescopes through the extensive air shower emitted when they reach the atmosphere. A new telescope LHAASO was built in order to be the most sensitive at PeV energy range and it started collecting data since 2019.

Chapter 6

Neutrinos and gamma rays from local sources

High-energy astrophysical neutrinos are a unique probe to understand the non-thermal universe [105]. They are produced together with photons in interactions of cosmic rays (CR) on matter and background photons close to their sources and during propagation.

In Ref. [170], evidence for a Galactic contribution in the HESE neutrino data was found based on both the signal in the Galactic plane and at high Galactic latitudes. Two-component models with a Galactic and an extragalactic contribution were suggested in Refs. [171] and [177] to explain the data in both the muon and cascade channels. A non-zero Galactic contribution was obtained also more recently in a multi-component fit performed in Ref. [178]. Finally, a gamma-ray excess at high Galactic latitudes in the Fermi LAT data with energies $E > 300\,\mathrm{GeV}$ was reported in Ref. [167, 172]. Since at these energies photons are strongly attenuated by pair-production on cosmic background photons, these multi TeV photons should have a largely Galactic origin. We studied the possibility is that the main contribution to the

Galactic neutrino flux is rather local, produced by CRs interactions in the nearby ISM.
In section 6.1 we studied the contribution of secondary neutrinos and γ rays produced by Vela CRs already presented in 3.4 interacting in the Local Bubble walls.

In section 6.2 we extended our work and we studied if the nearest Galactic CR accelerators may be visible as neutrino sources. We discussed the eventuality that the brightest spots in the Galactic neutrino sky may be gas clouds immersed into the CR overdensities close—but not close enough to be visible in TeV gamma-rays—to nearby young CR sources [136].

6.1 CR and secondary fluxes from Vela

We already studied the CRs flux expected from Vela for proton and heavier nuclei in section 3.4. In addition to the high magnetic field, the Local Bubble walls are also characterized by high density. We estimated the CRs intensity in the walls $\gtrsim$ 10 times than the one observed on Earth. We may then estimate in this case the the neutrinos and γ-rays produced in Local Bubble walls fluxes.

6.1.1 Cosmic rays fluxes

In Fig. 3.7, we estimated the normalised proton flux in the bubble wall, inside the bubble and around the source, for the cases U (top panel) and JF (bottom panel). Protons and heliums are expected to have the dominant contribution to *hundreds* TeV neutrinos and γ-rays secondaries, since the energy per nucleon decrease drastically for heavier nuclei.

In Figure 6.1, we show the proton and helium fluxes from Vela in the bubble wall and on Earth compared to the data from Refs. [117, 216, 47].

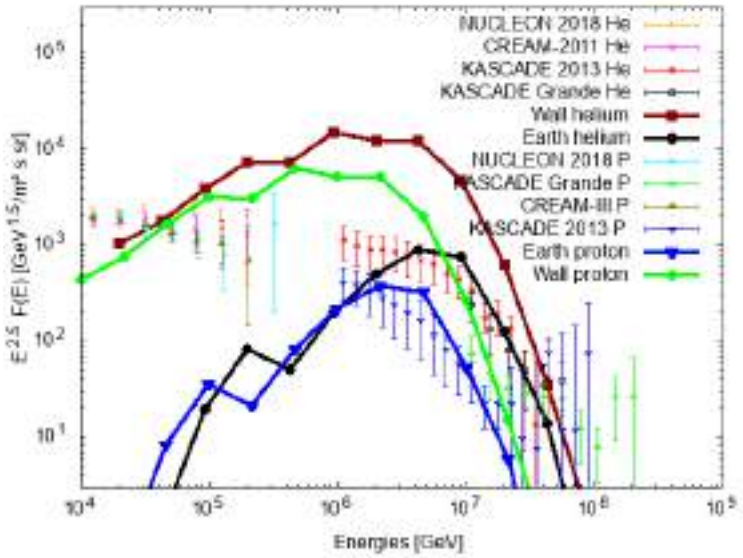

(a) caseU

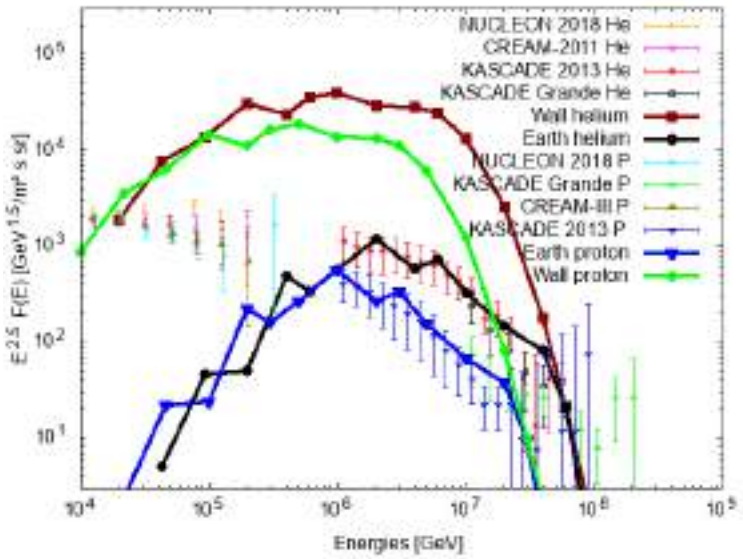

(b) caseJF

Figure 6.1: Contribution of Vela to the proton (green and blue) and helium (dark-red and black lines) fluxes in the bubble wall and at Earth compared to the data from Refs. [117, 216, 47]; top panel for case U, lower panel for case JF.

To compute the secondaries production we used the AAfrag program [174, 175]. Since the concept of a "nuclear enhancement factor" is not well

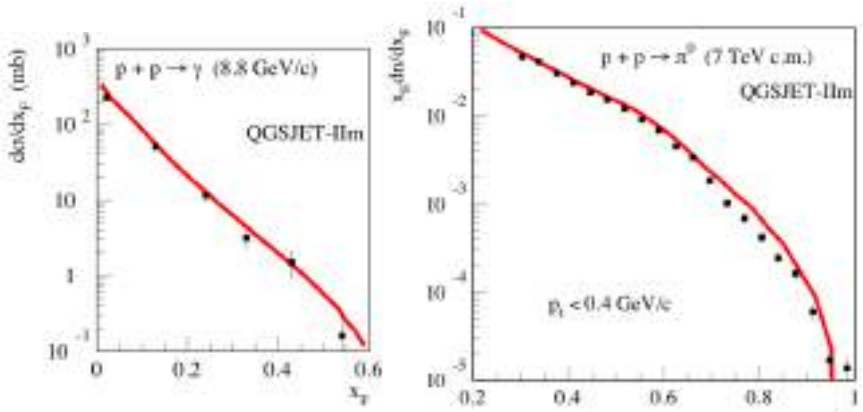

(a) $pp \to \gamma$

(b) $pp \to \pi$

Figure 6.2: *left :* Calculated Feynman x spectra $d\sigma^{\gamma}_{pp}/dx_F$ of photons in the C.m. frame for pp-collisions compared to experimental data *.right :* Calculated invariant energy spectrum $x_E dn^{\pi^0}_{pp}/dx_F$ of neutral pions in the c.m. frame for pp-collisions compared to the LHCf experimental data. Figure from Ref. [133]

defined [132, 133], we employ the Monte Carlo generator QGSJET- II [174, 175] to calculate the photon and neutrino secondary fluxes.

AAfrag is an interpolation routine for production secondary spices from proton-proton, proton-nuclei, nuclei-proton, nuclei-nucleil interactions. It uses QGSJET- II-04m model which was improved based on experimental data from LHCf, LHCb and NA61. The program is available on `https://aafrag.sourceforge.io`. The quality of the description of secondary particle production by QGSJET- II-04m model is illustrated in figure 6.2, where we can see that both at low and high energies the data set is well described by the results of QGSJET- II-04m.

The program structure is described in details in Ref. [133], we will here describe the different input and output. The program consists of two files `AAfrag101.f90` and `user101.f90` . The latter contain a sub routine `user_main` where we can fix type of interaction through

a parameter `k`, the energy of the incident particle `E_p` in GeV, then the program write in files as output the differential cross section in the form of $E_s^2 \times d\sigma^k/dE_p$ as a function of the energy of the secondary particle E_s, from `E_s` that can be fixed in the same subroutine, up to `E_p`.

For the target material we assume a mass fraction of 24% of Helium in the target gas and calculate the average intensity of the secondaries as

$$I_i(E) = \frac{c}{4\pi} \sum_{A\in\{1,4\}} \int_E^\infty \mathrm{d}E' \, \frac{\mathrm{d}\sigma_{\mathrm{inel}}^{pA\to i}(E', E)}{\mathrm{d}E} \tag{6.1}$$

$$\times \int \mathrm{d}^3x \, \frac{n_p(E', \vec{x}) n_{\mathrm{gas}}^A(\vec{x})}{d^2} \,, \tag{6.2}$$

where $\sigma_{\mathrm{inel}}^{pA}$ is the production cross section of secondaries of type i in interactions of protons on nuclei with mass number A, d denotes the distance from the Sun to the interaction point $\vec{x}$, $n_p(E, \vec{x})$ the differential number density of CR protons and $n_{\mathrm{gas}}^A(\vec{x})$ the density of protons and Helium in the bubble wall.

In Fig. 6.3 we compare the flux of neutrinos (red circles) and gamma-rays (magenta crosses) produced by CR interactions in the wall of the Local Bubble to Fermi LAT and IceCube measurements. The IceCube neutrino data consists of the muon neutrino channel with measurements above the atmospheric background at $E > 100\,\mathrm{TeV}$ (green band) and cascade events which show an excess with respect to the continuation of the muon neutrino flux at $E < 100$ TeV (red data with errorbars). Additionally, we show the neutrino flux from extragalactic sources as a thin black line for a $1/E^{2.1}$ power law, and the sum of the Galactic and extragalactic contributions with a thick black line. One can see that the sum of the two neutrino fluxes well

fits the IceCube data.

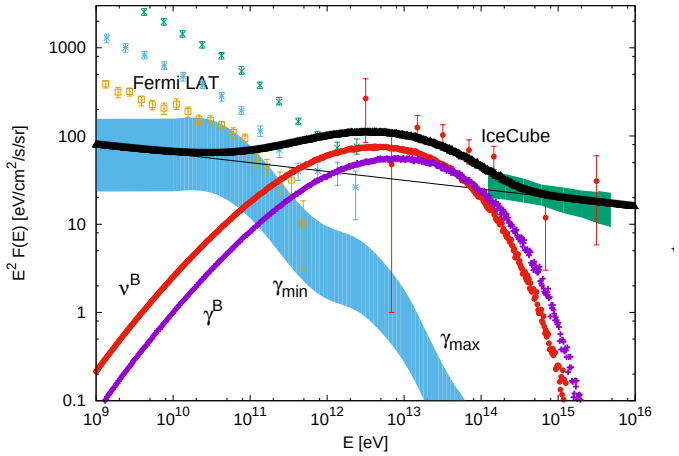

(a) caseU

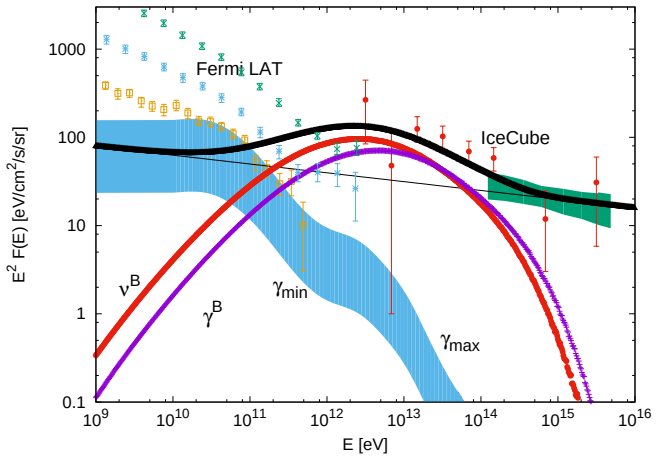

(b) caseJF

Figure 6.3: Multi-messenger contribution in neutrinos and gamma-rays of cosmic ray interactions in the walls of Local Bubble compared to Fermi LAT and IceCube measurements, for caseU in the top and caseJF in the bottom. Neutrino and gamma-ray fluxes from our model are presented with red circles and magenta crosses. Neutrino flux from extragalactic sources and total neutrino flux including contribution of bubble are presented with with black lines for $1/E^{2.1}$. Corresponding diffuse gamma-ray flux from extragalactic sources give contribution within blue strip normalized to diffuse gamma-ray background measured by Fermi LAT, presented with orange error-bars. Average diffuse gamma-ray flux at high galactic latitudes $|b| > 20°$ is presented with blue points and middle Galactic latitude flux $10° < |b| < 30°$ with green points.

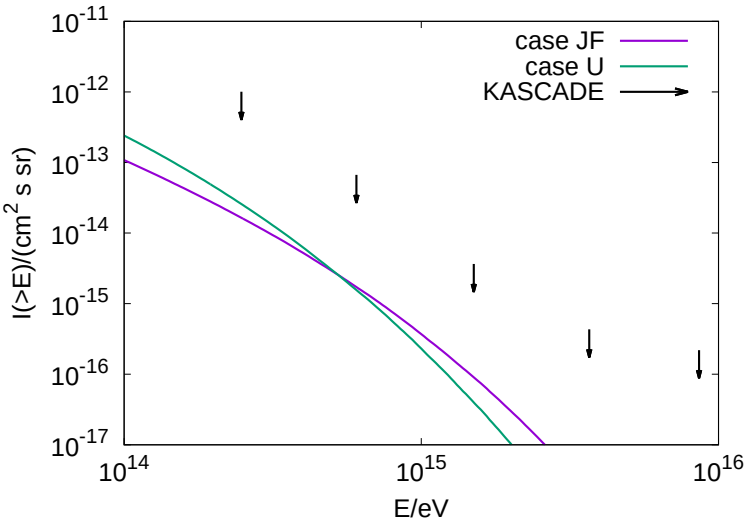

(a)

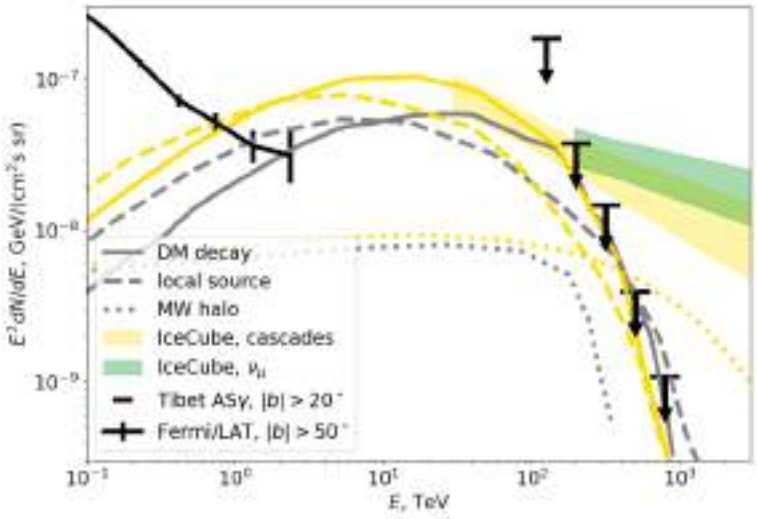

(b)

Figure 6.4: *(a) :* Integral photon flux from cosmic ray interactions in the walls of Local Bubble compared to KASCADE limits.*(b) :* Tibet ASγ limit on high Galactic latitude γ-ray flux compared to Fermi LAT measurements at lower energies from Ref. [172] and to model predictions of neutrino (yellow lines) and γ-ray (grey lines) fluxes for the local cosmic ray studied in this thesis (dashed lines), dark matter decay [167](solid), and 100 kpc scale halos of the Milky Way [187] (dotted). Yellow and green areas show the astrophysical neutrino spectrum measurement in cascade [3] and muon [195] channels. Figure from Ref. [169].

The extragalactic diffuse gamma-ray flux measured by Fermi LAT is shown with orange errorbars together with estimates for the contributions to the gamma-ray flux from extragalactic neutrino sources. The minimal flux close to the lowest values in the blue band corresponds to an $1/E^2$ neutrino flux, while the highest values is normalized to the measured diffuse gamma-ray background. Since up to 85% of this background comes from unresolved blazars, the contribution of all other sources is restricted to the lowest part of the blue band, corresponding to an $1/E^2$ neutrino flux. The average diffuse gamma-ray flux at high galactic latitudes $|b| > 20^\circ$ is presented with green points. This flux is dominated by the diffuse emission in the local part of our Galaxy. In addition to the expected cutoff in the diffuse emission above 100 GeV one can see a new hard component at $E > 300$ GeV, found in Ref. [167]. This component is fitted with the gamma-ray flux from the walls of the Local Bubble.

The integral photon flux from CR interactions in the wall of the LB are compared to KASCADE and TibetASγ limits in Fig. 6.4. In order to detect this photon flux, new more sensitive experiments are required. The flux level of gamma-rays predicted in our model at PeV energies may be measured by CR experiments with a high hadron rejection power, like CARPET-3 [92] or LHAASO [193].

6.2 Neutrinos and gamma rays from Cygnus Loop

Since neutrinos and gamma rays don't follow magnetic field lines while travelling, we should not restrict ourselves to sources connected tu us by magnetic field lines. We study in this section other local sources and consider the possibility that one of the nearest Galactic CR accelerators may be visible as neutrino sources.

6.2.1 Local matter density from dust maps

To model the matter distribution in the nearby ISM we used the LGE2020 dust maps, introduced in section 4.3. We calculated the hydrogen column density as follows.

$$N_{\mathrm{H}} = 3.63 \times 10^{21}\,\mathrm{cm}^{-2}\; A_{\mathrm{G}}/\mathrm{mag}. \tag{6.3}$$

In addition, we account for helium, which contributes 9.1% to the number density of the ISM.

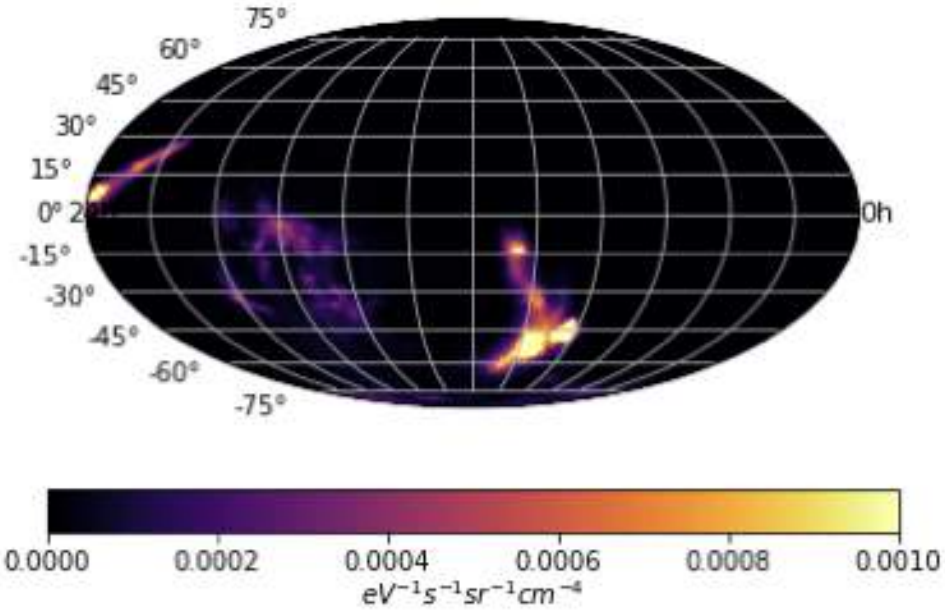

Figure 6.5: The function $\Xi^{pp}(E, l, b)$ in Galactic coordinates for the proton energy $E_p = 3\,\mathrm{PeV}$.

Combining the obtained matter map with the CR densities and integrating along the line-of-sight,

$$\Xi^{A,A'}(E, l, b) = \int_0^\infty \mathrm{d}s\; n^{A'}_{\mathrm{gas}}(\vec{x}) I^{A}_{\mathrm{CR}}(E, \vec{x}), \tag{6.4}$$

Where $I^{A}_{\mathrm{CR}}(E)$ is the CR intensity of nuclei with mass number A. The inten-

sity of nuclei is connected to their differential number density as $I^A_{\rm CR}(E) = c/(4\pi)n^A_{\rm CR}(E)$.We find in Ξ^{pp} the two prominent hot spots visible in Fig. 6.5: The extended region produced by CRs from Vela interacting with gas in the wall of the Local Bubble is absent in the IceCube HESE sample. The other, smaller one produced by CRs from the SNR G074.0-08.5 in the Cygnus Loop is close in position with the hottest spot in the IceCube neutrino data. As shown in figure 6.6, CRs propagate along a magnetic field line away from the Galactic plane until they reach a region of increased gas density close to the boundary of the Local Bubble where the interaction probability $\propto \Xi(E, l, b)$ has a maximum.

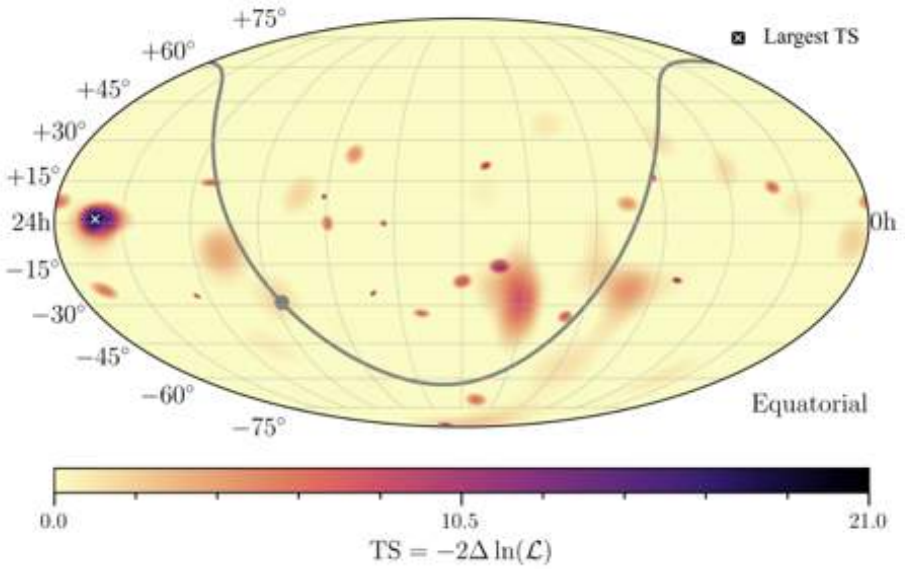

Figure 6.6: Point source TS map from Ref [10], Galactic center and galactic plane are indicated by grey dot and grey line. The most significant position is as $(\alpha, \delta) = (342.1°, 1.3°)$.

6.2.2 Neutrino intensity

We concentrate now on the neutrinos produced by CRs from SNR G074.0-08.5 in the Cygnus Loop. In this section, we report the results of our nu-

merical calculations which we compare in the appendix with analytical estimates. Because of the rather large uncertainty in the distance to this SNR, $d = (0.5-1)\,\mathrm{kpc}$, we consider two cases, choosing as the distance the average ($d = 0.75\,\mathrm{kpc}$) and the minimal value ($d = 0.5\,\mathrm{kpc}$) of this range, respectively. The intensity $I_\nu(E, l, b)$ of neutrinos with energy E emitted along the line-of-sight with direction (l, b) is given by

$$I_\nu(E, l, b) = \sum_{A,A'} \int_E^\infty \mathrm{d}E'\, \Xi^{A,A'}(E', l, b) \frac{\mathrm{d}\sigma^{AA'\to\nu}(E', E)}{\mathrm{d}E}. \qquad (6.5)$$

We include both for the target gas and the CRs the contribution of protons and helium nuclei, $A, A' = \{p, \mathrm{He}\}$. The neutrino production cross sections are evaluated with `AAfrag` [133]. In figure 6.7, we show the resulting neutrino intensity I_ν for the energy $E = 100\,\mathrm{TeV}$ in equatorial coordinates, i.e. as function of right ascension α and declination δ for $d = 0.5\,\mathrm{kpc}$. For the larger source distance, $d = 0.75\,\mathrm{kpc}$, the hot spot in the neutrino intensity shrinks slightly in size, while its position is nearly unchanged. The maximum of $I_\nu(E, \alpha, \delta)$ corresponds to $\simeq 400$ times the isotropic neutrino intensity measured by IceCube. In the case of the larger source distance, $d = 0.75\,\mathrm{kpc}$, the neutrino intensity is reduced by one third.

We note that the position of the hot spot is approximately determined by the intersection of the ellipsoid filled by CRs and the boundary of the Local Bubble. From Fig. 6.7, we see that the hot spot predicted by us is around 10°–15° offset against the most significant point in the search for point sources found by IceCube. Uncertainties in the direction of the magnetic field line connected to the Cygnus SNR lead to a variation in the position of the hot spot as shown in Fig. 6.8: In this figure, we show the projection of the magnetic field line passing through Cygnus (blue line)

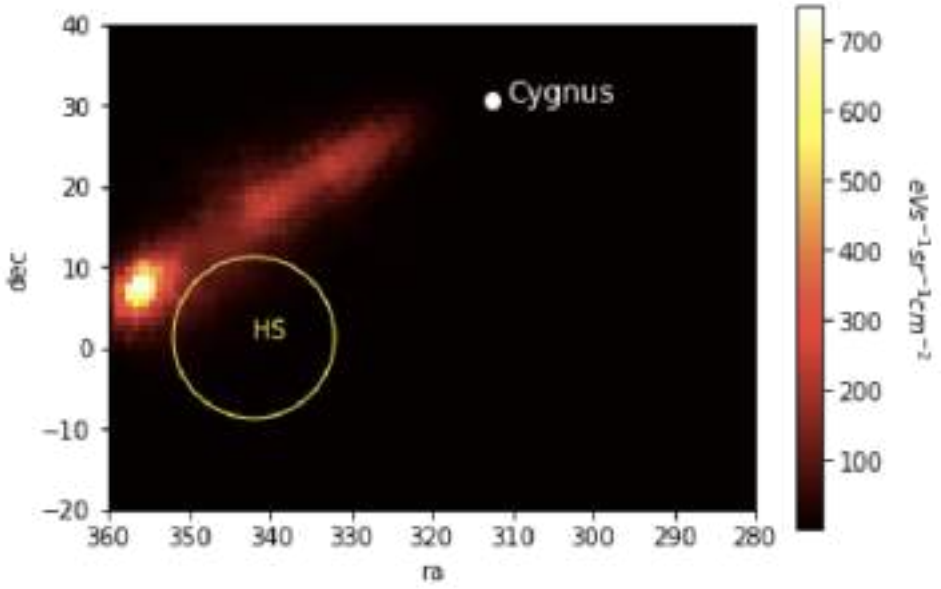

Figure 6.7: Neutrino intensity $E^2 I_\nu(E, \alpha, \delta)$ for $E = 100\,\mathrm{TeV}$ in equatorial coordinates; the star shows the most significant point in the IceCube search for point sources.

together with the position of IceCube hot spot varying its distance R as a red line. If this hot spot is created by the cosmic rays from the Cygnus SNR, its distance R has to be around 200 pc such that the IceCube hot spot is the closest to CR ellipsoid from Cygnus. From Fig. 6.8a, it is clear that a rather small rotation of $\simeq 5^\circ$ of the magnetic field line in the Galactic plane would be sufficient to align cosmic rays from the Cygnus loop SNR with the position of the Ice Cube hot spot. Note also that small changes in the position of the hot spot would not lead to large changes in the resulting neutrino intensity, because the gas density in the hot spot is not atypically large, $n_{\mathrm{gas}} \simeq 0.6/\mathrm{cm}^3$, compared to other, close parts of the boundary of the Local Bubble.

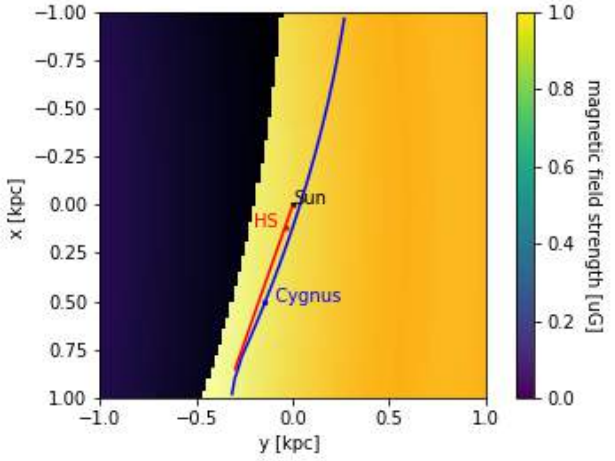

(a) XY projection

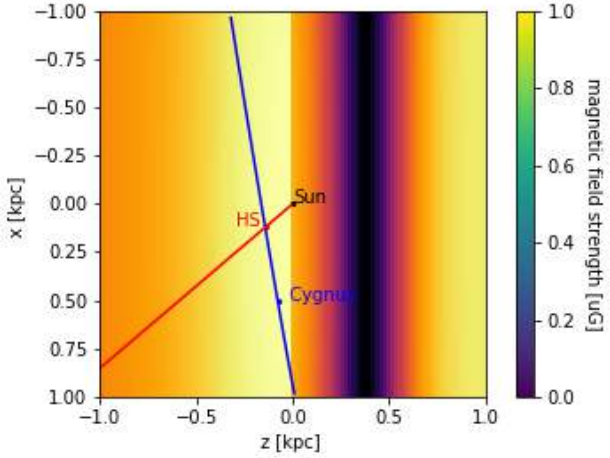

(b) XZ projection

Figure 6.8: Projection of the magnetic field line passing through the Cygnus loop SNR in blue, the position of the Sun position in black and the red line represent the position of the IceCube hot spot for varying R, the red point corresponds to the position of the IceCube hot spot for $R_{hs} = 194\,\mathrm{pc}$.

We define the equivalent isotropic intensity of a specific source as

$$\langle I_\nu(E)\rangle \equiv \frac{1}{4\pi}\int \mathrm{d}\Omega\, w(E) I_\nu(E,l,b) \tag{6.6}$$

With the weight $w(E)$ set to one. Since the observed neutrino intensity $I_\nu^{\mathrm{obs}}(E)$ is approximately isotropic, the ratio $I_\nu(E)/I_\nu^{\mathrm{obs}}(E)$ corresponds to the fraction of neutrino events with energy E from a given source observed by an experiment with uniform exposure. In Fig. 6.9, we show the isotropic neutrino intensity $\langle I_\nu(E)\rangle$ produced by CRs from the Cygnus Loop together with Ice Cube data from Ref. [7]. Note that the neutrino flux is dominated by the contribution from helium primaries which have a larger interaction probability and dominate above $E \simeq 10^{14}\,\mathrm{eV}$ the CR injection spectrum defined in section. 3.3. Additionally, we compare the intensity of photons to the sensitivity of the LHASSO experiment estimated in Ref. [168].

For a specific experiment like IceCube, we have to account for the declination dependence of the effective area $A_{\mathrm{eff}}(E,\delta)$. For the HESE data set, we use the the effective area $A_{\mathrm{eff}}(E)$ from Ref. [10] and deduce the declination dependence We subtract in the Supplemental Fig. 5 of Ref. [10] the line signal+background from the background to obtain the signal $S(\delta)$ as function of the declination δ. Then we calculate with $x = \sin\delta$

$$S_{\mathrm{av}} = \frac{1}{2}\int_{-1}^{1} \mathrm{d}x\, S(\delta). \tag{6.7}$$

The weight w of a source with declination δ follows then as $w = S(\delta)/S_{\mathrm{av}}$.

Since the extension of the hot spot is small, we can neglect the declination dependence of the weight, setting $w = A_{\mathrm{eff}}(E,\delta_s)/A_{\mathrm{eff}}(E) \simeq 1$ with $\delta \simeq 0^\circ$ for the hot spot of IceCube.

We estimate the number of expected neutrino events above the minimal

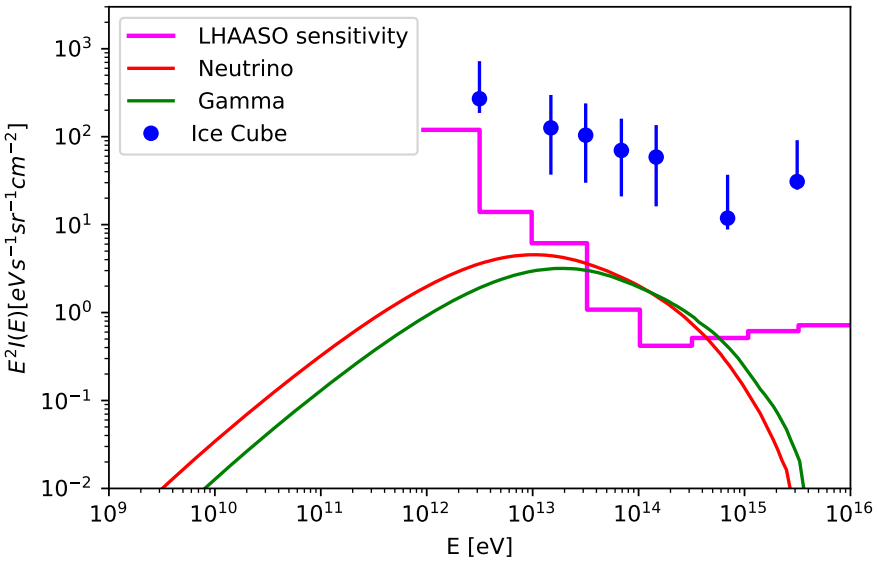

Figure 6.9: Equivalent isotropic intensity of a neutrinos and photons produced by CRs from the Cygnus Loop are compared to IceCube data [7] and the estimated sensitivity of the LHASSO experiment [168].

energy E_0 as

$$N_\nu(E > E_0) = wT \int_{E_0}^{\infty} dE \int \mathrm{d}\Omega A_{\mathrm{eff}}(E) I_\nu(E, l, b), \tag{6.8}$$

Where T is the observation time. With $E_0 = 60\,\mathrm{TeV}$, we find that the hot spot produced by CRs from the Cygnus loop corresponds to two neutrino events, while four neutrino events in the HESE (event ID 44, 67, 74 with corresponding energies of 84.6 TeV, 165 TeV, 71.3 TeV respectively, and event 105) may be associated with hot spot found in the IceCube analysis.

6.2.3 Discussion

Before we conclude, we recall that we obtained combining the gas and CR maps a second hot spot produced by CRs from Vela. Although more promi-

nent, the corresponding neutrino signal is absent in the IceCube HESE sample. The simplest explanation for its absence is that Vela is not a PeVatron: A low value of the maximal acceleration energy $E_{\rm max}$ would reduce the number of CRs which can reach the high density regions close to the boundary of the Local Bubble. Moreover, the production of neutrinos is strongly suppressed above $E_{\rm max}/20$, this senario will affect also the cosmic rays spectrum received at higher energies. Alternatively, our magnetic field model fails close to the Local Bubble: CRs may be spread over a larger solid angle, if the ratio of the turbulent to regular field strength is larger, or the local field lines deviate from the direction in the Jansson-Farrar model. In this case Vela may still dominate CRs flux, but instead of producing a hotspot in the neutrino sky map it will induce a contribution spread on a much larger volume that will be consistent with IceCube data.

Third, we comment on the prospects for the detection of gamma-rays which are produced in association with neutrinos in the hot spot. Since the predicted gamma-ray emission from the hot spot is not point-like but rather extended, its detection is challenging and depends strongly on the rejection capability of hadron in the considered gamma-ray experiment. HAWC can detect a diffuse gamma-ray flux on a level comparable to the over-all diffuse neutrino flux measured by IceCube shown, but is not sensitive enough to detect the expected gamma-ray flux from the hot spot shown in Fig. 6.9. In contrast, the more sensitive LHAASO experiment [55] should be able to detect the photon flux from the hot spot in the energy range $E \sim 100\,\mathrm{TeV}$ within few years.

Finally, let us comment on the recent detection of 0.1–1 PeV diffuse gamma-rays reported by the Tibet ASgamma collaboration [36]. In their event sample, all gamma rays with energies above 398 TeV were separated

by more than 0.5° from known TeV sources. In the scenario of anisotropic CR diffusion discussed here, such a separation arises rather naturally. This measurement combined with Fermi LAT data at TeV energies indicate also that the photon flux in the outer Galaxy is rather hard, $1/E^{2.5}$ [147].

Summary :

We studied the secondary production of PeV CRs from Vela interaction in the bubble walls. We assumed density matter in the Local bubble walls ~ 10 times higher than the interstellar one we obtained a neutrino flux compatible with IceCube spectrum. The gamma rays flux which might explain Fermi LAT the γ-ray excess suggested in Ref. [167].

Then we studied other potential local neutrino sources. We selected young sources $\lesssim 30\,\mathrm{kyr}$ and in the vicinity of the sun $\lesssim 1\,\mathrm{kpc}$ and propagated cosmic rays following an anisotropic diffusion. We used a recent dust map from [157] to model matter distribution. We found that CRs from Cygnus Loop source interacting with gas close to the boundary of the Local Bubble lead to a hot spot in the neutrino flux close to the most significant point in the IceCube search for point sources. The computed neutrino intensity estimated from Cygnus Loop contribution corresponds to two events with energy above 60 TeV. The γ-rays counterpart fluxes should be detectable by LHASSO within few years, providing a clear signature for a Galactic origin of the hot spot in the neutrino flux observed by IceCube.

Chapter 7

Conclusion and discussion

Conclusion : In this thesis, we conducted a multi-messenger study of local sources with PeV cosmic rays (around the *knee*) and *multi* TeV neutrinos and γ-rays in an anisotropic diffusion model taking into account the effect of the Local Bubble and using the most recent dust map.

In the standard diffusion picture it is assumed that Galactic CRs form a smooth, stationary "sea" around the Galactic disk. Evidence for this assumption comes from GeV γ-ray observations, which indicate a rather small variation of the parent CR populations below $\approx 100\,\mathrm{GeV}$ throughout the Galaxy outside of several kpc from the Galactic center [27]. Going to higher energies, CRs escape faster and thus the number of CR sources contributing to the local flux diminishes. In order to match the required diffusion coefficient with micro-gauss magnetic fields observed in the local Galaxy the CR propagation should be strongly anisotropic [108]. Then the number of CR sources decreases by a factor 100 relative to the case of isotropic diffusion. As a result, the CR flux should be dominated by few local CR sources except for the lowest energies.

In the first part of this thesis, we have examined the suggestion put

forward in Refs. [94, 93] that the spectrum below the knee is dominated by CRs accelerated in the Vela SNR and that the knee corresponds to the maximal energy of this source. As an important improvement compared to these earlier studies, we have taken into account that the Sun is located inside the Local Bubble and that CRs propagate anisotropically. Without the influence of the Local Bubble, the CR flux from Vela at the position of the Sun would overshot the observed one by 3 order of magnitude, because the Sun and Vela are connected by field lines of the regular magnetic field. We have obtained a good description of the flux of individual groups of CR nuclei both in the knee region and above. Adding additionally the CR flux from the 2–3 Myr old source suggested in Ref. [134, 135], the CR spectra in the whole energy range between 200 GV and the transition to extragalactic CRs are described well combining the fluxes from only these two Galactic sources.

We stress that, while including the effect of the Local Bubble is an important improvement, the uncertainties connected to the strength and shape of the magnetic field in the bubble are large. We studied in depth the dependence of the spectrum and amplitude of the CR flux from Vela received on Earth on the parameters and the geometry of the Local Bubble.
In a second part of this thesis, we presented a model which explains the high diffuse neutrino flux measured by IceCube at $E < 100$ TeV by CR interactions in the walls of the Local Bubble from Vela SNR cosmic rays.

The strong magnetic field in the wall of the LB serves as a magnetic shield for CRs from such sources and trap cosmic rays. At the same time, the gas density is ~ 10 times higher in the wall compared to the interstellar one. Both factors lead to a significant neutrino and gamma-ray flux produced in the bubble walls. Combining this Galactic component with a standard $1/E^{2.1}$

extragalactic neutrino flux describes well the IceCube neutrino spectrum. The accompanying photon flux may be responsible for the TeV gamma-ray excess found recently in Ref. [167].

In the last project we extended our study to other local sources and we used the most recent dust map from Leike et al. [157] to model the CRs target for neutrinos and γ-rays production. We observed that CRs from the SNR G074.0-08.5 in the Cygnus Loop interacting with gas close to the boundary of the Local Bubble lead to a hot spot in the neutrino flux. The position of this hot spot is compatible with the most significant point in the IceCube search for point sources, and the neutrino intensity estimated by us corresponds to two events with energy above 60 TeV. The corresponding photon fluxes should be detectable by LHASSO within few years, providing a clear signature for a Galactic origin of the hot spot in the neutrino flux observed by IceCube.

Outlooks : A first step would be to find a set of parameters that allow to concile the dominent CRs source with and IceCube neutrino maps for Vela. In a more general point of view, a natural continuation of the work done would be to apply the same analysis to larger scales. In addition to extinction, other ISM surveys construct large scale maps deduced from CO observation [84] and 21 cm hydrogen line [141], for instance and all sky Leiden/Argentine/Bonn (LAB) Survey of Galactic H $_{\mathrm{I}}$ reconstructed a 3d map of matter distribution on galactic scales [140]. We then inject cosmic rays from a population of sources following the supernova distribution in the Galaxy, and propagate particle according to the diffusion properties of GMF. We study the interaction product of cosmic rays with ISM and compute secondary production of neutrinos and gamma rays. Then we could construct a model based on both galactic and local contribution. It would

be interesting to compare different GMF models and the ratio between the regular and turbulent magnetic field.
By including Local Bubble we showed how local magnetic features may affect the cosmic rays flux received on Earth. It would be interesting to consider a more realistic local magnetic field geometry by including like the loop I that is connected to the Local Bubble forming a dense and thick wall. Dust maps can be used to probe these features, Lallement et al. [154] already used a dust map to study the geometry of the Local Bubble.

Summary : This thesis sheds the light on local source's contribution to CRs, neutrinos and γ-rays fluxes, and on the effect of the Local Bubble. We can summarise our contribution as follows :

- We showed that in anisotropic diffusion, a single local source provides a cosmic rays flux that dominates the spectrum around the *knee*;
- We studied the role played by the Local Bubble in CRs propagation and in secondaries production;
- We studied the contribution of local sources to neutrino flux, and observed a production of neutrinos from Cygnus loop CRs consistent with the brightest region in IceCube map;
- We predicted a γ-ray flux that should be detectable within few years by LHAASO.

This work leads to further exploration of local sources and can be completed by studying more deeply the local environment and by considering a large scale multi-messenger study.

Appendix A

Comparison with analytical estimates

A.1 Cosmic ray density

For our analytical estimates, we assume that the Cygnus Loop SNR (G074.0-08.5) injected instantaneously $6 \times 10^{50}\,\mathrm{erg}$ in CRs, following a power law with $Q(E) = Q_0(E/E_0)^{-\alpha}$ and $\alpha \simeq 2.2$ for the injection spectrum. To be definite, we split the total energy between protons and helium nuclei as 4:3. Choosing the lowest injection energy of protons as the normalization energy, $E_0 = 1\,\mathrm{GeV}$, it follows then $Q_p = E_p/(5E_0^2) \simeq 4.3 \times 10^{52}/\mathrm{GeV}$. Similarly, it follows $Q_{\mathrm{He}} = 4E_{\mathrm{He}}/(15E_0^2) \simeq Q_p$ for the normalization of the helium flux above the minimal injection energy $4\,\mathrm{GeV}$.

The diffusion approximation can be applied once CRs have reached distances from the source that are greater than a few times the coherence length of the turbulent magnetic field [109, 110], which is around $L_{\mathrm{coh}} \approx 10\,\mathrm{pc}$ close to the disk. At a given energy, the functional behavior of the observed CR flux from a single source at the distance L and with the age τ can be di-

vided into three regimes: For $2D\tau \ll L^2$, the diffuse flux is exponentially suppressed, while for intermediate times it is given by

$$I(E) \simeq \frac{c}{4\pi}\frac{Q(E)}{V(t)}. \tag{A.1}$$

Here, $V(t) = 4\pi\, L_\perp^2 L_\parallel/3$ is the volume of the ellipsoid with major axis $L_\parallel = (2D_\parallel t)^{1/2}$ and minor axis $L_\perp = (2D_\perp t)^{1/2}$, When the diffusion front reaches the edge of the Galactic CR halo, CRs start to escape and the slope of the CR intensity steepens.

For the numerical values of the diffusion coefficients in the case of anisotropic diffusion, we read from Fig. 4 from Ref. [108] with $\eta = 0.25$ and $D_{\rm iso} \simeq 1 \times 10^{30}{\rm cm}^2/{\rm s}$ valid at the reference energy $E_* = 10^{14}\,{\rm eV}$ that $D_\parallel \simeq 5D_{\rm iso}$, while $D_\perp \simeq D_{\rm iso}/500$. Hence CRs with energy E_* fill an ellipsoid with major axis $L_\parallel \simeq 700\,{\rm pc}$ and minor axis $L_\perp \simeq 14\,{\rm pc}$. The CR intensity of protons inside this ellipsoid can be estimated with $V \simeq 1.7 \times 10^{61}{\rm cm}^3$ as $E_* I(E_*) \simeq 6 \times 10^{-6}/({\rm cm}^2\,{\rm s}\,{\rm sr})$.

In Fig. A.1, we show for comparison the cells satisfying the condition $I(E) > 0.01 I_{\rm max}(E)$ at $E = 10^{14}\,{\rm eV}$ in our numerical simulations together with the position of the hot spot and of the Cygnus Loop SNR. One can see that the CRs fill a tube with diameter 50 pc, what agrees quite well with the expectation $\sim 6 \times 2D_\perp\tau \simeq 80\,{\rm pc}$ for $I(E) = 0.01 I_{\rm max}(E)$. Moreover, the distance between the hot spot and the Cygnus Loop SNR is around 630 pc and the CR tube extends until it touches the Local Bubble. Note also this diameter is much larger than the extension of a SNR at the age of few hundred years; thus our assumption of a point-like injection is justified.

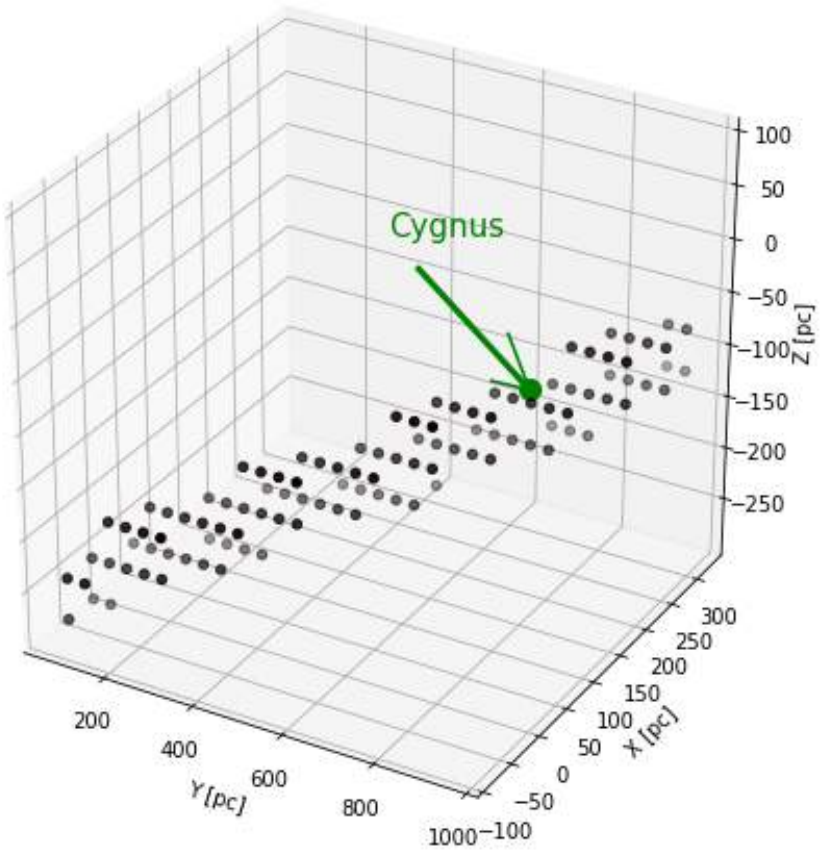

Figure A.1: Volume satisfying $I > 0.01 I_{\max}$ at the proton energy $E = 10^{14}$ eV together with the position of the hot spot and the Cygnus Loop SNR.

A.2 Neutrino production

In order to obtain an estimate for the equivalent isotropic neutrino intensity, we define first the volume $\mathcal{V}$ of the neutrino emitting region by the condition

$$n_{\rm gas}(\vec{x}) I_{\rm CR}(E_*, \vec{x}) > 0.01 \max_{\vec{x}\in{\rm box}} \{n_{\rm gas}(\vec{x}) I_{\rm CR}(E_*, \vec{x})\} \tag{A.2}$$

at a given energy E_*. Then we introduce in

$$I_\nu(E) = \frac{c}{4\pi} \sum_{A,A'\in\{1,4\}} \int_E^\infty {\rm d}E' \, \frac{{\rm d}\sigma_{\rm inel}^{AA'\to\nu}(E', E)}{{\rm d}E} \times \int {\rm d}^3x \, \frac{n_A(E', \vec{x}) n_{\rm gas}^{A'}(\vec{x})}{4\pi d^2} \,, \tag{A.3}$$

the inelastic cross section $\sigma_{\rm inel}^{AA'}$, the spectrally averaged energy fraction $\left\langle y^{\alpha-1} \right\rangle$ transferred to neutrinos, and the total number of gas particles $N_{\rm gas} = \sum_A \int_{\mathcal{V}} {\rm d}^3x \, n_{\rm gas}^A(\vec{x})$ in the source region $\mathcal{V}$. Moreover, we neglect the extension of the source region, obtaining

$$I_\nu(E) \simeq \sum_{A,A'} \frac{f_{A'} N_{\rm gas}}{4\pi d^2} \left\langle y^{\alpha-1} \right\rangle \sigma_{\rm inel}^{AA'\to\nu}(E) \langle I_A(E) \rangle, \tag{A.4}$$

where d denotes the distance to the source volume $\mathcal{V}$, f_A the fraction of proton and helium nuclei in the gas, and $\langle I_A(E') \rangle$ the spatially averaged intensity of CR protons and helium nuclei.

At the energy $E_* = 10^{14}\,{\rm eV}$, the condition (A.2) is satisfied in 750 cells of size $(6\,{\rm pc})^3$, resulting with $\langle n_{\rm gas} \rangle \simeq 0.56/{\rm cm}^3$ into $N_{\rm gas} \simeq 2 \times 10^{60}$. The intensity of CR protons obtained from our numerical simulations and averaged over this volume is $\langle E_* I_p(E_*) \rangle \simeq 4 \times 10^{-6}/{\rm cm}^2/{\rm s}/{\rm sr}$, i.e. agrees well with our estimate using the diffusion approximation in the previous subsection.

With $d \simeq 270\,{\rm pc}$ and $Z(E_*, \alpha) = \left\langle y^{\alpha-1} \right\rangle \sigma_{\rm inel}^{pp} \simeq 7\,{\rm mbarn}$ for the Z factor

for the production of neutrinos from a power law with $\alpha \simeq 2.2$, this leads to

$$E_*^2 I_\nu^{pp}(E_*) \simeq 1.0 \frac{\mathrm{eV}}{\mathrm{cm}^2\,\mathrm{s}\,\mathrm{sr}}$$

for the isotropic neutrino intensity due to pp interactions. We can estimate the contribution of helium projectiles and targets at energies $E_\nu \lesssim 10^{13}\,\mathrm{eV}$ setting $I_p(E) \simeq I_{\mathrm{He}}(E)$ valid for primary energies $\lesssim 10^{14}\,\mathrm{eV}$. With $\sigma_{\mathrm{inel}}^{pp} \simeq 48\,\mathrm{mbarn}$, $\sigma_{\mathrm{inel}}^{p\mathrm{He}} \simeq 148\,\mathrm{mbarn}$, $\sigma_{\mathrm{inel}}^{\mathrm{He}p} \simeq 137\,\mathrm{mbarn}$ and $\sigma_{\mathrm{inel}}^{\mathrm{He}\,\mathrm{He}} \simeq 324\,\mathrm{mbarn}$, it follows then

$$\frac{I_\nu^{\mathrm{tot}}}{I_\nu^{\mathrm{pp}}} \simeq \frac{0.9(\sigma_{\mathrm{inel}}^{pp} + \sigma_{\mathrm{inel}}^{\mathrm{He}p}) + 0.1(\sigma_{\mathrm{inel}}^{\mathrm{He}p} + \sigma_{\mathrm{inel}}^{\mathrm{He}\,\mathrm{He}})}{\sigma_{pp}} \simeq 4. \tag{A.5}$$

Thus our estimate agrees again well the numerical value shown in Fig. 6.9.

Bibliography

[1] A. Aab, P. Abreu, M. Aglietta, I. F. M. Albuquerque, J. M. Albury, I. Allekotte, A. Almela, J. A. Castillo, J. Alvarez-Muniz, G. A. Anastasi, and et al. Large-scale cosmic-ray anisotropies above 4 eev measured by the pierre auger observatory. *The Astrophysical Journal*, 868(1):4, Nov 2018.

[2] A. Aab, P. Abreu, M. Aglietta, J. M. Albury, I. Allekotte, A. Almela, J. A. Castillo, J. Alvarez-Muniz, R. Alves Batista, G. A. Anastasi, et al. Measurement of the cosmic-ray energy spectrum above 2.5×10^{18} ev using the pierre auger observatory. *Physical Review D*, 102(6), Sep 2020.

[3] M. Aartsen, M. Ackermann, J. Adams, J. Aguilar, M. Ahlers, M. Ahrens, C. Alispach, K. Andeen, T. Anderson, I. Ansseau, and et al. Characteristics of the diffuse astrophysical electron and tau neutrino flux with six years of icecube high energy cascade data. *Physical Review Letters*, 125(12), Sep 2020.

[4] M. Aartsen, M. Ackermann, J. Adams, J. Aguilar, M. Ahlers, M. Ahrens, D. Altmann, K. Andeen, T. Anderson, I. Ansseau, and et al. Astrophysical neutrinos and cosmic rays observed by icecube. *Advances in Space Research*, 62(10):2902–2930, Nov 2018.

[5] M. Aartsen, M. Ackermann, J. Adams, J. A. Aguilar, M. Ahlers, M. Ahrens, I. Al Samarai, D. Altmann, K. Andeen, and et al. Multi-messenger observations of a flaring blazar coincident with high-energy neutrino icecube-170922a. *Science*, 361(6398):eaat1378, Jul 2018.

[6] M. G. Aartsen, K. Abraham, M. Ackermann, J. Adams, J. A. Aguilar, M. Ahlers, M. Ahrens, D. Altmann, T. Anderson, I. Ansseau, and et al. Anisotropy in cosmic-ray arrival directions in the southern hemisphere based on six years of data from the icecube detector. *The Astrophysical Journal*, 826(2):220, Aug 2016.

[7] M. G. Aartsen, M. Ackermann, J. Adams, J. A. Aguilar, M. Ahlers, M. Ahrens, I. A. Samarai, D. Altmann, K. Andeen, T. Anderson, and et al. Constraints on galactic neutrino emission with seven years of icecube data. *The Astrophysical Journal*, 849(1):67, Oct 2017.

[8] M. G. Aartsen et al. Neutrino astronomy with the next generation icecube neutrino observatory, 2019.

[9] R. Abbasi, M. Abe, T. Abu-Zayyad, M. Allen, R. Azuma, E. Barcikowski, J. Belz, D. Bergman, S. Blake, R. Cady, and et al. The energy spectrum of cosmic rays above 1017.2 ev measured by the fluorescence detectors of the telescope array experiment in seven years. *Astroparticle Physics*, 80:131–140, Jul 2016.

[10] R. Abbasi, M. Ackermann, J. Adams, J. Aguilar, M. Ahlers, M. Ahrens, C. Alispach, A. Alves, N. Amin, K. Andeen, and et al. Icecube high-energy starting event sample: Description and flux characterization with 7.5 years of data. *Physical Review D*, 104(2), Jul 2021.

[11] R. U. Abbasi, M. Abe, T. Abu-Zayyad, M. Allen, Y. Arai, E. Barcikowski, J. W. Belz, D. R. Bergman, S. A. Blake, R. Cady, and et al. The cosmic-ray composition between 2 pev and 2 eev observed with the tale detector in monocular mode. *The Astrophysical Journal*, 909(2):178, Mar 2021.

[12] R. U. Abbasi, M. Abe, T. Abu-Zayyad, M. Allen, R. Azuma, E. Barcikowski, J. W. Belz, D. R. Bergman, S. A. Blake, R. Cady, and et al. The cosmic ray energy spectrum between 2 pev and 2 eev observed with the tale detector in monocular mode. *The Astrophysical Journal*, 865(1):74, Sep 2018.

[13] A. U. Abeysekara, R. Alfaro, C. Alvarez, R. Arceo, J. C. Arteaga-Velázquez, D. A. Rojas, E. Belmont-Moreno, S. Y. BenZvi, C. Brisbois, T. Capistrán, and et al. All-sky measurement of the anisotropy of cosmic rays at 10 tev and mapping of the local interstellar magnetic field. *The Astrophysical Journal*, 871(1):96, Jan 2019.

[14] A. U. Abeysekara, R. Alfaro, C. Alvarez, J. D. Álvarez, R. Arceo, J. C. Arteaga-Velázquez, D. A. Rojas, H. A. A. Solares, A. Becerril, E. Belmont-Moreno, and et al. Observation of anisotropy of tev cosmic rays with two years of hawc. *The Astrophysical Journal*, 865(1):57, Sep 2018.

[15] A. Abramowski, F. Aharonian, F. Ait Benkhali, A. G. Akhperjanian, E. O. Angüner, M. Backes, S. Balenderan, A. Balzer, A. Barnacka, and et al. H.e.s.s. reveals a lack of tev emission from the supernova remnant puppis a. *Astronomy & Astrophysics*, 575:A81, Feb 2015.

[16] F. Acero, M. Ackermann, M. Ajello, A. Albert, L. Baldini, J. Ballet,

G. Barbiellini, D. Bastieri, R. Bellazzini, E. Bissaldi, and et al. Development of the model of galactic interstellar emission for standard point-source analysis of fermi large area telescope data. *The Astrophysical Journal Supplement Series*, 223(2):26, Apr 2016.

[17] M. Ackermann, M. Ajello, A. Albert, W. B. Atwood, L. Baldini, J. Ballet, G. Barbiellini, D. Bastieri, K. Bechtol, R. Bellazzini, and et al. The spectrum of isotropic diffuse gamma-ray emission between 100 mev and 820 gev. *The Astrophysical Journal*, 799(1):86, Jan 2015.

[18] M. Ackermann, M. Ajello, W. B. Atwood, L. Baldini, J. Ballet, G. Barbiellini, D. Bastieri, K. Bechtol, R. Bellazzini, B. Berenji, and et al. Fermi-lat observations of the diffuse γ-ray emission: Implications for cosmic rays and the interstellar medium. *The Astrophysical Journal*, 750(1):3, Apr 2012.

[19] P. A. R. Ade, N. Aghanim, D. Alina, M. I. R. Alves, C. Armitage-Caplan, M. Arnaud, D. Arzoumanian, M. Ashdown, F. Atrio-Barandela, and et al. Planckintermediate results. xix. an overview of the polarized thermal emission from galactic dust. *Astronomy & Astrophysics*, 576:A104, Apr 2015.

[20] O. Adriani et al. Pamela measurements of cosmic-ray proton and helium spectra. *Science*, 332(6025):69–72, 2011.

[21] N. Aghanim, Y. Akrami, F. Arroja, M. Ashdown, J. Aumont, C. Baccigalupi, M. Ballardini, A. J. Banday, R. B. Barreiro, and et al. Planck2018 results. *Astronomy & Astrophysics*, 641:A1, Sep 2020.

[22] M. Aguilar et al. Precision measurement of the helium flux in primary cosmic rays of rigidities 1.9 gv to 3 tv with the alpha mag-

netic spectrometer on the international space station. *Phys. Rev. Lett.*, 115:211101, Nov 2015.

[23] M. Aguilar et al. Precision measurement of the proton flux in primary cosmic rays from rigidity 1 gv to 1.8 tv with the alpha magnetic spectrometer on the international space station. *Phys. Rev. Lett.*, 114:171103, Apr 2015.

[24] M. Aguilar et al. Precision measurement of the boron to carbon flux ratio in cosmic rays from 1.9 gv to 2.6 tv with the alpha magnetic spectrometer on the international space station. *Phys. Rev. Lett.*, 117:231102, Nov 2016.

[25] M. Aguilar et al. Observation of the identical rigidity dependence of he, c, and o cosmic rays at high rigidities by the alpha magnetic spectrometer on the international space station. *Phys. Rev. Lett.*, 119:251101, Dec 2017.

[26] F. Aharonian, A. G. Akhperjanian, A. R. Bazer-Bachi, M. Beilicke, W. Benbow, D. Berge, K. Bernlöhr, C. Boisson, O. Bolz, V. Borrel, and et al. Detection of tev γ-ray emission from the shell-type supernova remnant rx j0852.0-4622 with hess. *Astronomy & Astrophysics*, 437(1):L7–L10, Jun 2005.

[27] F. Aharonian, G. Peron, R. Yang, S. Casanova, and R. Zanin. Probing the "Sea" of Galactic Cosmic Rays with Fermi-LAT. 2018.

[28] M. Ahlers and F. Halzen. IceCube: Neutrinos and multimessenger astronomy. *Progress of Theoretical and Experimental Physics*, 2017(12), 11 2017. 12A105.

[29] M. Ahlers and F. Halzen. Opening a new window onto the universe with icecube. *Progress in Particle and Nuclear Physics*, 102:73–88, Sep 2018.

[30] S. E. M. Ahmed Maouloud, G. De Wasseige, M. Ahlers, M. Bustamante, and V. Van Elewyck. Observing GeV Neutrino Transients in the Multi-Messenger Era. *PoS*, ICRC2019:1023, 2021.

[31] H. Ahn, P. Allison, M. Bagliesi, J. Beatty, G. Bigongiari, P. Boyle, T. Brandt, J. Childers, N. Conklin, S. Coutu, and et al. Measurements of cosmic-ray secondary nuclei at high energies with the first flight of the cream balloon-borne experiment. *Astroparticle Physics*, 30(3):133–141, Oct 2008.

[32] H. S. Ahn, P. Allison, M. G. Bagliesi, J. J. Beatty, G. Bigongiari, J. T. Childers, N. B. Conklin, S. Coutu, M. A. DuVernois, O. Ganel, and et al. Discrepant hardening observed in cosmic-ray elemental spectra. *The Astrophysical Journal*, 714(1):L89–L93, Apr 2010.

[33] R. Alfaro et al. All-particle cosmic ray energy spectrum measured by the HAWC experiment from 10 to 500 TeV. *Phys. Rev.*, D96(12):122001, 2017.

[34] D. Allard. High energy astrophysics, 2016.

[35] M. Amenomori, S. Ayabe, S. W. Cui, Danzengluobu, L. K. Ding, X. H. Ding, C. F. Feng, Z. Y. Feng, X. Y. Gao, Q. X. Geng, and et al. Large-scale sidereal anisotropy of galactic cosmic-ray intensity observed by the tibet air shower array. *The Astrophysical Journal*, 626(1):L29–L32, May 2005.

[36] M. Amenomori, Y. Bao, X. Bi, D. Chen, T. Chen, W. Chen, X. Chen, Y. Chen, Cirennima, S. Cui, and et al. First detection of sub-pev diffuse gamma rays from the galactic disk: Evidence for ubiquitous galactic cosmic rays beyond pev energies. *Physical Review Letters*, 126(14), Apr 2021.

[37] M. Amenomori, X. J. Bi, D. Chen, T. L. Chen, W. Y. Chen, S. W. Cui, Danzengluobu, L. K. Ding, C. F. Feng, Z. Feng, and et al. Northern sky galactic cosmic ray anisotropy between 10 and 1000 tev with the tibet air shower array. *The Astrophysical Journal*, 836(2):153, Feb 2017.

[38] M. Amenomori et al. Measurement of air shower cores to study the cosmic ray composition in the knee energy region. *Phys. Rev. D*, 62:072007, Sep 2000.

[39] M. Amenomori et al. Cosmic-ray energy spectrum around the knee obtained by the tibet experiment and future prospects. *Advances in Space Research*, 47(4):629–639, 2011.

[40] Q. An et al. Measurement of the cosmic ray proton spectrum from 40 gev to 100 tev with the dampe satellite. *Science Advances*, 5(9):eaax3793, 2019.

[41] K. J. Andersen, M. Kachelrieß, and D. V. Semikoz. High-energy Neutrinos from Galactic Superbubbles. *Astrophys. J.*, 861(2):L19, 2018.

[42] C. D. Anderson. The apparent existence of easily deflected positives. *Science*, 76:238–239, 1932.

[43] C. D. Anderson and S. H. Neddermeyer. Cloud chamber observations of cosmic rays at 4300 meters elevation and near sea-level. *Phys. Rev.*, 50:263–271, Aug 1936.

[44] B.-G. Andersson and S. B. Potter. The magnetic field strength in the wall of the local bubble towardl,b$\approx 300°, 0°$. *The Astrophysical Journal*, 640(1):L51–L54, feb 2006.

[45] T. Antoni, W. Apel, A. Badea, K. Bekk, A. Bercuci, J. Blümer, H. Bozdog, I. Brancus, A. Chilingarian, K. Daumiller, and et al. Kascade measurements of energy spectra for elemental groups of cosmic rays: Results and open problems. *Astroparticle Physics*, 24(1-2):1–25, Sep 2005.

[46] W. D. Apel, J. C. Arteaga-Velázquez, K. Bekk, M. Bertaina, J. Blümer, H. Bozdog, I. M. Brancus, P. Buchholz, E. Cantoni, A. Chiavassa, and et al. Kneelike structure in the spectrum of the heavy component of cosmic rays observed with kascade-grande. *Physical Review Letters*, 107(17), Oct 2011.

[47] W. D. Apel et al. KASCADE-Grande measurements of energy spectra for elemental groups of cosmic rays. *Astropart. Phys.*, 47:54–66, 2013.

[48] J. W. Armstrong, B. J. Rickett, and S. R. Spangler. Electron Density Power Spectrum in the Local Interstellar Medium. *apj*, 443:209, Apr. 1995.

[49] B. Aschenbach, R. Egger, and J. Trümper. Discovery of explosion fragments outside the Vela supernova remnant shock-wave boundary. *Nature* , 373(6515):587–590, Feb. 1995.

[50] E. Atkin, V. Bulatov, V. Dorokhov, N. Gorbunov, S. Filippov, V. Grebenyuk, D. Karmanov, I. Kovalev, I. Kudryashov, A. Kurganov, and et al. First results of the cosmic ray nucleon experiment. *Journal of Cosmology and Astroparticle Physics*, 2017(07):020–020, Jul 2017.

[51] E. Atkin, V. Bulatov, V. Dorokhov, N. Gorbunov, S. Filippov, V. Grebenyuk, D. Karmanov, I. Kovalev, I. Kudryashov, A. Kurganov, and et al. New universal cosmic-ray knee near a magnetic rigidity of 10 tv with the nucleon space observatory. *JETP Letters*, 108(1):5–12, Jun 2018.

[52] E. V. Atkin et al. Energy Spectra of Cosmic-Ray Protons and Nuclei Measured in the NUCLEON Experiment Using a New Method. *Astron. Rep.*, 63(1):66–78, 2019.

[53] P. Auger, R. Maze, and T. Grivet-Mayer. Grandes gerbes cosmiques atmosphériques contenant des corpuscules ultrapénétrants. *Compt. Rend. Hebd. Seances Acad. Sci.*, 206(23):1721–1723, 1938.

[54] W. Baade and F. Zwicky. Cosmic rays from super-novae. *Proceedings of the National Academy of Sciences*, 20(5):259–263, 1934.

[55] X. Bai et al. The large high altitude air shower observatory (lhaaso) science white paper, 2019.

[56] B. Bartoli et al. Light-component spectrum of the primary cosmic rays in the multi-tev region measured by the argo-ybj experiment. *Phys. Rev. D*, 85:092005, May 2012.

[57] B. Bartoli et al. ARGO-YBJ OBSERVATION OF THE LARGE-SCALE COSMIC RAY ANISOTROPY DURING THE SOLAR MINIMUM BETWEEN CYCLES 23 AND 24. *The Astrophysical Journal*, 809(1):90, aug 2015.

[58] R. Beck. test. *Ap& SS*, 2009.

[59] A. R. Bell. Turbulent amplification of magnetic field and diffusive shock

acceleration of cosmic rays. *Monthly Notices of the Royal Astronomical Society*, 353(2):550–558, 09 2004.

[60] A. R. Bell and S. G. Lucek. Cosmic ray acceleration to very high energy through the non-linear amplification by cosmic rays of the seed magnetic field. *Monthly Notices of the Royal Astronomical Society*, 321(3):433–438, 03 2001.

[61] J. Bellido. Depth of maximum of air-shower profiles at the Pierre Auger Observatory: Measurements above $10^{17.2}$ eV and Composition Implications. *PoS*, ICRC2017:506, 2018. [,40(2017)].

[62] N. Benitez, J. Maiz-Apellaniz, and M. Canelles. Evidence for nearby supernova explosions. *Phys. Rev. Lett.*, 88:081101, 2002.

[63] C. L. Bennett, D. Larson, J. L. Weiland, N. Jarosik, G. Hinshaw, N. Odegard, K. M. Smith, R. S. Hill, B. Gold, M. Halpern, E. Komatsu, M. R. Nolta, L. Page, D. N. Spergel, E. Wollack, J. Dunkley, A. Kogut, M. Limon, S. S. Meyer, G. S. Tucker, and E. L. Wright. Nine-year wilkinson microwave anisotropy probe (wmap) observations: Final maps and results. *The Astrophysical Journal Supplement Series*, 208(2):20, sep 2013.

[64] Benoît, A. et al. First detection of polarization of the submillimetre diffuse galactic dust emission by archeops. *A&A*, 424(2):571–582, 2004.

[65] S. F. Berezhnev et al. First results from the operation of the prototype Tunka-HiSCORE array. *Bull. Russ. Acad. Sci. Phys.*, 79(3):348–351, 2015. [Izv. Ross. Akad. Nauk Ser. Fiz.79,no.3,381(2015)].

[66] T. BERGMANN, R. ENGEL, D. HECK, N. KALMYKOV, S. OSTAPCHENKO, T. PIEROG, T. THOUW, and K. WERNER.

One-dimensional hybrid approach to extensive air shower simulation. *Astroparticle Physics*, 26(6):420–432, Jan 2007.

[67] P. Blackett and G. Occhialini. Some photographics of the tracks of penetrating radiation. *Proceedings of the Royal Society of London*, A139:699–722, 1933.

[68] W. Bothe and W. Kolhörster. Das Wesen der Höhenstrahlung. *Zeitschrift fur Physik*, 56(11-12):751–777, Nov. 1929.

[69] S. Bottinelli. Matter cycle in the interstellar medium (ism).

[70] D. Breitschwerdt and S. Komossa. Galactic fountains and galactic winds. *Astrophys. Space Sci.*, 272:3–13, 2000.

[71] D. Breitschwerdt, J. F. McKenzie, and H. J. Voelk. Galactic winds. I. Cosmic ray and wave-driven winds from the galaxy. *Astron. Astrophys.* , 245:79, May 1991.

[72] L. F. Burlaga, V. Florinski, and N. F. Ness. IN SITU OBSERVATIONS OF MAGNETIC TURBULENCE IN THE LOCAL INTERSTELLAR MEDIUM. *The Astrophysical Journal*, 804(2):L31, may 2015.

[73] J. n. Candia, S. Mollerach, and E. Roulet. Cosmic ray spectrum and anisotropies from the knee to the second knee. *Journal of Cosmology and Astroparticle Physics*, 2003(05):003–003, May 2003.

[74] P. A. Caraveo, A. D. Luca, R. P. Mignani, and G. F. Bignami. The distance to the vela pulsar gauged withHubble space TelescopeParallax observations. *The Astrophysical Journal*, 561(2):930–937, nov 2001.

[75] M. Cardillo, E. Amato, and P. Blasi. On the cosmic ray spectrum from

type ii supernovae expanding in their red giant presupernova wind. *Astroparticle Physics*, 69:1–10, Sep 2015.

[76] A. N. Cha, K. R. Sembach, and A. C. Danks. The distance to the vela supernova remnant. *The Astrophysical Journal*, 515(1):L25–L28, apr 1999.

[77] Chen, B. Q., Schultheis, M., Jiang, B. W., Gonzalez, O. A., Robin, A. C., Rejkuba, M., and Minniti, D. Three-dimensional interstellar extinction map toward the galactic bulge. *A&A*, 550:A42, 2013.

[78] A. Chiavassa et al. A study of the first harmonic of the large scale anisotropies with the KASCADE-Grande experiment. *PoS*, ICRC2015:281, 2016.

[79] A. collaboration. Ams-02 detector. `https://ams02.space/fr/node/30`, september 2021.

[80] F. Collaboration. Fermi gamma-ray space telescope. `https://www.nasa.gov/content/fermi/overview`, August 2020.

[81] T. A. collaboration. Telescope array. `http://www.telescopearray.org/index.php/about/telescope-array`, september 2021.

[82] T. H. Collaboration and T. I. Collaboration. Combined analysis of cosmic-ray anisotropy with icecube and hawc, 2017.

[83] T. P. A. Collaboration, A. Aab, et al. The pierre auger observatory: Contributions to the 34th international cosmic ray conference (icrc 2015), 2015.

[84] T. M. Dame, D. Hartmann, and P. Thaddeus. The milky way in molec-

ular clouds: A new complete co survey. *The Astrophysical Journal*, 547(2):792–813, Feb 2001.

[85] A. De Angelis and M. Pimenta. *Introduction to Particle and Astroparticle Physics: Multimessenger Astronomy and its Particle Physics Foundations*. Undergraduate Lecture Notes in Physics. Springer International Publishing, 2018.

[86] C. A. de Coulomb. *Troisième Mémoire sur l'Electricité et le Magnétiseme*. Chez Bachelier, 1785.

[87] G. de Nolfo, I. Moskalenko, W. Binns, E. Christian, A. Cummings, A. Davis, J. George, P. Hink, M. Israel, R. Leske, and et al. Observations of the li, be, and b isotopes and constraints on cosmic-ray propagation. *Advances in Space Research*, 38(7):1558–1564, Jan 2006.

[88] P. A. M. Dirac. The quantum theory of the electron. *Proceedings of the Royal Society of London,*, A117:610–624, 1928.

[89] P. A. M. Dirac. The quantum theory of the electron ii. *Proceedings of the Royal Society of London,*, A118:351–361, 1928.

[90] L. O. Drury and A. W. Strong. Power requirements for cosmic ray propagation models involving diffusive reacceleration; estimates and implications for the damping of interstellar turbulence. *Astronomy & Astrophysics*, 597:A117, Jan 2017.

[91] G. M. Dubner, A. J. Green, W. M. Goss, D. C.-J. Bock, and E. Giacani. Neutral hydrogen in the direction of the vela supernova remnant. *The Astronomical Journal*, 116(2):813–822, aug 1998.

[92] D. D. Dzhappuev et al. Search for astrophysical PeV gamma rays from point sources with Carpet-2. *EPJ Web Conf.*, 207:03004, 2019.

[93] A. Erlykin and A. Wolfendale. Models for the origin of the knee in the cosmic-ray spectrum. *Advances in Space Research*, 27(4):803–812, 2001.

[94] A. D. Erlykin and A. W. Wolfendale. A single source of cosmic rays in the range - eV. *Journal of Physics G: Nuclear and Particle Physics*, 23(8):979–989, aug 1997.

[95] C. Ertley. Studying the polarization of hard x-ray solar flares with the gamma ray polarimeter experiment (grape). 01 2014.

[96] C. Evoli, P. Blasi, G. Morlino, and R. Aloisio. Origin of the cosmic ray galactic halo driven by advected turbulence and self-generated waves. *Physical Review Letters*, 121(2), Jul 2018.

[97] Fauvet, L., Macías-Pérez, J. F., Aumont, J., Désert, F. X., Jaffe, T. R., Banday, A. J., Tristram, M., Waelkens, A. H., and Santos, D. Joint 3d modelling of the polarized galactic synchrotron and thermal dust foreground diffuse emission. *A&A*, 526:A145, 2011.

[98] F. Fenu. The cosmic ray energy spectrum measured using the Pierre Auger Observatory. pages 9–16, 2017. [PoSICRC2017,486(2018)].

[99] K. M. Ferrière. The interstellar environment of our galaxy. *Reviews of Modern Physics*, 73(4):1031–1066, Dec 2001.

[100] C. Fitoussi et al. Search for supernova-produced Fe-60 in a marine sediment. *Phys. Rev. Lett.*, 101:121101, 2008.

[101] C. Flynn, J. Holmberg, L. Portinari, B. Fuchs, and H. Jahreiss. On the mass-to-light ratio of the local galactic disc and the optical luminosity of the galaxy. *Monthly Notices of the Royal Astronomical Society*, 372(3):1149–1160, Nov 2006.

[102] D. R. Foight, T. Güver, F. Özel, and P. O. Slane. Probing x-ray absorption and optical extinction in the interstellar medium usingchandraobservations of supernova remnants. *The Astrophysical Journal*, 826(1):66, Jul 2016.

[103] Gaia Collaboration, A. G. A. Brown, et al. Gaia Data Release 1. Summary of the astrometric, photometric, and survey properties. *Astron. Astrophys.* , 595:A2, Nov. 2016.

[104] Gaia Collaboration, Katz, D., et al. Gaia data release 2 - mapping the milky way disc kinematics. *A&A*, 616:A11, 2018.

[105] T. K. Gaisser, F. Halzen, and T. Stanev. Particle astrophysics with high-energy neutrinos. *Phys. Rept.*, 258:173–236, 1995. [Erratum: Phys. Rept.271,355(1996)].

[106] T. K. Gaisser, T. Stanev, and S. Tilav. Cosmic ray energy spectrum from measurements of air showers, 2013.

[107] J. S. George, K. A. Lave, M. E. Wiedenbeck, W. R. Binns, A. C. Cummings, A. J. Davis, G. A. de Nolfo, P. L. Hink, M. H. Israel, R. A. Leske, R. A. Mewaldt, L. M. Scott, E. C. Stone, T. T. von Rosenvinge, and N. E. Yanasak. ELEMENTAL COMPOSITION AND ENERGY SPECTRA OF GALACTIC COSMIC RAYS DURING SOLAR CYCLE 23. *The Astrophysical Journal*, 698(2):1666–1681, jun 2009.

[108] G. Giacinti, M. Kachelriess, and D. Semikoz. Reconciling cosmic ray diffusion with galactic magnetic field models. *Journal of Cosmology and Astroparticle Physics*, 2018(07):051–051, Jul 2018.

[109] G. Giacinti, M. Kachelrieß, and D. V. Semikoz. Filamentary Diffusion of Cosmic Rays on Small Scales. *Phys. Rev. Lett.*, 108:261101, 2012.

[110] G. Giacinti, M. Kachelrieß, and D. V. Semikoz. Anisotropic Cosmic Ray Diffusion and its Implications for Gamma-Ray Astronomy. *Phys. Rev.*, D88(2):023010, 2013.

[111] G. Giacinti, M. Kachelriess, and D. V. Semikoz. Explaining the spectra of cosmic ray groups above the knee by escape from the galaxy. *Physical Review D*, 90(4), Aug 2014.

[112] G. Giacinti, M. Kachelriess, and D. V. Semikoz. Escape model for galactic cosmic rays and an early extragalactic transition. *Physical Review D*, 91(8), Apr 2015.

[113] G. Giacinti, M. Kachelrieß, D. V. Semikoz, and G. Sigl. Cosmic Ray Anisotropy as Signature for the Transition from Galactic to Extragalactic Cosmic Rays. *JCAP*, 1207:031, 2012.

[114] G. Giacinti and J. G. Kirk. Large-scale cosmic-ray anisotropy as a probe of interstellar turbulence. *The Astrophysical Journal*, 835(2):258, Feb 2017.

[115] R. C. Gilmore, P. Madau, J. R. Primack, R. S. Somerville, and F. Haardt. Gev gamma-ray attenuation and the high-redshift uv background. *Monthly Notices of the Royal Astronomical Society*, 399(4):1694–1708, Nov 2009.

[116] P. Girichidis, T. Naab, S. Walch, M. Hanasz, M.-M. M. Low, J. P. Ostriker, A. Gatto, T. Peters, R. Wünsch, S. C. O. Glover, and et al. Launching cosmic-ray-driven outflows from the magnetized interstellar medium. *The Astrophysical Journal*, 816(2):L19, Jan 2016.

[117] N. Gorbunov et al. Energy spectra of abundant cosmic-ray nuclei in the NUCLEON experiment. 2018.

[118] N. Gorbunov, V. Grebenyuk, D. Karmanov, I. Kovalev, I. Kudryashov, A. Kurganov, A. Panov, D. Podorozhny, S. Porokhovoy, L. Sveshnikova, A. Tkachenko, L. Tkachev, A. Turundaevskiy, O. Vasiliev, and A. Voronin. Energy spectra of abundant cosmic-ray nuclei in the nucleon experiment, 2018.

[119] V. Grebenyuk, D. Karmanov, I. Kovalev, I. Kudryashov, A. Kurganov, A. Panov, D. Podorozhny, A. Tkachenko, L. Tkachev, A. Turundaevskiy, and et al. Secondary cosmic rays in the nucleon space experiment. *Advances in Space Research*, 64(12):2559–2563, Dec 2019.

[120] J.-L. Han. The Large - scale magnetic field structure of our galaxy: Efficiently deduced from pulsar rotation measures. In *Magnetized Interstellar Medium Conference*, 2 2004.

[121] J. L. Han, R. N. Manchester, W. van Straten, and P. Demorest. Pulsar rotation measures and large-scale magnetic field reversals in the galactic disk. *The Astrophysical Journal Supplement Series*, 234(1):11, jan 2018.

[122] C. Heiles. 9286 STARS: AN AGGLOMERATION OF STELLAR POLARIZATION CATALOGS. *The Astronomical Journal*, 119(2):923–927, feb 2000.

[123] V. F. Hess. Über Beobachtungen der durchdringenden Strahlung bei sieben Freiballonfahrten. *Phys. Z.*, 13:1084–1091, 1912.

[124] A. M. Hillas. Can diffusive shock acceleration in supernova remnants account for high-energy galactic cosmic rays? *Journal of Physics G: Nuclear and Particle Physics*, 31(5):R95–R131, apr 2005.

[125] T. R. Jaffe. Practical modeling of large-scale galactic magnetic fields: Status and prospects. *Galaxies*, 7(2):52, Apr 2019.

[126] T. R. Jaffe, K. M. Ferrière, A. J. Banday, A. W. Strong, E. Orlando, J. F. Macías-Pérez, L. Fauvet, C. Combet, and E. Falgarone. Comparing polarized synchrotron and thermal dust emission in the Galactic plane. *Monthly Notices of the Royal Astronomical Society*, 431(1):683–694, 03 2013.

[127] R. Jansson and G. R. Farrar. A new model of the galactic magnetic field. *The Astrophysical Journal*, 757(1):14, Aug 2012.

[128] F. C. Jones. The dynamical halo and the variation of cosmic-ray at length with energy. *apj*, 229:747–752, Apr. 1979.

[129] M. Kachelriess. Lecture notes on high energy cosmic rays, 2008.

[130] M. Kachelriess. The rise and fall of top-down models as main uhecr sources, 2008.

[131] M. Kachelrieß, O. Kalashev, S. Ostapchenko, and D. V. Semikoz. Minimal model for extragalactic cosmic rays and neutrinos. *Phys. Rev.*, D96(8):083006, 2017.

[132] M. Kachelrieß, I. V. Moskalenko, and S. S. Ostapchenko. Nuclear enhancement of the photon yield in cosmic ray interactions. *Astrophys. J.*, 789:136, 2014.

[133] M. Kachelrieß, I. V. Moskalenko, and S. S. Ostapchenko. AAfrag: Interpolation routines for Monte Carlo results on secondary production in proton-proton, proton-nucleus and nucleus-nucleus interactions. 2019.

[134] M. Kachelrieß, A. Neronov, and D. V. Semikoz. Signatures of a two million year old supernova in the spectra of cosmic ray protons, antiprotons and positrons. *Phys. Rev. Lett.*, 115(18):181103, 2015.

[135] M. Kachelrieß, A. Neronov, and D. V. Semikoz. Cosmic ray signatures of a 2-3 Myr old local supernova. *Phys. Rev.*, D97(6):063011, 2018.

[136] M. Kachelrießand S. Ostapchenko. Neutrino yield from Galactic cosmic rays. *Phys. Rev.*, D90(8):083002, 2014.

[137] M. Kachelrieß and D. Semikoz. Cosmic ray models. *Progress in Particle and Nuclear Physics*, 109:103710, Nov 2019.

[138] M. Kachelrieß, P. Serpico, and M. Teshima. The galactic magnetic field as spectrograph for ultra-high energy cosmic rays. *Astroparticle Physics*, 26(6):378–386, 2007.

[139] E. Kafexhiu, F. Aharonian, A. M. Taylor, and G. S. Vila. Parametrization of gamma-ray production cross sections forppinteractions in a broad proton energy range from the kinematic threshold to pev energies. *Physical Review D*, 90(12), Dec 2014.

[140] P. M. W. Kalberla, W. B. Burton, D. Hartmann, E. M. Arnal, E. Bajaja, R. Morras, and W. G. L. Pöppel. The Leiden/Argentine/Bonn (LAB) Survey of Galactic HI. Final data release of the combined LDS and IAR surveys with improved stray-radiation corrections. *Astron. Astrophys.* , 440(2):775–782, Sept. 2005.

[141] P. M. W. Kalberla and J. Kerp. The Hi Distribution of the Milky Way. *Ann. Rev. Astron. Astrophys.* , 47(1):27–61, Sept. 2009.

[142] T. Kamae, N. Karlsson, T. Mizuno, T. Abe, and T. Koi. Parameterization of Gamma, e+/- and Neutrino Spectra Produced by p-p

Interaction in Astronomical Environment. *Astrophys. J.*, 647:692–708, 2006. [Erratum: Astrophys.J. 662, 779 (2007)].

[143] S. R. Kelner, F. A. Aharonian, and V. V. Bugayov. Energy spectra of gamma-rays, electrons and neutrinos produced at proton-proton interactions in the very high energy regime. *Phys. Rev. D*, 74:034018, 2006. [Erratum: Phys.Rev.D 79, 039901 (2009)].

[144] T. M. Kneiske. Gamma-ray background: A review. *Chinese Journal of Astronomy and Astrophysics*, 8:219–225, 2008.

[145] K. Knie, G. Korschinek, T. Faestermann, C. Wallner, J. Scholten, et al. Indication for Supernova Produced Fe-60 Activity on Earth. *Phys.Rev.Lett.*, 83:18–21, 1999.

[146] S. Koldobskiy, M. Kachelrieß, A. Lskavyan, A. Neronov, S. Ostapchenko, and D. V. Semikoz. Energy spectra of secondaries in proton-proton interactions, 2021.

[147] S. Koldobskiy, A. Neronov, and D. Semikoz. Pion decay model of the tibet- asγ pev gamma-ray signal. *Physical Review D*, 104(4), Aug 2021.

[148] W. Kolhörster, I. Matthes, and E. Weber. Gekoppelte Höhenstrahlen. *Naturwissenschaften*, 26(35):576–576, Sept. 1938.

[149] A. Kolmogorov. The Local Structure of Turbulence in Incompressible Viscous Fluid for Very Large Reynolds' Numbers. *Akademiia Nauk SSSR Doklady*, 30:301–305, Jan. 1941.

[150] M. Krause. Magnetic fields and star formation in spiral galaxies. In *RevMexAA (Serie de Conferencias)*, volume 36, page 25–29, 2009.

[151] M. Krause, C. Charbonnel, T. Decressin, G. Meynet, and N. Prantzos. Superbubble dynamics in globular cluster infancy. *Astronomy & Astrophysics*, 552:A121, Apr 2013.

[152] G. V. Kulikov and G. B. Khristiansen. On the size distribution of extensive atmospheric showers. *J. Exp. Theor. Phys.*, 35:8, 1 1958.

[153] R. Lallement, C. Babusiaux, J. L. Vergely, D. Katz, F. Arenou, B. Valette, C. Hottier, and L. Capitanio. Gaia-2mass 3d maps of galactic interstellar dust within 3 kpc. *Astronomy & Astrophysics*, 625:A135, May 2019.

[154] R. Lallement, B. Y. Welsh, J. L. Vergely, F. Crifo, and D. Sfeir. 3D mapping of the dense interstellar gas around the Local Bubble. *Astron. Astrophys.* , 411:447–464, Dec. 2003.

[155] Lallement, R., Capitanio, L., Ruiz-Dern, L., Danielski, C., Babusiaux, C., Vergely, L., Elyajouri, M., Arenou, F., and Leclerc, N. Three-dimensional maps of interstellar dust in the local arm: using gaia, 2mass, and apogee-dr14. *A&A*, 616:A132, 2018.

[156] C. M. G. LATTES, G. P. S. OCCHIALINI, and C. POWELL. Observations on the tracks of slow mesons in photographic emulsions. *Nature*, 160(4066):453—456, October 1947.

[157] R. H. Leike, M. Glatzle, and T. A. Enßlin. Resolving nearby dust clouds. *Astronomy & Astrophysics*, 639:A138, Jul 2020.

[158] K. Lodders. Solar system abundances and condensation temperatures of the elements. *The Astrophysical Journal*, 591(2):1220–1247, jul 2003.

[159] M. Lombardi, C. J. Lada, and J. Alves. 2mass wide field extinction

maps ii. the ophiuchus and the lupus cloud complexes. *Astronomy & Astrophysics*, 489(1):143–156, Jul 2008.

[160] M. Lombardi, C. J. Lada, and J. Alves. 2MASS wide field extinction maps. III. The Taurus, Perseus, and California cloud complexes. *Astron. Astrophys.* , 512:A67, Mar. 2010.

[161] Lombardi, M. and Alves, J. Mapping the interstellar dust with near-infrared observations: An optimized multi-band technique. *A&A*, 377(3):1023–1034, 2001.

[162] Lombardi, Marco and Alves, Joao and Lada, Charles J. 2MASS wide field extinction maps. 1. The Pipe nebula. *Astron. Astrophys.*, 454:781, 2006.

[163] S. A. Mao, B. M. Gaensler, M. Haverkorn, E. G. Zweibel, G. J. Madsen, N. M. McClure-Griffiths, A. Shukurov, and P. P. Kronberg. A survey of extragalactic faraday rotation at high galactic latitude: The vertical magnetic field of the milky way toward the galactic poles. *The Astrophysical Journal*, 714(2):1170–1186, Apr 2010.

[164] M. A. Markov. On high energy neutrino physics. In *10th International Conference on High Energy Physics*, pages 578–581, 1960.

[165] D. Maurin, R. Taillet, and F. Donato. New results on source and diffusion spectral features of galactic cosmic rays: I $B\vec{/}C$ ratio. *Astronomy & Astrophysics*, 394(3):1039–1056, Oct 2002.

[166] I. V. Moskalenko, A. W. Strong, J. F. Ormes, and M. S. Potgieter. Secondary antiprotons and propagation of cosmic rays in the galaxy and heliosphere. *The Astrophysical Journal*, 565(1):280–296, Jan 2002.

[167] A. Neronov, M. Kachelrieß, and D. Semikoz. Multimessenger gamma-ray counterpart of the icecube neutrino signal. *Physical Review D*, 98(2), Jul 2018.

[168] A. Neronov and D. Semikoz. Lhaaso telescope sensitivity to diffuse gamma-ray signals from the galaxy. *Physical Review D*, 102(4), Aug 2020.

[169] A. Neronov, D. Semikoz, and I. Vovk. New limit on high galactic latitude pev gamma-ray flux from tibet asγ data. *Astronomy & Astrophysics*, 653:L4, Sep 2021.

[170] A. Neronov and D. V. Semikoz. Evidence the Galactic contribution to the IceCube astrophysical neutrino flux. *Astropart. Phys.*, 75:60–63, 2016.

[171] A. Neronov and D. V. Semikoz. Galactic and extragalactic contributions to the astrophysical muon neutrino signal. *Phys. Rev.*, D93(12):123002, 2016.

[172] Neronov, A. and Semikoz, D. Galactic diffuse gamma-ray emission at tev energy. *A&A*, 633:A94, 2020.

[173] L. O'C. Drury, E. van der Swaluw, and O. Carroll. Particle acceleration in supernova remnants, the Bell-Lucek hypothesis and the cosmic ray "knee". *arXiv e-prints*, pages astro–ph/0309820, Sept. 2003.

[174] S. Ostapchenko. Enhanced Pomeron diagrams: Re-summation of unitarity cuts. *Phys. Rev.*, D77:034009, 2008.

[175] S. Ostapchenko. Monte Carlo treatment of hadronic interactions in enhanced Pomeron scheme: I. QGSJET-II model. *Phys. Rev.*, D83:014018, 2011.

[176] D. Osterbrock. Ucsc course notes, January 1984.

[177] A. Palladino, C. Mascaretti, and F. Vissani. On the compatibility of the IceCube results with a universal neutrino spectrum. *Eur. Phys. J.*, C77(10):684, 2017.

[178] A. Palladino and W. Winter. A Multi-Component Model for the Observed Astrophysical Neutrinos. 2018.

[179] A. D. Panov, J. H. Adams, H. S. Ahn, G. L. Bashinzhagyan, J. W. Watts, J. P. Wefel, J. Wu, O. Ganel, T. G. Guzik, V. I. Zatsepin, and et al. Energy spectra of abundant nuclei of primary cosmic rays from the data of atic-2 experiment: Final results. *Bulletin of the Russian Academy of Sciences: Physics*, 73(5):564–567, May 2009.

[180] E. Parizot, A. Marcowith, E. van der Swaluw, A. M. Bykov, and V. Tatischeff. Superbubbles and energetic particles in the galaxy. *Astronomy & Astrophysics*, 424(3):747–760, Sep 2004.

[181] T. Pierog, I. Karpenko, J. M. Katzy, E. Yatsenko, and K. Werner. Epos lhc: Test of collective hadronization with data measured at the cern large hadron collider. *Physical Review C*, 92(3), Sep 2015.

[182] Prosin, V.V. et al. Primary cr energy spectrum and mass composition by the data of tunka-133 array. *EPJ Web of Conferences*, 99:04002, 2015.

[183] M. S. Pshirkov, P. G. Tinyakov, P. P. Kronberg, and K. J. Newton-McGee. Deriving the global structure of the galactic magnetic field from faraday rotation measures of extragalactic sources. *The Astrophysical Journal*, 738(2):192, Aug 2011.

[184] V. S. Ptuskin, S. I. Rogovaya, V. N. Zirakashvili, L. G. Chuvilgin, G. B. Khristiansen, E. G. Klepach, and G. V. Kulikov. Diffusion and drift of very high energy cosmic rays in galactic magnetic fields. *Astron. Astrophys.* , 268(2):726–735, Feb. 1993.

[185] K. Rawlins. Cosmic ray spectrum and composition from three years of IceTop and IceCube. *Journal of Physics: Conference Series*, 718:052033, may 2016.

[186] S. Recchia, P. Blasi, and G. Morlino. Cosmic ray-driven winds in the galactic environment and the cosmic ray spectrum. *Monthly Notices of the Royal Astronomical Society*, 470(1):865–881, May 2017.

[187] S. Recchia, S. Gabici, F. A. Aharonian, and V. Niro. Giant cosmic-ray halos around m31 and the milky way. *The Astrophysical Journal*, 914(2):135, Jun 2021.

[188] Reich, P., Testori, J. C., and Reich, W. A radio continuum survey of the southern sky at 1420 mhz* - the atlas of contour maps. *A&A*, 376(3):861–877, 2001.

[189] P. E. Reichley, G. S. Downs, and G. A. Morris. Time-of-Arrival Observations of Eleven Pulsars. *Astrophys. J. Lett.* , 159:L35–L40, Jan. 1970.

[190] G. D. Rochester and C. C. Butler. Evidence for the Existence of New Unstable Elementary Particles. *Nature*, 160:855–857, 1947.

[191] F. G. Schröder. Radio detection of cosmic-ray air showers and high-energy neutrinos. *Progress in Particle and Nuclear Physics*, 93:1–68, 2017.

[192] M. M. Schulreich, D. Breitschwerdt, J. Feige, and C. Dettbarn. Numerical studies on the link between radioisotopic signatures on Earth and the formation of the Local Bubble - I. 60Fe transport to the solar system by turbulent mixing of ejecta from nearby supernovae into a locally homogeneous interstellar medium. *Astron. Astrophys.*, 604:A81, 2017.

[193] G. D. Sciascio. The lhaaso experiment: from gamma-ray astronomy to cosmic rays, 2016.

[194] F. W. Stecker, M. A. Malkan, and S. T. Scully. Intergalactic photon spectra from the far-ir to the uv lyman limit for $0 < z < 6$ and the optical depth of the universe to high-energy gamma rays. *The Astrophysical Journal*, 648(2):774–783, Sep 2006.

[195] J. Stettner. Measurement of the diffuse astrophysical muon-neutrino spectrum with ten years of icecube data, 2019.

[196] R. Stothers. Age of the VELA pulsar PSR 0833-45. *Publications of the Astronomical Society of the Pacific* , 92:145–146, Apr. 1980.

[197] A. W. Strong, I. V. Moskalenko, T. A. Porter, G. Jóhannesson, E. Orlando, and S. W. Digel. The galprop cosmic-ray propagation code, 2009.

[198] A. W. Strong, I. V. Moskalenko, and V. S. Ptuskin. Cosmic-ray propagation and interactions in the galaxy. *Annual Review of Nuclear and Particle Science*, 57(1):285–327, Nov 2007.

[199] Sun, X. H., Reich, W., Waelkens, A., and Enßlin, T. A. Radio observational constraints on galactic 3d-emission models. *A&A*, 477(2):573–592, 2008.

[200] I. Sushch, B. Hnatyk, and A. Neronov. Modeling of the Vela complex including the Vela supernova remnant, the binary system γ^2 Velorum, and the Gum nebula. *Astron. Astrophys.*, 525:A154, 2011.

[201] S. I. Syrovatskii. Cosmic Rays of Ultra-High Energy. *Comments on Astrophysics and Space Physics*, 3:155, Sept. 1971.

[202] A. R. Taylor, J. M. Stil, and C. Sunstrum. A ROTATION MEASURE IMAGE OF THE SKY. *The Astrophysical Journal*, 702(2):1230–1236, aug 2009.

[203] Testori, J. C., Reich, P., and Reich, W. A fully sampled cm linear polarization survey of the southern sky. *A&A*, 484(3):733–742, 2008.

[204] G. Thomson. Physics of the tale experiment. 5:1593–1596, 01 2008.

[205] S. Thoudam, J. P. Rachen, A. van Vliet, A. Achterberg, S. Buitink, H. Falcke, and J. R. Hörandel. Cosmic-ray energy spectrum and composition up to the ankle: the case for a second galactic component. *Astronomy & Astrophysics*, 595:A33, Oct 2016.

[206] M. Tluczykont* and others on behalf of the TAIGA Collaboration. Taiga-hiscore: results from the first two operation seasons. *PoS ICRC2017*, 759, 2018.

[207] M. Unger. Highlights from the pierre auger observatory (icrc17), 2017.

[208] A. J. van Marle, Z. Meliani, and A. Marcowith. A hydrodynamical model of the circumstellar bubble created by two massive stars. *Astronomy & Astrophysics*, 541:L8, May 2012.

[209] A. J. van Marle, Z. Meliani, and A. Marcowith. Shape and evolution

of wind-blown bubbles of massive stars: on the effect of the interstellar magnetic field. *Astronomy & Astrophysics*, 584:A49, Nov 2015.

[210] T. M. Venters. Contribution to the extragalactic gamma-ray background from the cascades of very high energy gamma rays from blazars. *The Astrophysical Journal*, 710(2):1530–1540, Feb 2010.

[211] A. Wallner, J. Feige, N. Kinoshita, M. Paul, L. K. Fifield, R. Golser, M. Honda, U. Linnemann, H. Matsuzaki, S. Merchel, G. Rugel, S. G. Tims, P. Steier, T. Yamagata, and S. R. Winkler. Recent near-Earth supernovae probed by global deposition of interstellar radioactive ^{60}Fe. *Nature* , 532:69–72, Apr. 2016.

[212] J. Z. Wang et al. Measurement of cosmic-ray hydrogen and helium and their isotopic composition with the BESS experiment. *The Astrophysical Journal*, 564(1):244–259, jan 2002.

[213] S. Wang and X. Chen. The optical to mid-infrared extinction law based on the apogee, gaia dr2, pan-starrs1, sdss, apass, 2mass, and wise surveys. *The Astrophysical Journal*, 877(2):116, Jun 2019.

[214] M. Wolleben, A. Fletcher, T. L. Landecker, E. Carretti, J. M. Dickey, B. M. Gaensler, M. Haverkorn, N. McClure-Griffiths, W. Reich, and A. R. Taylor. Antisymmetry in the faraday rotation sky caused by a nearby magnetized bubble. *The Astrophysical Journal*, 724(1):L48–L52, Oct 2010.

[215] J. Xu and J.-L. Han. A compiled catalog of rotation measures of radio point sources. *Research in Astronomy and Astrophysics*, 14(8):942–958, jul 2014.

[216] Y. S. Yoon, T. Anderson, A. Barrau, N. B. Conklin, S. Coutu, L. Derome, J. H. Han, J. A. Jeon, K. C. Kim, M. H. Kim, and et al. Proton and helium spectra from the cream-iii flight. *The Astrophysical Journal*, 839(1):5, Apr 2017.

[217] Y. S. Yoon et al. Cosmic-ray Proton and Helium Spectra from the First CREAM Flight. *Astrophys. J.*, 728(122):8, 2011.

[218] H. YUKAWA. On the interaction of elementary particles. i. *Proceedings of the Physico-Mathematical Society of Japan. 3rd Series*, 17:48–57, 1935.

[219] V. I. Zatsepin and N. V. Sokolskaya. Three component model of cosmic ray spectra from 10 gev to 100 pev. *Astronomy & Astrophysics*, 458(1):1–5, Oct 2006.

[220] C. Zhen. Highlights of the ARGO-YBJ Experiment at 4,300 m a.s.l. *Braz. J. Phys.*, 44:494–503, 2014.

[221] E. J. Zirnstein, J. Heerikhuisen, H. O. Funsten, G. Livadiotis, D. J. McComas, and N. V. Pogorelov. LOCAL INTERSTELLAR MAGNETIC FIELD DETERMINED FROM THEINTERSTELLAR BOUNDARY EXPLORER RIBBON. *The Astrophysical Journal*, 818(1):L18, feb 2016.